Large-area and lumped element field-effect transistors for picosecond-scale detection in the Terahertz band and beyond

Vom Fachbereich Elektrotechnik und Informationstechnik
der Technischen Universität Darmstadt
zur Erlangung des akademischen Grades
eines Doktor-Ingenieurs (Dr.-Ing.)
genehmigte

Dissertation

von

M.Sc.
Stefan Regensburger
aus Neumarkt i.d.OPf.

Referent: Prof. Dr. Sascha Preu
Korreferent: Prof. Dr. Hartmut G. Roskos

D17
Darmstadt 2019

Regensburger, Stefan:
Large-area and lumped element field-effect transistors for
picosecond-scale detection in the Terahertz band and beyond

Darmstadt, Technische Universität Darmstadt,
Jahr der Veröffentlichung der Dissertation auf TUprints: 2019
URN: urn:nbn:de:tuda-tuprints-91893
URL: https://tuprints.ulb.tu-darmstadt.de/id/eprint/9189
Tag der Einreichung: 02.07.2019
Tag der mündlichen Prüfung: 14.10.2019

Contents

Abbreviations

2DEG 2 dimensional electron gas

AC Alternating current

A-FET Antenna-coupled field-effect transistor

AlGaAs Aluminium gallium arsenide

ARC Anti-reflective coating

BWO Backward-wave oscillator

CPW Coplanar waveguide

CW Continuous wave

D Drain

DC Direct current

ENBW Equivalent noise bandwidth

EOS Electro-optical sampling

FET Field-effect transistor

FEL Free electron laser

FELBE THz and MIR free electron laser at Helmholtz-Zentrum Dresden-Rossendorf

FIR Far-infrared

FWHM Full width at half maximum

G Gate

GaAs Gallium arsenide

GHz Gigahertz (10^9 Hz)

HEMT High-electron-mobility transistor

HFET Heterojunction field-effect transistor

IR Infrared radiation

IF Intermediate frequency

LA-FET Large-area field-effect transistor

LO Local oscillator

MCT Mercury cadmium telluride

MIR Mid-infrared

MODFET Modulation-doped field-effect transistor

MOSFET Metal–oxide–semiconductor field-effect transistor

NEP Noise equivalent power

NIR Near-infrared

QCL Quantum cascade laser

RC Resistor-capacitor

S Source

Si Silicon

SMA SubMiniature version A connector

SNR Signal-to-noise ratio

THz Terahertz (10^{12} Hz)

UV Ultraviolet

Abstract

Because of inefficient sources and detectors, the Terahertz band (0.1 - 10 THz) located in between electronics with tens of Gigahertz (GHz) and optics with tens of Terahertz (THz) remained hardly accessible for a long time. Rapid advances in research and development of technology for emission and detection in recent years finally enable the technical utilization of this frequency range and an increasing number of applications. This thesis focuses on the direct detection with field-effect transistors (FETs) to improve the access to the THz band with compact and fast room-temperature operating detectors. Meanwhile, there are various promising applications for real-time detection, such as communication, automotive distance radar, or spectroscopy. One main focus of this thesis is an application linked to high THz power facilities: The characterization of pulse shapes in accelerator-based experiments.

In a simple picture, a THz bias applied to a FET simultaneously modulates the charge carrier velocity as well as the charge carrier density underneath the gate electrode. As a result, a DC current is generated, that is proportional to the incident THz power. The state-of-the-art model from M. Dyakonov and M. Shur from the 1990's describes the 2 dimensional electron gas (2DEG) with hydrodynamic equations and predicts plasmonic rectification underneath the gate contact. This rectification mechanism is experimentally proven in the THz band well above the maximum frequency of oscillation f_{max} and cutoff frequency f_T of the FET.

This thesis experimentally studies the detection mechanism of field-effect transistor-based rectifiers in the THz band and beyond in the mid infrared (MIR) up to 30 THz on the ten-picosecond scale. To achieve this exceptional frequency coverage, an antenna-less concept, the large-area FET (LA-FET), is chosen. The fast, picosecond-scale response from the FETs supports the hypothesis of an underlying Dyakonov-Shur-like rectification mechanism up to and including 30 THz regarding the responsivity distribution of the detector area, and regarding the polarization dependence. Further, the comparison with gate-less reference samples shows a suppression of more than two orders of magnitude at 2.0 THz and one order of magnitude at 11.8 THz for additional mechanisms that do not require a gate electrode. However, the gate bias dependence reduces towards higher frequencies, pointing towards a contribution of a yet unknown detection process. The fabricated detectors prove ultra-fast detection in the entire THz band with the exception of the GaAs Reststrahlen band. The upper limit of the internal rectification process evaluates to a Gaussian time constant of 7.1 ps. The slow, millisecond-response of the FETs shows increasing contributions from non-Dyakonov-Shur-like rectification mechanisms with increasing frequency, such as bolometric detection. The observed $f^{-1.4}$ roll-off is less strong than a RC roll-off with fixed resistance. This suggests an increasing radiation resistance of the LA-FET design for increasing frequency, that improves the incoupling of THz power to the FET. The large area allows to achieve a linearity range of 69 dB/$\sqrt{\text{Hz}}$, by distributing the THz power over the square-millimeter-scale active area. As compared to detectors available at the beginning of this thesis the

responsivity is improved by two orders of magnitude, now allowing for the detection of picosecond-scale pulses at accelerator-based facilities without any pre-amplifier, and additionally the detection in most table-top systems.

Antenna-coupled FETs (A-FETs) are studied in a frequency range from 0.1 up to 11.8 THz. The measured responsivity agrees excellently with theoretical expectations derived from a simple equivalent circuit and the simulated radiation resistance. Devices processed with simple UV-contact lithography achieve a noise equivalent power (NEP) of 250 $\mathrm{pW}/\sqrt{\mathrm{Hz}}$ at 0.6 THz, only one order of magnitude above foundry-processed state-of-the-art FET detectors in 65 nm technology.

Finally, both LA-FET and A-FET detectors demonstrate pulse shape characterization of picosecond-scale THz pulses from a free electron laser (FEL). The characterization of asymmetric FEL pulses arising from cavity detuning with FETs and a grating spectrometer allows the verification of a novel convolution ansatz for the FEL pulse shape, developed within this thesis. This ansatz circumvents deficits in the state-of-the-art piecewise ansatz such as unsteady differentiability and includes the smooth transition to a symmetric, Gaussian pulse. The ansatz further allows to include the Gaussian intermediate frequency (IF) limitations of the A-FET and LA-FET detector. The convolution ansatz circumvents the Heisenberg-Gabor limit, as it allows to measure exponential rise times significantly below the Gaussian IF limitations.

Kurzfassung

Aufgrund eines Mangels an effizienten Quellen und Detektoren war das Terahertzband (0.1 - 10 THz) zwischen Hochfrequenzelektronik im Bereich von zehn Gigahertz (GHz) und Optik im Bereich von zehn Terahertz (THz) lange Zeit nur schwer zugänglich. In den letzten Jahren gab es rapide Fortschritte in der Technologie zur Erzeugung und Detektion von Terahertzwellen, wodurch die technische Nutzbarkeit dieses Frequenzbereichs verbessert wird und somit eine wachsende Zahl von Anwendungen ermöglicht wird. Dazu möchte auch diese Dissertation beitragen, deren Ziel es ist, durch Gleichrichtung mit kompakten Feldeffekttransistoren (FETs) die schnelle und direkte Detektion bei Raumtemperatur zu verbessern. Mittlerweile gibt es eine Vielzahl von erfolgversprechenden Anwendungen für Echtzeitdetektion, wie zum Beispiel die Kommunikation, das Abstandsradar im Automobilbereich und die Spektroskopie. In einem viel höheren Leistungsbereich bewegt sich die Anwendung, auf der in dieser Forschungsarbeit ein Hauptaugenmerk liegt: Die Charakterisierung von Pulsformen in Beschleunigerexperimenten.

In einem vereinfachten Bild funktioniert die Gleichrichtung im FET durch die simultane Modulation der Ladungsträgerdichte und Ladungsträgergeschwindigkeit unterhalb des Gatekontakts. Der resultierende Gleichstrom ist proportional zur einfallenden THz-Leistung. M. Dyakonov und M. Shur modellierten das zweidimensionale Elektronengas (2DEG) mit hydrodynamischen Bewegungsgleichungen in den 1990er-Jahren und beschrieben die plasmonische Gleichrichtung unterhalb der Gateelektrode. Dieser Gleichrichtungsmechanismus ist im Terahertzband experimentell bestätigt, und funktioniert deutlich über der maximalen Oszillationsfrequenz f_{max} und Grenzfrequenz f_T der verwendeten FETs.

Diese Dissertation befasst sich mit dem Detektionsmechanismus von Feldeffekttransistoren im Terahertzband und darüber hinaus im mittleren Infrarot (MIR) bis 30 THz auf der Zehn-Pikosekundenskala. Um diesen extremen Frequenzbereich zu adressieren, wurde das Konzept von antennenlosen FETs (LA-FETs) ausgewählt. Die schnelle Detektorantwort der FETs auf der Pikosekundenskala ist hinsichtlich der Verteilung der Responsivität auf der Detektorfläche und der Polarisationsabhängigkeit vereinbar mit einer Dyakonov-Shur-Gleichrichtung bis einschließlich 30 THz. Weiter zeigt der Vergleich mit Referenzbauteilen ohne Gateelektrode eine Unterdrückung von Signalen aus Gleichrichtungsprozessen, die keine Gateelektrode benötigen, von mehr als zwei Größenordnungen bei 2.0 THz und einer Größenordnung bei 11.8 THz. Die Abhängigkeit von der Gatespannung wird hingegen schwächer hin zu höheren Frequenzen und deutet auf einen Beitrag von einem bisher nicht identifizierten Detektionsprozess hin. Mit Ausnahme des GaAs-Reststrahlenbandes besitzen die Detektoren eine Frequenzabdeckung im gesamten Terahertzband. Die Obergrenze für die intrinsische Detektionsgeschwindigkeit kann mit einer Gauß-Zeitkonstante von 7.1 ps angegeben werden. Die langsame Detektorantwort auf einer Millisekundenskala zeigt einen steigenden Anteil von anderen Gleichrichtungsmechanismen hin zu höheren Frequenzen. Ein möglicher Mechanismus ist eine bolometrische Detektion. Das gemessene $f^{-1.4}$ Frequenzverhalten ist schwächer als ein RC Abklingverhalten mit

konstantem Widerstand und deutet daher auf einen steigenden Strahlungswiderstand des LA-FETs für höhere Frequenzen hin, der die Einkopplung von THz-Leistung zu dem FET verbessert. Die großflächigen Detektoren zeigen einen Linearitätsbereich von $69\,\mathrm{dB}/\sqrt{\mathrm{Hz}}$. Im Vergleich zu Detektoren, welche zu Anfang dieser Forschungsarbeit zur Verfügung standen, konnte die Responsivität um zwei Größenordnungen verbessert werden und ermöglicht jetzt eine Detektion von Pulsen im Pikosekundenbereich an Beschleunigereinrichtungen ohne Vorverstärker, und zusätzlich auch eine Detektion in den meisten kompakteren Aufbauten im Labormaßstab.

Antennengekoppelte FETs (A-FETs) werden in einem Frequenzbereich von 0.1 bis 11.8 THz untersucht. Die gemessene Responsivität zeigt eine exzellente Übereinstimmung mit theoretischen Erwartungen aus einem einfachem Ersatzschaltbild und dem simulierten Strahlungswiderstand. Mit einfacher UV-Kontaktlithographie wird zudem eine äquivalente Rauschleistung (engl. Abk. NEP) von $250\,\mathrm{pW}/\sqrt{\mathrm{Hz}}$ bei 0.6 THz erreicht, die nur eine Größenordnung über der NEP von FETs liegt, welche mit 65 nm Technologie in Halbleiterwerken gefertigt wurden.

Sowohl mit einem LA-FET, als auch mit einem A-FET Detektor wird die Charakterisierung der Pulsform von Terahertzpulsen eines freien Elektronenlasers (FEL) im Pikosekundenbereich demonstriert. Im Rahmen dieser Dissertation wird ein neuer Faltungsansatz für die Beschreibung von asymmetrischen Pulsen in Abhängigkeit der FEL-Kavitätsverstimmung präsentiert und experimentell mit Zeitbereichsmessungen der FETs und Frequenzbereichsmessungen mit einem Gitterspektrometer verifiziert. Dieser Ansatz umgeht die Schwachpunkte der unstetigen Differenzierbarkeit der bisher in der Literatur vorherrschenden abschnittsweisen Modellierung und erlaubt einen kontinuierlichen Übergang zu einem symmetrischen Gaußpuls. Weiter erlaubt das neue Modell, die gaußförmige Limitierung in der Zwischenfrequenz (engl. Abk. IF) mit einzubeziehen. Mit dem Faltungsansatz kann die Heisenberg-Gabor-Beschränkung umgangen werden, da exponentielle Anstiegszeiten deutlich unterhalb der gaußförmigen IF-Limitierung gemessen werden können.

1. Introduction

1.1. Terahertz band – access and utilization

For many years, there has been a technological gap in the frequency spectrum of electromagnetic waves. While high speed electronics in the tens of Gigahertz (GHz) range as well as infrared optics in the tens of Terahertz (THz) range have been widely utilized, the frequency range in between remained virtually inaccessible for many applications that were possible in electronics and infrared optics. Since about two decades, this part of the spectrum is now receiving steadily growing attention from researchers and industry, working in the Terahertz field. There is no fixed definition for the Terahertz band, but it is mostly referred to as the frequency range from 100 GHz to 10 THz, as shown in Fig. 1.1. The access to the Terahertz band is impeded by the availability of compact and efficient sources and detectors. Because of technical challenges in generation and detection, the Terahertz band was long time referred to as the "Terahertz gap" between electronics and optics.

Nowadays, a strong development in the output power of sources and the sensitivity of detectors is ongoing, enabling more applications in the Terahertz band, but still not reaching a performance similar to electronics or infrared optics. The available powers are still low. For example, photomixer sources, that are in widespread use in table-top systems for continous-wave (CW) THz spectroscopy, can generate output powers in the few μW range at 1 THz [1]. Quantum cascade lasers (QCLs) produce mW power levels at cryogenic temperatures, however they feature a limited tunability and can hardly be operated at frequencies below 1 THz [2, p.128ff.]. Promising THz applications are *communication*, because this part of the electromagnetic spectrum is almost unused so far, *automotive distance control by radar* with improved resolution as compared to microwave solutions, *spectroscopy and molecular fingerprinting* [3–6]. While all scientific advancements in the design, characterization and physical understanding of Terahertz detectors will be potentially beneficial for the aforementioned applications, the current thesis has a special focus on a detection concept which is ideally suitable for the following application: Providing *advanced beam diagnostics* for accelerator based research [7].

1.2. Motivation

Accelerator-based generation of highly intense electromagnetic radiation can be achieved with relativistic electron beams, such as synchrotrons, linear accelerators, and free electron lasers (FELs). They are able to generate ultra-short pulses with a very high peak power and a wide tunability of the spectral characteristics. These systems allow for probing physics at extreme conditions and experiments not possible with table-top systems. They enable a new class of experiments to access non-linearities with their ultra-short and high power pulses [10–12]. For stable operation, the electron beam must be monitored on a sub-picosecond or even femtosecond timescale. Such arrival time monitors are often high speed detectors that resolve

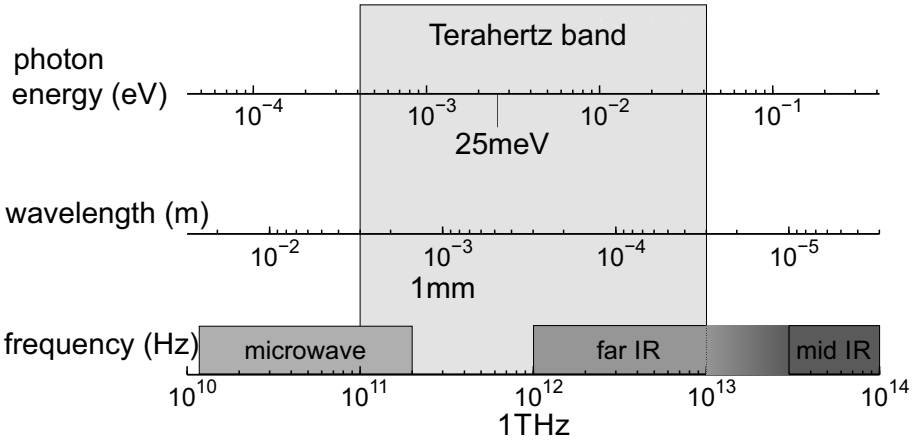

Fig. 1.1: *Terahertz band between optics and electronics. Adapted from [8; 9]*

the electromagnetic field generated by the passing electron. Further, FELs can be designed for operation at THz frequencies. In an FEL, relativistic electrons provide gain to the electromagnetic radiation in an undulator. FELs feature an extreme frequency tunability, not possible with table-top sources. Pump-probe experiments including an FEL allow to probe non-linearities under extreme conditions with picosecond pulses at THz frequencies. FELs can be synchronized with near-infrared (NIR) lasers such as a titanium-sapphire (Ti:Sa) laser, allowing intense THz excitation and probing a temporal delay at 800 nm. However, the THz pulse from the FEL and the NIR laser are separate entities and do not have natural locking. Therefore jitter and drift on the picosecond-scale impede experiments that require averaging or scanning-type measurements. Usually, for low power experiments the main requirement for detectors is a high sensitivity or low noise equivalent power (NEP). This class of experiments with ultra-short high power pulses and extreme frequency tunability requires detectors that can *withstand the extreme power levels*, and *resolve picosecond-scale pulses*. The detector should further feature a large *linearity range* and an *extreme frequency coverage*. Absorption lines of water vapor in ambient air temporally broaden pulses at selective frequencies, therefore ultra-short THz pulses need to be monitored as close as possible to the actual experiment, or in an N_2 enclosure. The detector should therefore be *compact*, *easy to handle*, work at *room temperature* and *not require a complex setup*. One **main objective** of this thesis is to develop a detector which provides **a good coverage of these requirements** and to **characterize FEL pulse shapes** with this detector.

The temporal width and temporal shape of THz pulses can be measured with different detection techniques:

- *Direct detection* allows to measure the intensity of the THz pulse. Thermal, electrical and certain optical detectors allow direct detection. Real-time detection of THz pulses in single shot mode is possible. The intermediate frequency (IF) bandwidth of the post detection system broadens the measured pulse width. The minimum detectable pulse width is limited by the bandwidth of the

whole IF path and the time constant of the detector. For the case of envelope detection, the IF bandwidth is also referred to as video bandwidth.

There are different realizations of direct detectors with large IF bandwidths, also used for communication in a narrowband configuration [3; 13]. YBCO detectors at cryogenic temperatures reach a minimum detected full width at half maximum (FWHM) pulse width of 16 ps and 30 ps with a 63 GHz and 30 GHz oscilloscope, respectively [14; 15]. Quasi optical Schottky diodes feature an IF bandwidth of 10 GHz at 75 GHz carrier frequency [16]. Waveguide coupled Schottky diodes reach up to 40 GHz IF bandwidth at 300 GHz carrier frequency [17]. Coherent synchrotron radiation has been detected by Schottky diodes with response times of ≤ 20 ps [18]. Waveguide coupled field-effect transistor (FET) rectifiers in ref. [19] feature an 18 GHz IF bandwidth.

- *Electro-optical sampling (EOS)* measures a THz signal in the time domain. The THz pulse is sampled with an optical laser with tens of femtoseconds pulse width using optical $\chi^{(2)}$ rectification in a crystal. This technique allows to measure pulse widths below the picosecond-scale [20–22].

  Jitter and drift of FELs on the picosecond-scale impede typical scanning-type measurements of the electrical field with EOS. The temporal delay can only be reconstructed in data analysis after the measurement with a complex single pulse arrival time monitoring [23]. More complex setups may allow single shot measurement, however typically with a very limited time range [24].

- A more complex balanced *cross-correlation* setup with a low-jitter synchronized laser measures the THz pulse shape as well as the absolute timing to the laser through sum frequency generation [25].

- In an *auto-correlation* setup, the THz signal is split, one part is delayed and then both parts are overlapped again in a Mach-Zender interferometer geometry. The auto-correlated signal is measured subsequently against the time delay. The original signal in time domain can be reconstructed by deconvolution. However, noise and asymmetrical pulse shapes impede the reconstruction. Direct detectors such as field-effect transistors can be used in auto-correlation setups [26; 27]. The resolution limit is given by the resolution of the scanning delay and is therefore below the picosecond-scale. Therefore this technique is also used for femtosecond pulses in the optical domain. Scanning-type auto-correlation measurements are not suited for real-time pulse width acquisition.

- The *intensity spectrum* can be measured with a grating spectrometer and a direct detector. However, the intensity spectrum does not contain the spectral phase, such that information on a chirp in time domain is lost. The Fourier transformation of the spectrum yields the shortest possible pulse in time domain. This Heisenberg-Gabor limited pulse in time domain can be reconstructed by a deconvolution. However this reconstructed pulse does not need to be identical

to the pulse in time domain. Pulse widths below the picosecond-scale can be measured.

In this thesis, **FET-based rectifiers** are chosen as fast direct detectors for the broadband detection of THz pulses for the following reasons: FET detectors allow for real-time detection of amplitude and temporal distance of both THz pulses, and for 800 nm NIR pulses. FET detectors allow for operation at room temperature, offer a compact design, and are easy to handle. They do not require low-jitter synchronized lasers or cryogenic cooling.

The other **main objective** of this thesis is to study the **detection mechanism of FETs in the THz band and beyond in the mid infrared (MIR)**. By measuring the THz induced response on different time scales, the underlying detection mechanisms are compared. Finally, two different concepts of FET based detectors are evaluated against each other and applied for the study of picosecond-scale pulse shapes:

The concept of **large-area FETs** (LA-FETs) allows to distribute the THz power over a large active area to achieve a high destruction threshold and large linearity range. The antenna-less design avoids antenna resonances for a very large frequency coverage. Fig. 1.2a) shows a schematic of a LA-FET mounted on a silicon lens. The lens can be omitted for THz incoupling from the air-side.

Antenna-coupled FETs (A-FETs) concentrate the THz power in a lumped element FET with an antenna and are therefore more sensitive. With certain antennas, broadband operation is possible, however not obtaining the same frequency coverage as with antenna-less designs. Fig. 1.2b) shows a schematic of an A-FET mounted on a silicon lens.

Besides a focus on beam diagnostics in this thesis, A-FET detectors fabricated within this thesis can also be used in *table-top experiments* with the sensitivity achieved in this thesis. This allows for a wide range of applications e.g. in *spectroscopy* setups and *communication* with low available THz power. Other groups have also demonstrated FET-based cameras as detailed in the following chapter. In contrast, LA-FETs are ideally suited for applications where a large linearity range and extreme frequency coverage are required at a higher available THz power, such as pulse shape monitoring and pump-probe experiments. FET-based rectifiers have therefore a *large applicability* for detection of THz radiation, as demonstrated by the detection of CW THz radiation generated by photomixers, backward-wave oscillators (BWOs), QCLs, as well as picosecond THz pulses from an FEL and pulses from a CO_2 laser within this thesis.

1.3. Thesis outline

This thesis reviews the design, modeling, fabrication, and responsivity of field-effect transistors for the detection in the Terahertz band and beyond in the MIR. Major results of this thesis are the ultra-broadband characterization of LA-FETs from 0.1 THz up to 30 THz, and of antenna-coupled FETs from 0.1 up to 12 THz,

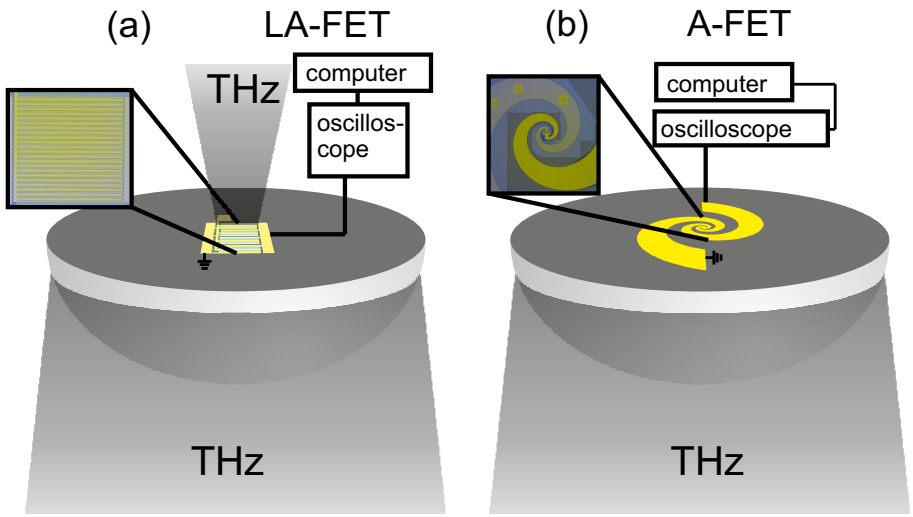

Fig. 1.2: *Schematic of FETs for rectification of THz radiation. The FET devices are mounted on hyper-hemispherical silicon lenses for improved incoupling. The zoom-ins show microscope images of FETs fabricated within this thesis. a) LA-FET for incoupling from the substrate side or from air side. The silicon lens can be omitted for incoupling from air side.* 800 *nm NIR pulses can optionally be detected for illumination from the air side. b) A-FET with spiral antenna for enhanced incoupling and responsivity.*

including a comparison with a transmission line model, published in ref. [28] and ref. [29], respectively. The fast response and the averaged, integrated fast and slow response of LA-FETs to THz and MIR is measured with a 2D scan of the detector area. The comparison with reference samples without gate allows to quantify competing detection mechanisms, that originate from imperfection of ohmic contacts. Additionally the measurement of pulses with temporal shape and width on the picosecond-scale is demonstrated with large-area as well as antenna-coupled lumped element FETs, published in ref. [30]. A novel, refined convolution ansatz for the description of FEL pulses from a detuned cavity allows a more accurate pulse description. Additionally the refined ansatz allows the extraction of exponential broadening below the Gaussian IF limitation of the measurement.

Chapter 2 introduces the state of the art of selected sources and detectors in the Terahertz band used within this thesis.

Chapter 3 describes the theory of THz detection in FETs. The ideal responsivity of a FET is derived based on the Dyakonov-Shur rectification mechanism. The transmission line model is used to calculate the electrical coupling efficiency for incoupling from the antenna to the active element. The concept of antenna-coupled and antenna-less large-area detectors is introduced along with the radiation resistance. Finally, the semiconductor structure of the AlGaAs-based FETs is introduced.

Further a novel convolution ansatz for the temporal pulse shape of free electron lasers is presented in **chapter 4**. The novel ansatz allows to model the dependence on

cavity detuning, giving the expected intensity pulses in time and frequency domain. Finally, the limitations from the IF bandwidth for the detection of such pulses are discussed.

Chapter 5 presents the design of the different detector concepts. Additionally the fabrication and DC characterization of the samples is discussed.

The experimental results of LA-FETs and A-FETs in the Terahertz band and beyond for frequency dependent responsivity, saturation, and gate bias dependence are presented and discussed in **chapter 6**. The results of the A-FETs are compared with the theoretical prediction from the transmission line model using simulated and measured device impedances.

Chapter 7 discusses the discrimination of non-Dyakonov-Shur-like rectification mechanisms. The picosecond-scale response of reference samples without gate contact is presented and compared with the picosecond-scale response of FETs. Additionally, the 2 dimensional picosecond-scale and millisecond-scale response scanned over the area of the LA-FET is compared with the reference samples. The response is measured for a polarization along and perpendicular to the channel of the FET for THz and MIR frequencies.

In **chapter 8**, the results from pulse-length dependent experiments are used for characterization of the pulse shape from an FEL as well as the temporal resolution of the A-FET and LA-FET device. The time domain traces recorded with the FETs are compared with the intensity spectra for different pulses.

Chapter 9 summarizes the findings and presents an outlook for future research on THz detection with FETs. A FET based concept for accelerator beam diagnostics is proposed.

2. State-of-the-art Terahertz sources and detectors

In this chapter the FEL as a THz source is presented in more detail and additionally a brief overview of table-top sources for Terahertz radiation is given. The overview is not exhaustive, but includes the devices used for experiments in the course of this thesis. After the overview of different THz sources, a brief overview of different THz detectors is given.

2.1. Terahertz sources

Many sources still generate THz indirectly either through frequency up- or down conversion. Important performance indicators for sources are the output power, P_{THz}, frequency tunability, frequency dependence of the output power $P_{\mathrm{THz}}(f)$, compactness for application in table-top systems, and pulsed or continuous wave operation mode.

2.1.1. Free electron laser

Free electron lasers (FELs) use a relativistic electron beam to emit electromagnetic radiation upon acceleration in an undulator. FELs are not realized as table-top sources, but as large scale facilities, due to the dimensions of the required electron accelerator and undulator. Fig. 2.1 shows a schematic drawing of a free electron laser. The undulator is placed in a cavity for the electromagnetic radiation. FELs are sources with a very high peak output power and an extreme frequency tunability. Depending on the components, different FELs can be built to cover frequencies from microwave up to the X-ray spectrum.

The wavelength λ_0 of the emitted radiation is given by

$$\lambda_0 = \frac{\lambda_u}{2\gamma^2}\left(1 + \frac{K^2}{2}\right), \tag{2.1}$$

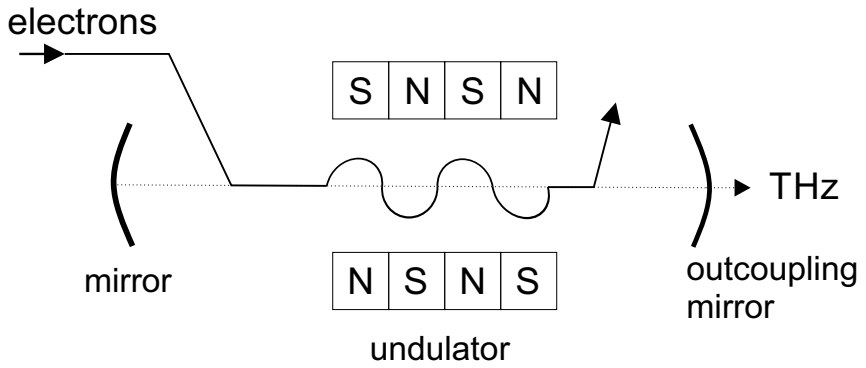

Fig. 2.1: *Working principle of a FEL. Electromagnetic radiation is emitted from relativistic electrons being diverted in the undulator. The undulator is placed in a cavity for the THz radiation.*

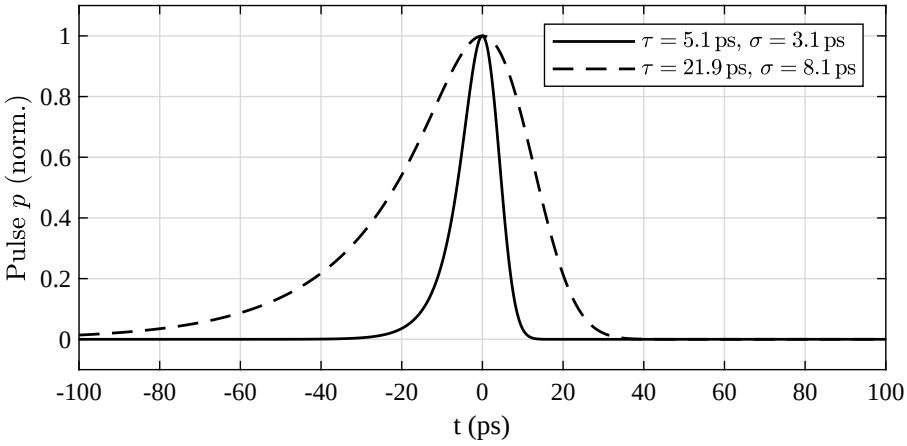

Fig. 2.2: *FEL pulse shapes for different cavity detunings, i.e. temporal delay between the electron bunch and the THz pulse in the undulator. The pulse is dominated by a Gaussian shape for a close to zero cavity detuning* $\Delta L \approx 0$ *(solid line), the rise is dominated by an exponential shape for a strong negative cavity detuning* $\Delta L \ll 0$ *(dashed line).*

with the dimensionless parameter $K = \frac{eB\lambda_u}{2\pi m_e c}$, the undulator period λ_u, the Lorentz factor $\gamma = 1/\sqrt{1-(v/c)^2}$, the magnetic field strength B, and the electron rest mass m_e. Electron bunches are accelerated to relativistic energies and guided into the undulator. The electromagnetic field in the undulator exerts a force back onto the electron bunch. Depending on the local electrical field, electrons are accelerated or decelerated in the electron bunch. As a result, micro bunches are formed in the order of the wavelength of the electromagnetic radiation in the undulator. The temporal delay Δt between the electron bunch (providing the gain) and the THz pulse can be tuned by the cavity length L. A zero cavity detuning $\Delta L = 0$ corresponds to perfect synchronization of the THz pulse and electron bunch. Due to the dynamics of the lasing process, the THz pulse needs to arrive earlier than the electron bunch to achieve stable lasing, such that the cavity needs to be shortened with $\Delta L < 0$ [31]. For very strong negative cavity detuning ($\Delta L \ll 0$), the output electromagnetic radiation is dominated by an exponentially rising edge [25; 30; 31]. In many cases only the relative change of the cavity length $\Delta L'$ is measured. It can be gauged in order to obtain the absolute cavity detuning.

Fig. 2.2 shows idealized FEL pulses from FELBE at 2.0 THz for different cavity detunings. The pulse with close to zero cavity detuning $\Delta L \approx 0$ is dominated by a Gaussian pulse shape with a slight asymmetry introduced by a Gaussian part. The pulse with strong negative cavity detuning $\Delta L \ll 0$ is dominated by an exponential behavior for the rising edge and a Gaussian falling edge.

2.1.2. Photomixer sources

Photomixer sources generate THz through frequency down conversion of NIR laser beams by absorption. For CW generation of Terahertz two optical laser beams with the respective frequencies f_1 and f_2 are overlapped. The resulting laser beam features a beat with the frequency difference $f_{THz} = |f_1 - f_2|$ of the two laser beams. This frequency difference can easily be tuned to a frequency within the THz range. Fig. 2.3 shows a schematic of the process and a realization with a pin-diode. The photomixer device converts the intensity oscillation with frequency f_{THz} of the heterodyned NIR lasers to an oscillating current with the frequency f_{THz}. This current is fed into an antenna that subsequently emits THz radiation. Fig. 2.4 shows the radiated power of a commercial HHI/Toptica 1550 nm pin-diode vs frequency. The power is measured with a calibrated Golay cell. The power shows a f^{-2} RC roll-off and a f^{-2} transit

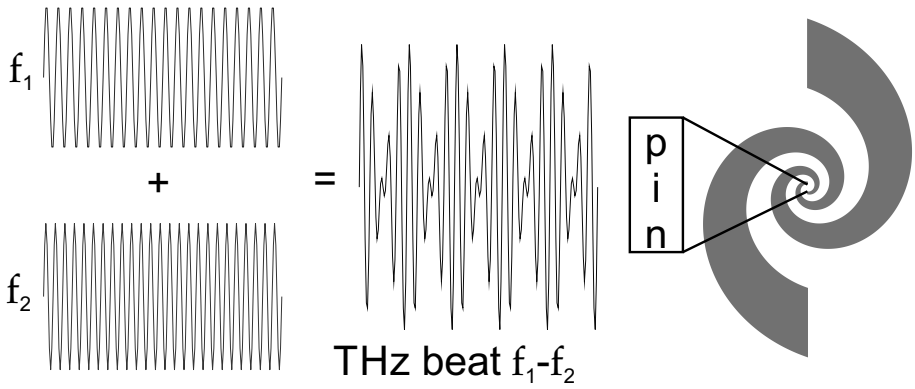

Fig. 2.3: *For CW generation two NIR lasers with frequency f_1 and f_2 are overlapped and fed onto the pin-diode. The pin-diode generates a current proportional to the beating $|f_1 - f_2| = f_{THz}$ of the NIR lasers. Adapted from [9].*

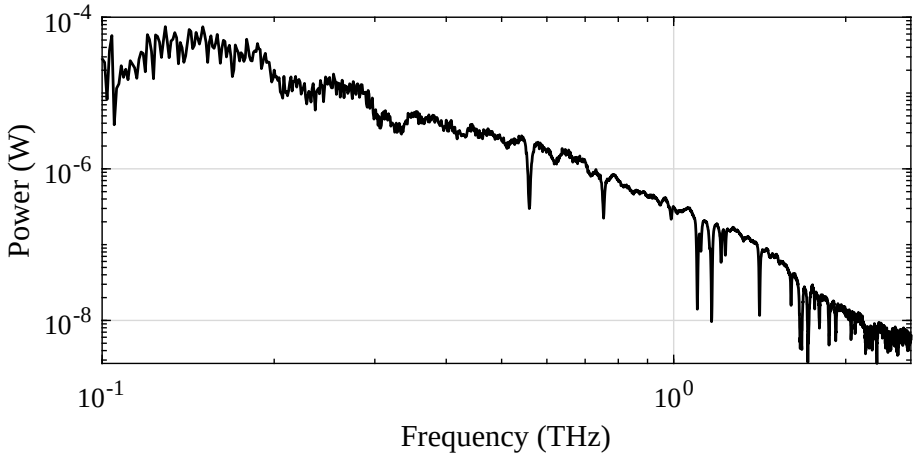

Fig. 2.4: *Power vs frequency of a commercial pin-diode from HHI/Toptica. The dips in the spectrum are due to the absorption of water vapor.*

time roll-off, above (typical) 3 dB frequencies of 0.2 and 0.9 THz, respectively. A more detailed study of the different roll-off mechanisms is presented in literature [1]. The benefit of this class of sources is the wide tunability and compactness of the devices suitable for table-top setups. Photomixer sources can reach power levels in the range of a few μW at 1 THz.

Photomixer sources (i.e. photoconductors) are also able to operate in a pulsed mode using a pulsed laser source. The output spectrum in pulsed operation is broadband with a bandwidth of several THz in contrast to a narrow line in CW operation.

2.1.3. Electronic sources

Electronic frequency multiplier source

Frequency multipliers allow to extend microwave technology to the THz band. Harmonic multiplier chains are compact, CW room-temperature THz sources, with a limited frequency tunability. Those sources rely on a cascaded multiplier chain, with an initial generator operating often with tens of GHz. The initial linewidth of those oscillators is typically narrow with $\Delta\lambda/\lambda \approx 10^{-6}$ [2, p.137]. Schottky diode based frequency multipliers are frequently used as frequency doublers as well as frequency triplers. Towards higher frequencies, the output power decreases, as power is lost in each frequency multiplication step and the efficiency of the multipliers also decreases for higher frequencies, while the linewidth increases. Output powers of 0.01 to 0.1 mW can be reached at 1 THz and a few μW at 1.9 THz [8, p.143]. The frequency tunability is limited by the respective waveguide band, such that for a wider tuning range additional multiplier chains need to be used. The limitation in frequency tunability in the respective waveguides allows to optimize the multipliers for a narrow frequency band and increase the efficiency of the individual multiplier stages. Typical tuning ranges are in the range of 50% of the center frequency.

Backward-wave oscillator

Backward-wave oscillators (BWO) are tunable room-temperature sources using the energy of an electron beam for the output radiation. BWOs are still compact enough to be used as table-top sources with dimensions in the order of a 19" rack. The source is named after the opposite direction between the electron beam and the amplification of the THz beam. The THz beam is outcoupled using a waveguide. Fig. 2.5 shows a schematic drawing of a BWO. Electrons are emitted from a thermionic cathode and accelerated by a DC bias voltage. They interact with the electromagnetic field in a periodic structure forming electron bunches and amplifying the THz beam. The key element of the BWO is a slow-wave structure enabling a phase match between the slower electrons with $v < c$ and the THz radiation at the speed of light c. The BWO is a fundamental oscillator with frequencies up to 1.4 THz, with multiplier chains the frequency range can be extended further. At around 100 GHz BWOs can reach output powers between 10 and 100 mW, at 1 THz the maximum power is between 0.1

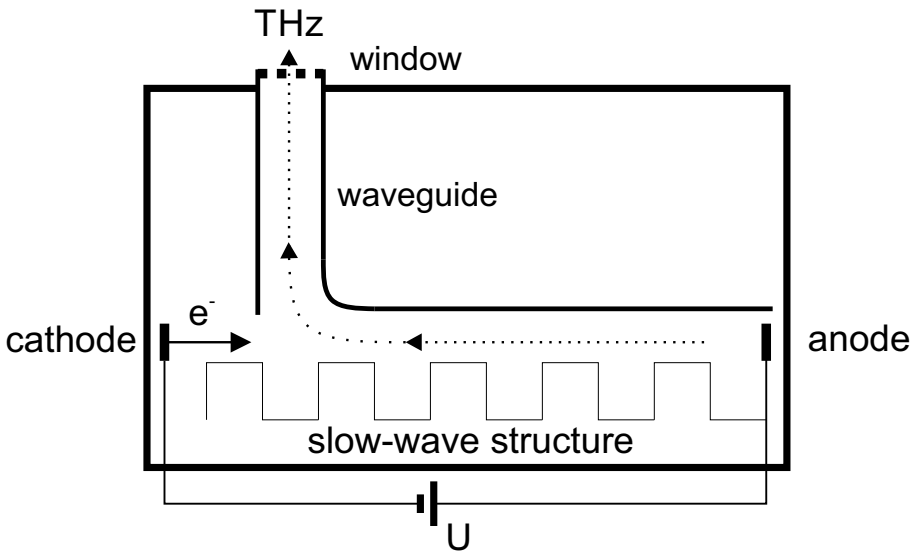

Fig. 2.5: *The electrons are emitted from a cathode and accelerated with a voltage U towards the anode along a slow-wave structure. The THz radiation is generated in backward direction of the electron beam and coupled out with a waveguide. Adapted from [2, p.145f.]*

and 1 mW [2, p. 144f]. For different waveguide bands, different BWOs are necessary. BWOs show a reproducible fluctuation of the output power within the individual waveguide band, and offer a limited tunability of the output frequency through the electron bias.

2.1.4. Optical sources

Optical sources include Quantum cascade lasers (QCLs), gas lasers and non-linear frequency conversion in a $\chi^{(2)}$ or $\chi^{(3)}$-active crystal. Within this thesis, a QCL and a CO_2 laser are used for the characterization of FET detectors. The basic principles and relevant properties of these laser types will be described in the following paragraphs.

Quantum cascade laser

In a quantum cascade laser, electrons within the conduction band emit photons in intersubband transitions within the conduction band [2, p.128ff.]. An electron injected into the conduction band cascades down a potential staircase. In a QCL that features m stages, a single electron emits m photons. In a single stage there are multiple energy levels, such that an population inversion is achieved to enable lasing. Lasing from 1.2 to 4.9 THz has been demonstrated with a from sub-mW up to a 100 mW power level [2, p.132]. The frequency tunability of single QCLs in the range of 0.01 $\Delta\lambda/\lambda_0$ is rather low, compared to other THz sources. Due to the small energy transitions in the Terahertz band on the order of thermal energy at room temperature, QCL are operated at cryogenic temperatures. Within this thesis, a

QCL operating at 3.8 THz is used [32].

CO_2 laser

CO_2 lasers operate in the MIR spectrum around 30 THz and are a powerful source located above the THz spectrum [33, p.11ff.]. Transitions between vibrational-rotational levels feature lines centered around 9.4 μm and 10.4 μm. The upper lasing level features a long μs lifetime and is mostly pumped by energy transfer from excited N_2 molecules. An electric discharge in a gas mixture including CO_2, He and N_2 excites N_2 molecules to a vibrational state. The excited N_2 molecules then excite the CO_2 molecule to the excited state. The efficient excitation of CO_2 molecules with N_2 molecules creates a population inversion in the CO_2 molecules. The lower levels after the stimulated emission in the CO_2 molecules are short-lived, due to collisions with He atoms.

CO_2 lasers are widely employed to pump molecular gas lasers with discrete lines in the THz band, with different gases [33, p.11]. For example, a CO_2-pumped NH_3 laser can emit at 8.6, 4.0, 3.3, 2.0, or 0.1 THz, depending on the exact pump frequency and other parameters.

2.2. Terahertz detectors

While generating THz in an efficient manner certainly remains an important subject for fundamental research and technology development, the focus of the current thesis was on the other end of the THz chain - the detection.

To provide a standardized measure of detector characteristics, the following quantities for comparison of detector performance are commonly used:

- *Responsivity*: The (voltage) responsivity is defined as $\mathcal{R} = \frac{U_{det}}{P_{\mathrm{THz}}}$, where U_{det} is the detected voltage and P_{THz} the incident THz power. The (external) responsivity $\mathcal{R}$ is referenced to the external THz power in contrast to the de-embedded, internal responsivity $\mathcal{R}^{id,0}$ considering coupling efficiencies η_i as $\mathcal{R} = \mathcal{R}^{id,0} \cdot \prod_i \eta_i$. For current detectors the respective current responsivity is defined as $\mathcal{R}_I = I_{det}/P_{\mathrm{THz}}$, where I_{det} is the detected current. With a transimpedance amplifier in the post-detection path, a current detector can also be used with the same post-detection electronics as a voltage detector.

- *SNR*: The signal to noise ratio (SNR) is a property of a concrete measurement and is defined as $\mathrm{SNR} = U_{det}/U_N$, with the noise voltage U_N.

- *Detection type*: THz radiation can be detected either in a direct or a mixer detection mode. In direct detection the intensity of the THz signal is measured such that the detector response is proportional to the THz power $U_{det} \propto P_{\mathrm{THz}}$. Mixer detectors are able to measure the field amplitude as well as the phase between a reference signal, i.e. from a local oscillator with P_{LO}, the response is proportional to the THz field $U_{det} \propto \sqrt{P_{LO} \cdot P_{\mathrm{THz}}} \propto E_{\mathrm{THz}}$.

- *NEP*: The performance indicator for the sensitivity of detectors is the noise equivalent power (NEP) defined for direct detection as

$$\mathrm{NEP} = \frac{U_N}{\mathcal{R} \cdot \sqrt{\Delta f}},$$

  with the measurement bandwidth Δf, that is also referred to as equivalent noise bandwidth (ENBW). The NEP is a measure for the minimum detectable power normalized to the measurement bandwidth Δf, respectively integration time of the post-detection electronics. For mixing detection, the NEP is defined as $\frac{U_N}{\mathcal{R} \cdot \Delta f}$. A lower NEP indicates a higher sensitivity of the detector.

- *Frequency coverage*: The frequency dependence of the responsivity $\mathcal{R}(f)$ determines the frequency coverage.

- *Detector response time*: For the detection of THz pulses and high modulation frequencies the response time and intermediate frequency bandwidth f_{IF} are crucial for determining the measured pulse shape and pulse width. For noise suppression, the THz signal is often modulated and detected with lock-in amplifiers. Further, communication requires modulation of data onto the THz carrier frequency. A slow detector response time ultimately limits the modulation frequency.

- *Linearity range and destruction threshold*: The direct detector output should be linear with the input. Within the desired range of power levels a large linearity range with a high 1 dB saturation point and large destruction threshold is desirable.

- *Operation conditions and prerequisites*: A compact detector working at room temperature is generally preferred over a bulky complex detection system requiring expensive equipment such as synchronized lasers and cryogenic cooling. The aperture of the detector for THz radiation is especially important for longer wavelengths with a larger diffraction-limited beam waist.

Besides field-effect transistor-based detectors a range of other detection concepts have been used in this thesis, that are detailed in the following sections. Some of them are used for benchmarking the developed FET detectors, others are used for calibration purposes.

2.2.1. Thermal detectors

Thomas Keating power meter

The Thomas Keating power meter is a broadband detector with a large entrance window. This power meter is composed of a closed gas chamber: between two windows, a thin metal foil absorbs ≈50% of the THz power. The modulated THz power heats the metal foil, such that a pressure wave at the modulation frequency is

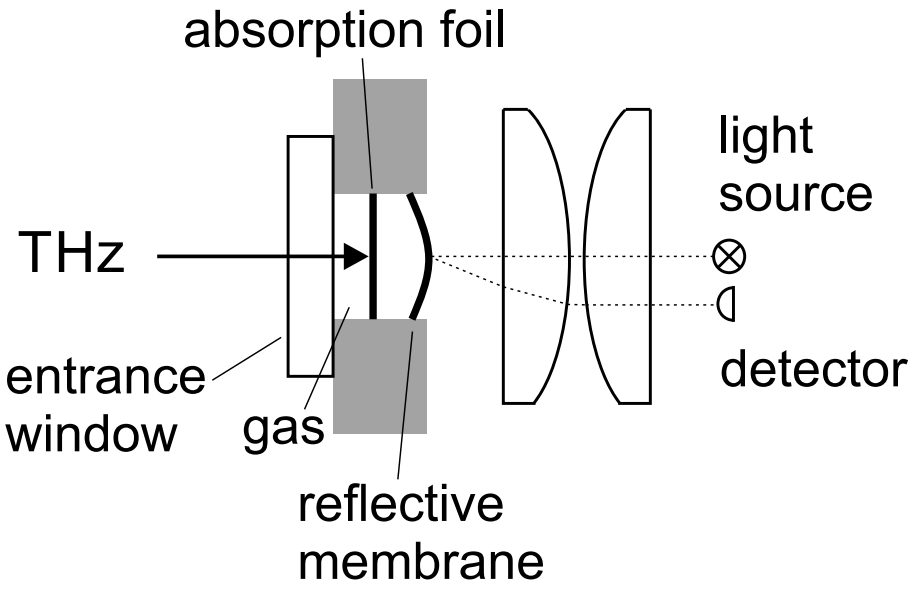

Fig. 2.6: *Schematic drawing of the Golay cell. THz radiation enters the gas cell through the entrance window and is absorbed by a foil. The heating of the gas expands the membrane, the deflection of the membrane is detected with an optical system.*

created in the gas chamber. The pressure wave is detected by a microphone. For a precise measurement of linearly polarized THz radiation, the entrance window is aligned to the Brewster angle of 55.5° to the incident THz beam. The sensitive area features an diameter greater than 30 mm. The NEP is typically $5\,\mu\mathrm{W}/\sqrt{\mathrm{Hz}}$, much higher than that of a Golay cell. The frequency response of this detector is flat, only altered by the transmission of the TPX entrance window and the absorption of the metal film. The detector can be calibrated by external electrical heating of the metal foil with a known power and comparison with the output signal. The absorption of of the film and the transmission of the entrance window can be calibrated with a spectrometer.

Golay cell

A Golay cell is a very broadband IR and THz detector with a fairly flat frequency dependence at room temperature. A scheme of the Golay cell is shown in Fig. 2.6. In a Golay cell, the Terahertz power is measured through the thermal expansion of a gas volume [34]. The cell consists of a gas volume with an entrance window for the Terahertz radiation (e.g. HDPE or diamond) and a flexible membrane. The Terahertz radiation is absorbed in a foil located in the gas volume and subsequently heats the gas. The thermal expansion causes a displacement of the flexible membrane. A LED or laser beam is focused on the flexible membrane. A quadrant photodiode measures the reflection. As a result, the power of the Terahertz radiation heating the gas volume can be detected through the deflection of the membrane and a measure for the irradiance can be given. The Golay cell has a flat frequency dependence over

a large frequency range, depending on the transmission of the entrance window and absorption of the foil in the gas volume. The entrance window features e.g. a 6 mm diameter and can be further increased with an entrance cone, especially important for longer wavelengths with a larger diffraction-limited beam waist. Certain Golay cells feature a NEP of 200 pW/$\sqrt{\text{Hz}}$ [2, p. 183f] at room temperature. A disadvantage of Golay cells is the limited speed of the detector with a time constant of tens of ms, leading to a strong decrease in responsivity towards higher modulation frequencies. Additionally Golay cells are very sensitive to vibrations. The modulation frequency is typically chosen between 10 and 20 Hz for a low NEP. The responsivity of Golay cells typically decreases over time, such that a recalibration of the responsivity becomes necessary. The Tydex Golay cell used in this thesis was therefore recalibrated with an electronic multiplier source and a Thomas Keating power meter.

Pyroelectric detector

A pyroelectric detector measures the heating of a crystal by the THz power. The crystal expands when heated, causing a change of the lattice constant, leading to a change in the dipole moment and electrical surface charge. A capacitor containing the pyroelectric material allows to measure the charge. The speed of the detector depends on the integrated amplifier, electrical capacitance and thermal capacitance. Certain pyroelectric detectors show response times of less than 1 ns [2, p.185 f.], but response times in the range of 10 ms are typical. Pyroelectric elements can also be used to built arrayed detectors. With a sufficient curie temperature of the used material, pyroelectric detectors can operate at room temperature.

The responsivity of the detector can be increased by applying an absorption layer on the pyroelectric material, if the absorption of the pyroelectric material in the desired frequency band is not sufficient.

2.2.2. Optical detector

Mercury cadmium telluride

Mercury cadmium telluride (MCT) is a semiconductor material with a bandgap tunable by the amount of cadmium in the alloy. The bandgap can be chosen such that wavelengths in the IR are absorbed in the semiconductor, enabling the direct detection of MIR radiation. MCT detectors are commercially available as room-temperature or liquid nitrogen cooled detectors for reduction of thermal noise. They are commonly used in Fourier transform infrared spectrometers as photodetectors. Special liquid N_2-cooled MCT detectors with an IF bandwidth in the low MHz range are e.g. used at Helmholtz-Zentrum Dresden-Rossendorf. They are sensitive down to about 8 THz and therefore only cover a small part of the upper THz band.

2.2.3. Electrical detectors

Schottky diode

Schottky diodes exploit the non-linear current-voltage characteristics of a metal-semiconductor junction with a Schottky barrier. Schottky diodes are fast, compact and sensitive detectors for THz radiation at room temperature. They offer the possibility to be used for heterodyne as well as direct detection of sub-THz, THz, and MIR radiation [35]. NEPs of $0.4\,\mathrm{pW}/\sqrt{\mathrm{Hz}}$ [36] have been demonstrated right below the THz band at 88 GHz and values of a few $\mathrm{pW}/\sqrt{\mathrm{Hz}}$ around 600 GHz [37–39]. A spectroscopic detector system has been demonstrated combining multiple sensor elements with different resonant antennas [40].

The I-V characteristic of a Schottky diode is non-linear. The non-linearities are described by the derivatives $\chi^{(j)} = \frac{\partial^j I}{\partial U^j}$. Mixing in a Schottky diode with a non-zero $\chi^{(2)} = \frac{\partial^2 I}{\partial U^2}$ of a THz signal $U_a \cos(\omega_{THz} t)$ and the signal from the local oscillator $U_{LO} \cos(\omega_{LO} t + \varphi)$ calculates as follows:

$$
\begin{aligned}
I &= \chi^{(0)} + \chi^{(1)} \cdot [U_a \cos(\omega_{THz} t) + U_{LO} \cos(\omega_{LO} t + \varphi)] && (2.2)\\
&+ \chi^{(2)} \cdot [U_a \cos(\omega_{THz} t) + U_{LO} \cos(\omega_{LO} t + \varphi)]^2 + \cdots \\
&= \chi^{(0)} + \chi^{(1)} \cdot (U_a \cos(\omega_{THz} t) + U_{LO} \cos(\omega_{LO} t + \varphi)) && (2.3)\\
&+ \frac{\chi^{(2)}}{2}((U_a)^2 + (U_{LO})^2) && (2.4)\\
&+ \frac{\chi^{(2)}}{2}(U_a)^2 \cos(2\omega_{THz} t) && (2.5)\\
&+ \frac{\chi^{(2)}}{2}(U_{LO})^2 \cos(2\omega_{LO} t + 2\varphi) && (2.6)\\
&+ \chi^{(2)} U_{LO} U_a \cos((\omega_{THz} - \omega_{LO})t - \varphi) && (2.7)\\
&+ \chi^{(2)} U_{LO} U_a \cos((\omega_{THz} + \omega_{LO})t + \varphi) + \cdots && (2.8)
\end{aligned}
$$

Term 2.4 represents the self-rectification $\propto U_a^2$ which is also present without local oscillator input ($U_{LO} = 0$). The internal ideal responsivity R_{id} can be calculated to $\mathrm{R}_{id} = 10...19\,\mathrm{A/W}$, depending on the ideality factor of the diode [41].

The mixing term 2.7 oscillates at the intermediate frequency $f_{IF} = f_{THz} - f_{LO}$ and contains information on the phase between the THz and the local oscillator. The second mixing term 2.8 oscillates at a frequency higher than the THz frequency, being not relevant for detection. Additionally there are components at higher harmonics such as the terms 2.5 and 2.6, that are also not relevant for detection.

Field-effect transistor

Field-effect transistors are able to rectify THz radiation well above their maximum frequency of oscillation f_{max} or cutoff frequency f_T. Fast, compact and sensitive room-temperature detectors can be built using FETs. Especially in the last decade strong improvements have lead to very sensitive detectors, as well as FET-based THz

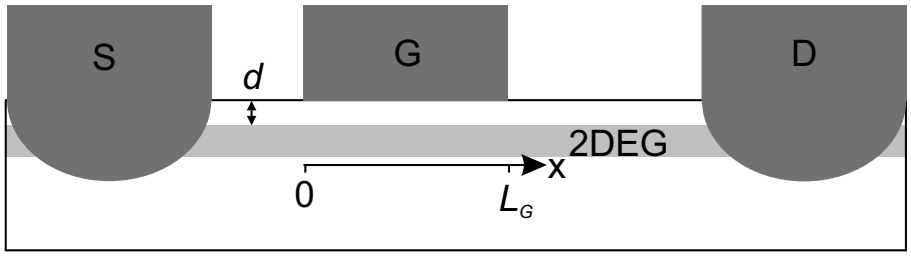

Fig. 2.7: *Scheme of a FET with source (S), gate (G), and drain (D) terminals and a 2-dimensional electron gas (2DEG)-channel. The channel is situated d underneath the surface, the gate has a length of L_G. The THz wave is rectified underneath the gate contact. The THz radiation is fed into the channel directly or through an antenna.*

cameras [42]. Published NEPs of 14 to 20 $\mathrm{pW}/\sqrt{\mathrm{Hz}}$ at 720 and 590 GHz demonstrate the high sensitivity [43; 44]. In high electron mobility transistor (HEMT) devices with short gate lengths, plasma oscillations can further enhance the responsivity at specific frequencies [45–47]. There are various realizations of THz detectors using metal-oxide-semiconductor FETs (MOSFETs)[43; 44; 48; 49] or HEMTs [45–47; 50]. Silicon-based MOSFET rectifiers have the advantage of commercially available well-established foundry processes, compensating disadvantages from the semiconductor such as the rather low mobility in the hundreds of $\mathrm{cm}^2/\mathrm{Vs}$. HEMTs, also known as heterojunction FETs (HFETs) or modulation-doped FETs (MODFETs) feature high electron mobilities through the remote doping of the wide-energy-gap material with an undoped channel and subsequently less impurity scattering. Additionally, oxide charging as in MOSFETs is not present in HEMTs. Fig. 2.7 shows the scheme of a HEMT.

For the study of the plasmonics in 2DEGs and THz absorption, the concept of large-area field-effect transistors has already been used before [51–53]. However, not covering the whole THz band and beyond up to the MIR.

This works builds upon previous work from S. Preu *et al.* on LA-FET detectors for the simultaneous detection of THz and 800 nm pulses, mixing detection with A-FETs, and theoretical studies [54–56]. This work also builds upon own prior work from the master's thesis on GaAs-based A-FETs [9; 57].

3. Theory of Terahertz detection by a field-effect transistor

This chapter discusses the Dyakonov-Shur rectification mechanism, the coupling of THz to the FET, noise sources in a FET, and the thermoelectric detection mechanism. Further, the concept of antenna-coupled and large-area FETs, as well as the (Al)GaAs semiconductor structure are introduced. In the following section, a theoretical model for the detection mechanism inside a FET detector will be derived [9; 29; 41; 48; 55; 58; 59].

3.1. Rectification in an ideal transistor

THz radiation can be fed to the FET either directly to the channel between source and drain contact, as well as through an antenna that enhances the incoupling. In both cases, the THz field is converted to a channel or gate bias. For the rectification of THz radiation, the local gate voltage $U(x,t)$ above threshold U_{th} is modulated by the received THz signal as

$$U(t) \propto U_{THz}(t) = U_a \exp(+j\omega t), \tag{3.1}$$

with the frequency $f = \omega/2\pi$. In a FET, the charge carrier density $n^{(2D)}$ is modulated through the local gate voltage U in the gated region

$$n^{(2D)} = \frac{c\kappa k_B T}{e^2} \ln\left(1 + e^{\frac{eU}{\kappa k_B T}}\right), \tag{3.2}$$

with the thermal energy $k_B \cdot T$, the gate-channel capacitance per unit area c, and the ideality factor κ. Above threshold ($U \gg k_B T/e$) Eq. 3.2 can be approximated, obtaining a linear relation for the charge carrier density and the THz voltage: $en^{(2D)} = cU(t) \propto U_{THz}(t)$.

In the channel, the charge carrier velocity $v = \mu E_{THz}$ is modulated by the THz voltage applied between drain and source, $U_{DS} \propto U_{THz}$. μ denotes the charge carrier mobility $\mu = e\tau/m^*$, with m^* the effective mass of the charge carriers (e.g. $m^* = 0.063\, m_0$ for electrons in GaAs), and τ the effective scattering time. The simultaneous modulation of the charge carrier density $n^{(2D)}$ and the charge carrier velocity v in the channel of the FET leads to a rectified part in the resulting current density J of the channel:

$$J = en^{(2D)} \cdot v \propto U_{THz}^2 \propto U_a^2(1 + \cos(2\omega t)). \tag{3.3}$$

The channel current in a heterojunction FET can be described by the textbook square-law formula [55; 60]

$$I_d = \frac{\mu c W}{L} \cdot \begin{cases} (U_{GS} - U_{th}) \cdot U_{DS} - \frac{1}{2}U_{DS}^2 & \text{for } U_{DS} \geq 0 \\ (U_{GS} - U_{th}) \cdot U_{DS} + \frac{1}{2}U_{DS}^2 & \text{for } U_{DS} < 0. \end{cases} \tag{3.4}$$

Eq. 3.4 shows, that the boundary conditions i.e. incoupling of the THz wave from source with floating or fixed potential at the drain or incoupling of the THz wave from the drain, as well as the phase between $U_{GS} - U_{th}$ and U_{DS} determine the magnitude of the rectified current, which can be represented by the time averaged Eq. 3.4. However the second derivative $\frac{\partial^2 I_d}{\partial U_{DS}^2}$ of this model at $U_{DS} = 0$ does not exist, or would have to be zero [60]. Under experimental conditions, the operation around $U_{DS} = 0$, without a DC bias is beneficial for low noise operation.

Therefore, the rectification in the 2D electron gas (2DEG) is derived using hydrodynamic equations, the so-called Dyakonov-Shur model [61]. The equation of motion and the continuity equation read

$$\frac{\partial v}{\partial t} + v\frac{\partial v}{\partial x} + \frac{v}{\tau} = -\frac{e}{m^*}\frac{\partial U}{\partial x} \tag{3.5}$$

$$\frac{\partial n}{\partial t} + \frac{\partial (nv)}{\partial x} = 0, \tag{3.6}$$

with the scattering time τ and the effective mass m^*. The term v/τ in Eq. 3.5 accounts for the external scattering through impurities or phonons, thus for frequencies smaller than $\omega\tau < 1$ the plasmons are overdamped. In literature this case is mostly referred to as non-resonant regime, whereas for frequencies $\omega\tau \geq 1$ plasmons can be excited in the so-called plasma-resonant regime.

For the separation of the time derivative, the following ansatz with a harmonic time dependence of the excitation frequency is chosen [48; 58]

$$U(t) = U_0 + \frac{1}{2}\sum_m \left(U_m \exp\left(+jm\omega t\right) + U_m^* \exp\left(-jm\omega t\right)\right) \tag{3.7}$$

$$n^{(2D)}(t) = n_0 + \frac{1}{2}\sum_m \left(n_m \exp\left(+jm\omega t\right) + n_m^* \exp\left(-jm\omega t\right)\right) \tag{3.8}$$

$$v(t) = v_0 + \frac{1}{2}\sum_m \left(v_m \exp\left(+jm\omega t\right) + v_m^* \exp\left(-jm\omega t\right)\right), \tag{3.9}$$

with the averaged quantities U_0, n_0, and v_0, and U_m, n_m, and v_m, varying with $m\omega$, m being an integer.

Transmission line model

In the following derivation, a time dependence of the shape $\exp(+j\omega t)$ is chosen. The resulting impedance of a capacitance $Z_C = -j/(\omega C)$ has therefore a negative imaginary part. Choosing the other sign convention with a time dependence of $\exp(-j\omega t)$, or as also used in literature, $\exp(-i\omega t)$, causes only a substitution $+j \to -i$ and results in $Z_C = +i/(\omega C)$ with positive sign. Including U_a to the first order for Eq. 3.5 and Eq. 3.6, one obtains the following equations [58; 62]:

$$\frac{\partial v_1}{\partial t} + \frac{v_1}{\tau} = -\frac{e}{m^*}\frac{\partial U_1}{\partial x} \tag{3.10}$$

$$\frac{\partial n_1}{\partial t} + n_0\frac{\partial v_1}{\partial x} + v_0\frac{\partial n_1}{\partial x} = 0. \tag{3.11}$$

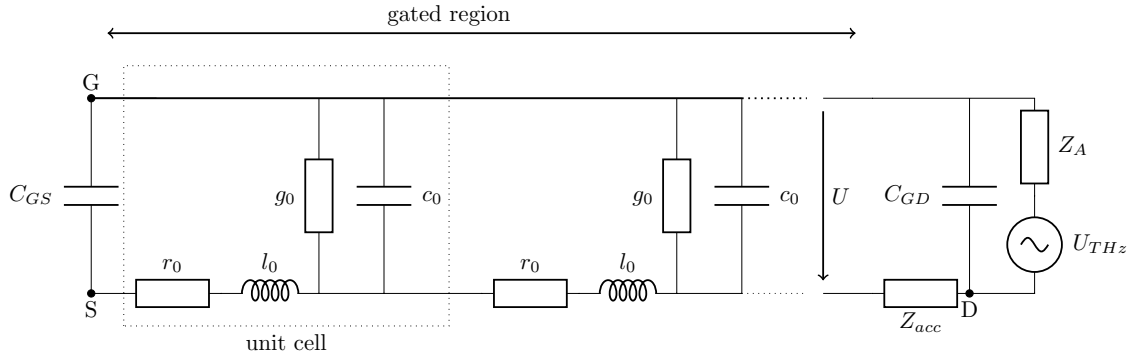

Fig. 3.1: *Equivalent circuit of the rectification in the FET as transmission line model. Adapted from [29] ©IEEE 2018.*

The term $v_0 \frac{\partial n_1}{\partial x}$ can be neglected for the case of low DC channel bias ($U_{DS} \approx 0\,\mathrm{V}$). Reformulating Eq. 3.10 and Eq. 3.11, the following equations are obtained:

$$\frac{\partial U_1}{\partial x} = -n_0 eW \left(\frac{m^*}{n_0 e^2 \tau W} + \tau \frac{m^*}{n_0 e^2 \tau W} \frac{\partial}{\partial t} \right) v_1 \tag{3.12}$$

$$n_0 eW \frac{\partial v_1}{\partial x} = -\left(0 + eW \frac{\partial n}{\partial U} \frac{\partial}{\partial t} \right) U_1. \tag{3.13}$$

Taking finite gate leakage into account ($g_0 \neq 0$) Eq. 3.12 and Eq. 3.13 reduce to the telegrapher's equations for a transmission line with $I_1 = e n_0 v_1 W$ [29; 55; 63; 64]:

$$\frac{\partial}{\partial x} U_1 = -(r_0 + l_0 \frac{\partial}{\partial t}) I_1 \tag{3.14}$$

$$\frac{\partial}{\partial x} I_1 = -(g_0 + c_0 \frac{\partial}{\partial t}) U_1, \tag{3.15}$$

where $c_0 = cW = \epsilon_0 \epsilon_r W/d = eW \frac{\partial n_0}{\partial U_0}$ is the gate-channel capacitance per unit length, g_0 the gate-channel conductance per unit length, $r_0 = m^*/(n_0 e^2 \tau W)$ the channel's resistance and $l_0 = \tau r_0$ the channel's inductance per unit length. The corresponding equivalent circuit is shown in Fig. 3.1, additionally including the access impedance Z_{acc}, radiation impedance Z_A, shunt capacitance C_{GS}, and capacitance C_{GD}, which are discussed in the following section for the incoupling of the THz bias.

Eq. 3.14 and Eq. 3.15 for current and voltage can be combined to a single equation for the voltage as

$$\frac{\partial^2}{\partial x^2} U_1 + l_0 c_0 U_1 = (r_0 c_0 + g_0 l_0) \frac{\partial}{\partial t} U_1 + g_0 r_0 U_1. \tag{3.16}$$

The general ansatz for the solution of the Equations 3.14 and 3.15, or Eq. 3.16 is $U(x) = U_x \exp(-\gamma x) + U_{xr} \exp(+\gamma x)$

$$\gamma = \pm \sqrt{(r_0 + j\omega l_0)(g_0 + j\omega c_0)} \approx \pm \sqrt{r_0 (1 + j\omega\tau)(j\omega c_0)} = \pm \frac{1}{L_{eff}} \pm jk, \tag{3.17}$$

with the real part being just the inverse of the effective rectification length L_{eff} of the THz wave in the gated area and the wave vector k. g_0 is typically small, so it can be neglected for frequencies in the MHz, GHz, and THz range and is set to 0 in the following calculations. The sign of γ has to be chosen such to obtain a wave decaying along the channel depending on the direction of the wave and incoupling of the THz wave, as the device is operated above f_T. The amplitude of the THz wave at the beginning of the gated area is set to U_x.

The (frequency dependent) effective rectification length $L_{eff}(\omega)$ calculates to

$$L_{eff}(\omega) = \left(\sqrt{1+\omega^2\tau^2} - \omega\tau\right)^{-1/2} \cdot L_{eff}^{nr}, \tag{3.18}$$

with the effective rectification length $L_{eff}^{nr} = \sqrt{2}/\sqrt{\omega r_0 c_0}$ in the non-resonant approximation ($\omega\tau < 1$, $\omega l_0 \ll r_0$). The THz wave in the FET is not amplified, but rectified and subsequently the THz wave decays in the gated area. The goal is the efficient conversion of THz radiation into a DC current or voltage. The effective rectification length L_{eff} gives the decay length of the THz wave in the transistor. A FET with a long channel, where all the THz power is rectified, is preferred for an efficient broadband detector. The amplitude of the reflected wave U_{xr} is small in the long channel limit and can be neglected. A gate length of 2 to $3L_{eff}$ suffices for good performance. For longer gates, undesired serial impedances originate from an excess length of the gate as discussed in the following section.

In contrast to the non-resonant approximation L_{eff}^{nr} (not being valid for the high frequency limit), the general non-resonant ($\omega\tau < 1$) and resonant ($\omega\tau \geq 1$) effective rectification length $L_{eff}(\omega)$ approaches a constant value in the high frequency limit,

$$L_{eff}(\infty) = \lim_{\omega\to\infty} L_{eff}(\omega) = 2\sqrt{\frac{\tau}{2r_0c_0}}. \tag{3.19}$$

$L_{eff}(\infty)$ can be expressed by material parameters and the geometrical design of the FET

$$L_{eff}(\infty) = 2e\tau\sqrt{\frac{n^{(2D)}d}{m^*\epsilon_0\epsilon_r}} = 2\mu_{DC}\sqrt{\frac{m^*n^{(2D)}d}{\epsilon_0\epsilon_r}}. \tag{3.20}$$

For an exemplary HEMT with a mobility of $6022\,\mathrm{cm}^2/\mathrm{Vs}$, a barrier thickness of 25 nm, and a carrier concentration of $5.3\cdot10^{11}\,\mathrm{cm}^2$ the effective rectification length is $0.3\,\mu$m. Silicon-based FETs typically feature a much lower mobility in the range of $110\,\mathrm{cm}^2/\mathrm{Vs}$ at a similar effective barrier thickness d/ϵ_r [48]. The effective rectification length of silicon-based FET with and charge carrier concentrations in the range of 1 to $10\cdot10^{11}\,\mathrm{cm}^2$ is therefore much shorter with 5 to 14 nm. The fabrication of efficient silicon-based FETs requires therefore ideally high-end fabrication technology in the 22 nm node or better for frequencies on the upper end of the THz band. For low frequencies, this condition is relaxed. In contrast, HEMTs allow fabrication with simple UV-contact lithography.

(a) drain coupling (b) gate source coupling

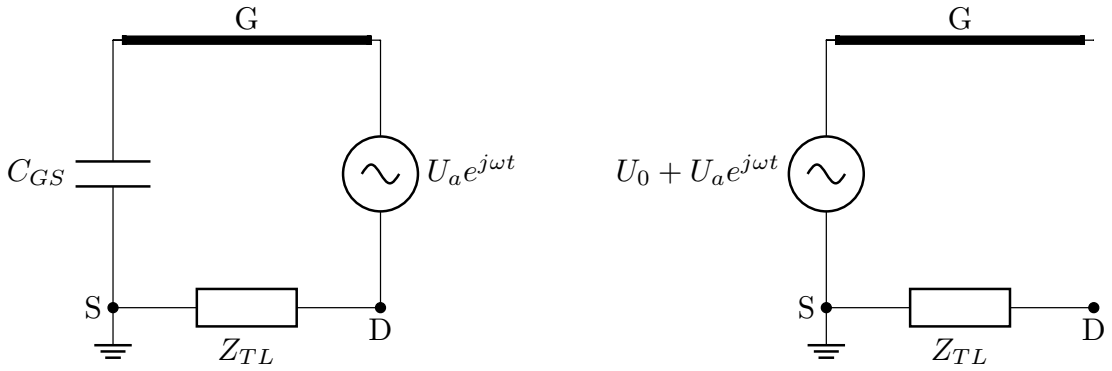

Fig. 3.2: *a) Schematic of incoupling from the drain side of the FET. The source-gate capacitor ensures the same AC potential for source and gate. b) Schematic of incoupling from the source side of the FET.*

In the following calculations, the rectification mechanism will be derived for the long-channel limit ($L > L_{eff}$) for both the non-resonant ($\omega\tau < 1$), as well as the plasma-resonant case ($\omega\tau \geq 1$).

The impedance of the active rectifying element Z_{TL} calculates to

$$Z_{TL} = \sqrt{\frac{r_0 + j\omega l_0}{g_0 + j\omega c_0}} \approx \sqrt{\frac{r_0(1 + j\omega\tau)}{j\omega c_0}}. \tag{3.21}$$

Rectification

The THz bias causes a rectified read-out bias ΔU, that is derived including the second order of the THz bias U_a. Substituting the harmonic ansatz Eq. 3.7, Eq. 3.8, and Eq. 3.9 into Eq. 3.5 and Eq. 3.6, the following stationary (time independent) terms are obtained [48]

$$\frac{\partial}{\partial x}\left(\frac{eU_0}{m^*} + \frac{v_1 v_1^*}{4}\right) + \frac{v_0}{\tau} = 0 \tag{3.22}$$

$$\frac{\partial}{\partial x}\left(\frac{e^2 n_0}{m^* c} v_0 + \frac{e}{m^*}\frac{v_1 U_1^* + v_1^* U_1}{4}\right) = 0. \tag{3.23}$$

For the case of incoupling from the drain side with a strong AC coupling between source and gate the boundary conditions are (cf. Fig. 3.2a))

$$U_1(x = L) = -U_a \quad \& \quad U_1(x = 0) = 0. \tag{3.24}$$

In this case source and gate are set to the same AC potential. The ansatz for the

voltage and charge carrier velocity for these boundary condition evaluates to [48]

$$U_1 = -U_a \frac{\sin \gamma x}{\sin \gamma L} \tag{3.25}$$

$$v_1 = \frac{\omega c U_a}{j \gamma e n_0} \frac{\cos \gamma x}{\sin \gamma L}. \tag{3.26}$$

The stationary velocity v_0 is obtained from Eq. 3.23. Now the rectified voltage ΔU can be calculated by solving and integrating Eq. 3.22 for U_0

$$\Delta U = -\frac{m^*}{e} \frac{v_1 v_1^*}{4} \Big|_{x=0}^{x=L} + \frac{m^* c}{4 e^2 n_0 \tau} \int_0^L (v_1 U_1^* + v_1^* U_1) \, \mathrm{d}x. \tag{3.27}$$

The rectified voltage ΔU can be simplified to

$$\Delta U = U_a^2 \frac{c}{4 e n_0} \eta_{p,d}. \tag{3.28}$$

With the phase velocity $v_{ph} = \sqrt{e^2 n_0 / (mc)}$, ΔU can be written as $U_a^2 \frac{e}{4 m^* v_{ph}^2} \eta_{p,d}$ to obtain the same formula as in ref. [48]. The plasmonic efficiency $\eta_{p,d}$ is defined as [48]

$$\eta_{p,d} = 1 + \frac{2\omega\tau}{\sqrt{1 + (\omega\tau)^2}} \frac{\sinh^2(L/L_{\text{eff}}) - \sin^2(Lk)}{\cosh^2(L/L_{\text{eff}}) - \cos^2(Lk)}, \tag{3.29}$$

with the complex wave vector $\gamma = \frac{1}{L_{\text{eff}}} + jk$ from Eq. 3.17.

The corresponding rectified current can be obtained by dividing the voltage with the corresponding DC resistance of the channel $R_{ch} = L_{eff} \cdot r_0$

$$\Delta I = U_a^2 \frac{c_0 \mu}{4 L_{eff}} \eta_{p,d}. \tag{3.30}$$

The intrinsic responsivity $\mathcal{R}_I^{id,FET}$ of the FET is calculated by referencing the response of the FET with the THz power at the FET $P_{THz}^{FET} = \frac{U_a^2}{2 r_0 L_{eff}}$. The intrinsic current responsivity evaluates to $\mathcal{R}_I^{id,FET} = \frac{c}{2 e n_0}$. Considering operation close to or below threshold, an intrinsic responsivity of 10 to 20 A/W can be expected, being in the same range as Schottky diodes [41; 48]. However, this intrinsic responsivity is obtained at a very high channel impedance that leads to low coupling efficiencies. The intrinsic responsivity does also not consider the radiation impedance of an antenna. The following section discusses the incoupling with an antenna and respective coupling efficiencies.

For this ideal treatment of the HEMT structure, the FET is symmetric regarding the gate and drain contacts. Exchanging the side of the incoupling gives the same absolute response: Incoupling the THz wave from the source side with the AC ground at the drain with the boundary conditions (cf. Fig. 3.2b))

$$U_1(x = 0) = U_a \quad \& \quad U_1(x = L) = 0 \tag{3.31}$$

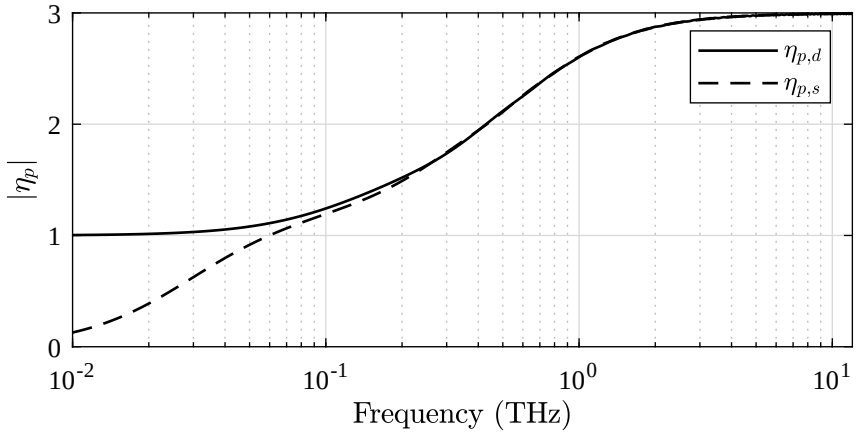

Fig. 3.3: *Comparison of the plasmonic efficiency $\eta_{p,d}$ and $\eta_{p,s}$ for a HEMT in the long channel limit with $v_{ph}\tau/L = 0.12$.*

gives the same magnitude of the rectified current or voltage as the first discussed case for incoupling from the drain side with fixed source potential, only the sign changes.

For HEMTs with short gate lengths ($v_{ph}\tau/L \gg 1$), $\eta_{p,d}$ shows a strong frequency and gate bias dependent oscillation at the plasma frequencies ω_p [45; 58]. The short channel acts a cavity for the plasmons, showing resonances in the response. However, experimentally the resulting increase does not feature multiple orders of magnitude responsivity enhancement as expected taking only $\eta_{p,d}$ into account [50]. It is still under discussion, if the multiple order of magnitude enhancement in $\eta_{p,d}$ for the short channel limit can be accessed experimentally in form of an orders of magnitude responsivity enhancement or if it is cloaked by damping from additional parasitic resistances [65].

The transistors in this thesis are designed for the long channel limit with over-damped plasma waves, therefore there are no strong oscillations in the plasmonic efficiency $\eta_{p,d}$, but a smooth transition from a value of 1 to 3 from the low frequency limit to the high frequency limit as shown in Fig. 3.3.

For the case of incoupling between source and gate without grounded AC potential at drain side, the boundary conditions are

$$U_1(x = 0) = U_a \quad \& \quad v_1(x = L) = 0 \tag{3.32}$$

The rectified voltage ΔU for the different incoupling can also be described by Eq. 3.28 with a different plasmonic efficiency $\eta_{p,s}$ [58]

$$\eta_{p,s} = 1 + \frac{2\omega\tau}{\sqrt{1+(\omega\tau)^2}} - \frac{1 + \frac{2\omega\tau}{\sqrt{1+(\omega\tau)^2}}\cos(2Lk)}{\sinh^2(L/L_{\text{eff}}) + \cos^2(Lk)}. \tag{3.33}$$

$\eta_{p,s}$ shows a smooth transition from 0 to 3 in the long channel limit as shown in Fig. 3.3 in comparison with $\eta_{p,d}$.

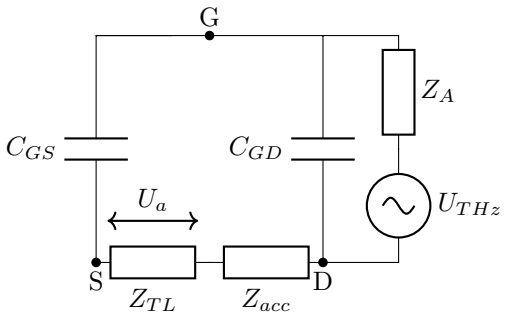

Fig. 3.4: *Equivalent circuit of the incoupling to the rectifying element in the FET.*

In the long channel limit ($L \gg L_{eff}$, respectively $v_{ph}\tau/L \ll 1$) the plasmonic efficiency for both cases $\eta_{p,s}$ and $\eta_{p,d}$ can both be approximated by $\eta_p = 1 + \frac{2\omega\tau}{\sqrt{1+(\omega\tau)^2}}$ in the high frequency limit ($\omega\tau \gg 1$).

Coupling THz to a FET with strong gate-source coupling can thus lead to a different rectified output compared to a FET with undefined potential at the end of the channel. For a HEMT with $v_{ph}\tau/L = 0.12$ as processed in this thesis, the respective plasmonic efficiency $\eta_{p,d}$ and $\eta_{p,s}$ shows a strong difference below 100 GHz. For a higher responsivity in the detection of THz radiation, a defined potential through strong gate-source coupling in the transistor is therefore preferred for low frequencies ($\omega\tau < 1$).

3.2. Coupling efficiency from antenna to transistor

The antenna couples the received THz radiation as a bias to the FET. The real radiation resistance R_A couples the received THz power of [66]

$$P_{THz} = \frac{1}{2R_A} U_{THz}^2 \tag{3.34}$$

to the circuit shown in Fig. 3.4. Z_A is the complex radiation impedance, Z_{acc} the access impedance, C_{GD} the gate-drain capacitance, C_{GS} the gate-source capacitance, and Z_{TL} the impedance of the actual rectifying element. Z_{TL} is modeled using the transmission line theory (Eq. 3.21). To ensure a well-defined AC potential and asymmetry, C_{GS} can be chosen large to act as an AC short for gate and source. The loss of the current in the antenna due to R_L is neglected, therefore the antenna (input) impedance $Z_A = R_L + Z_{rad}$ equals the radiation impedance Z_{rad}.

The access impedance Z_{acc} is dominated by the ungated parts of the channel and the DC conductance $\sigma_{DC}^{(2D)}$ can be extended to higher frequencies with the Drude model

$$\sigma^{(2D)}(\omega) = \frac{\sigma_{DC}^{(2D)}}{1 + j\omega\tau}, \tag{3.35}$$

and the DC conductivity $\sigma_{DC}^{(2D)} = en^{(2D)}\mu_{DC}$ [29]. The access impedance calculates to

$$Z_{acc} = \frac{1}{\sigma^{(2D)}(\omega)} \cdot \frac{L_{acc}}{W} = \frac{1}{\sigma_{DC}^{(2D)} W} L_{acc} + j\frac{\omega\tau}{\sigma_{DC}^{(2D)} W} L_{acc} = r_0^{acc} L_{acc} + j\omega l_0^{acc} L_{acc}, \tag{3.36}$$

with W being the width of the channel, and L_{acc} the length of the access part of the channel, r_0^{acc} the resistance per unit length, and $l_0^{acc} = \tau r_0^{acc}$ the inductance per unit length. The resistance per unit length is $r_0^{acc} = r_0^{(2D)}/W$ with the 2DEG sheet resistance $r_0^{(2D)}$.

The resistance r_0^{acc} and inductance l_0^{acc} in the ungated area are labeled with the superscript *acc* to account for the difference to the gated area with the resistance r_0 and inductance l_0. The charge carrier density $n^{(2D)}$ between the gated and ungated area may differ, through modification of the semiconductor surface or due to the presence of the gate metal.

The resulting voltage responsivity $\mathcal{R}$ and current responsivity $\mathcal{R}_I$ evaluate to

$$\mathcal{R} = \frac{\Delta U}{P_{THz}} = \mathcal{R}^{id,0}\eta_p\eta_{Op}\eta_A\eta_{El}\eta_{DCV}\eta_a \tag{3.37}$$

$$\mathcal{R}_I = \frac{\Delta I}{P_{THz}} = \mathcal{R}_I^{id,0}\eta_p\eta_{Op}\eta_A\eta_{El}\eta_{DCI}\eta_a, \tag{3.38}$$

with the following quantities:

- ideal voltage responsivity $\mathcal{R}^{id,0} = \frac{cR_a}{2en_0}$ in the low frequency limit
- ideal current responsivity $\mathcal{R}_I^{id,0} = \frac{\Delta I_d}{P_{THz}} = \mathcal{R}^{id,0}/R_{ch} = \frac{\mu c_0 R_a}{2L_{eff}}$ in the low frequency limit
- plasmonic efficiency $\eta_p = \eta_{p,d}$, or $\eta_p = \eta_{p,s}$, respectively
- optical efficiency η_{Op}
- aperture efficiency η_A
- electrical efficiency $\eta_{El} = |U_a/U_{THz}|^2$
- efficiency of the read-out circuit η_{DCV} for voltage and η_{DCI} current read-out
- amplitude suppression η_a, for the read-out of short pulses with a direct detector.

The optical efficiency accounts for loss through polarization mismatch e.g. 50% for linearly polarized THz wave and a circularly polarized antenna, reflection of the THz radiation before coupling to the antenna e.g. 30% through a silicon lens. The aperture efficiency η_A accounts for clipping of the spatial beam waist to the detector aperture.

For $L_{eff} = 0.3\,\mu$m, a radiation resistance of $72\,\Omega$, and a mobility of $5850\,\mathrm{cm}^2/\mathrm{Vs}$, the ideal current responsivity calculates to $\mathcal{R}^{id,0} = 3.9\,\mathrm{A/W}$ in the low frequency limit.

With more negative gate bias, the responsivity increases. Above threshold $U \gg k_B T/e$, Eq. 3.2 can be linearized and the responsivity becomes inversely proportional to the gate bias as

$$\mathcal{R}^{id,0} \propto \frac{1}{U} = \frac{1}{U_{GS} - U_{th}}. \tag{3.39}$$

The electrical efficiency quantifies the losses, when coupling THz radiation from the antenna to the actual rectifying element

$$\eta_{El} = \left| \frac{Z_{TL}}{Z_{dev} + Z_A} \left(1 - \frac{Z_{dev}}{Z_{C_{GD}}} \right) \right|^2, \tag{3.40}$$

with $Z_{dev} = [(Z_{TL} + Z_{acc})^{-1} + (Z_{C_{GD}})^{-1}]^{-1}$, and $Z_{C_{GD}} = 1/(j\omega C_{GD})$. The electrical efficiency approaches $\eta_{El} \to 1$ for $Z_{TL} \gg Z_A$ and $Z_{GD} \to \infty$, for impedance matching and $Z_{GD} \to \infty$, it is $1/2$.

A high impedance of the rectifying element Z_{TL} leads typically also to a higher access impedance Z_{acc}, as the channel is realized with the same semiconductor in the gated and ungated area for HEMTs. However, though modification of the semiconductor surface in the ungated area, $n^{(2D)}$ may be increased, which leads to a smaller Z_{acc}. For smaller values of Z_{TL} and Z_{acc}, impedance matching to the radiation impedance Z_A is typically a desirable choice.

For impedance matching, the radiation impedance Z_A should be chosen as the complex conjugate of the device impedance $Z_A = Z^*_{dev}$. This can be achieved with resonant antennas in narrow bands. In the high frequency limit, the gate-drain capacitance C_{GD} and access impedance Z_{acc} dominate the $\frac{1}{f^2_{RC}}$ roll-off in η_{El}. The product of gate-drain capacitance C_{GD} and the access impedance Z_{acc} should therefore be minimized.

The optimization for maximum electrical coupling efficiency η_{El} does not necessarily lead to maximum responsivity $\mathcal{R}_I$ in all cases, as the magnitude of the incoupled THz bias depends on the radiation resistance. Therefore the product $\mathcal{R}_I \propto R_A \cdot \eta_{El}$ needs to be optimized by careful design of the antenna as well as device parameters. For the read-out efficiency in the DC limit, the reactances of the previous expressions an be neglected. The definition of the read-out efficiency η_{DC} for the voltage read-out is

$$\eta_{DCV} = \frac{R_{measV}}{R_{ch} + R_{acc} + R_{measV}}, \tag{3.41}$$

with the internal resistance R_{measV} of the measurement device. For a lock-in amplifier with a typical internal resistance R_{measV} in the MΩ range and thus fulfilling the condition $R_{measV} \gg R_{TL} + R_{acc}$, the efficiency approaches $\eta_{DC} \to 1$.

For a current measurement, the read-out efficiency evaluates to

$$\eta_{DCI} = \frac{R_{ch}}{R_{ch} + R_{acc} + R_{measI}}. \tag{3.42}$$

R_{measI} denotes the internal resistance of the measurement electronics such as an transimpedance amplifier, and is ideally close to zero. For the detection of short pulses below the time constant of the measurement electronics, the amplitude efficiency η_a has to be taken into account as detailed in the following chapter (cf. Eq. 4.11).

The calculated response considers only a well-defined incoupling to either the drain or source side of the transistor. A well-defined incoupling requires asymmetry in the transistor. Therefore, the intrinsic symmetry between the ohmic source and drain contacts needs to be broken. For a symmetric design, the THz power is fed to both sides of the channel leading to superposing rectified signals that cancel each other out [49; 67].

3.3. Noise sources and detector sensitivity

There are several noise sources present, measuring THz radiation with a direct detector. The *total noise* $U_{N,tot}$, resulting from single, uncorrelated noise contributions $U_{N,i}$ can be calculated as $U_{N,tot} = \sqrt{\sum_i U_{N,i}^2}$. In this section, a brief overview of different noise sources is given:

Measurement electronics are used to measure the rectified signal from a direct detector, having their own noise limit, being added to the rectified signal from the direct detector. A lock-in amplifier with measurement bandwidth Δf has a typical noise level of $U_N/\sqrt{\Delta f} \approx 5\,\mathrm{nV}/\sqrt{\mathrm{Hz}}$, a longer measurement time therefore decreases the voltage noise as $\propto \sqrt{1/T} \propto \sqrt{\Delta f}$. Smaller signals can also be measured by including a low noise pre-amplifier, that amplifies the signal above the noise level of the lock-in amplifier. A current is mostly measured by using a transimpedance amplifier with current input and voltage output.

In a THz transmission measurement, as used in spectroscopy, a *modulation* of the THz source is widely used to counteract influence from thermal radiation in the background. A lock-in amplifier allows to measure the demodulated signal with a strongly suppressed noise. Without modulation there can be a strong influence from black body radiation sources disturbing the measurement. Additionally a high modulation suppresses potential $1/f$ *noise* in measurement electronics at DC.

In the FET rectifier itself *thermal noise* $U_N = \sqrt{4k_BTR\Delta f}$ is generated. For the ideal transistor, $R_{DS} = R_{ch}$ has to be considered as a noise source, for a real transistor additional serial resistors have to be included $R_{DS} = R_{ch} + R_{acc}$. Approaching the threshold of the FET, the resistance of the channel increases, and subsequently also the generated noise increases. The dependence from the temperature T further shows the challenges of a sensitive detector for room-temperature operation with $T \approx 300\,\mathrm{K}$, in contrast to liquid-He-cooled devices at $T \approx 4\,\mathrm{K}$.

A current of quantified charge carriers such as electrons generates *shot noise* in the measured signal. For the case of a low channel bias $U_{DS} \approx 0$ in a FET, the thermal noise dominates the total noise and the shot noise can be neglected.

The *NEP* of an ideal FET can be calculated by dividing the thermal noise of the channel $\sqrt{4k_BTR_{ch}}$ by the ideal responsivity $\mathcal{R}^{id,0}$ and the measurement bandwidth

$$\mathrm{NEP}_{id} = \frac{U_N}{\mathcal{R}^{id,0}\sqrt{\Delta f}} = \sqrt{4k_B T L r_0}\frac{2en_0}{cR_a}. \tag{3.43}$$

For a semiconductor with $n_0 = 4.6 \cdot 10^{11}\,1/\mathrm{cm}^2$, $\mu = 5900\,\mathrm{cm}^2/\mathrm{Vs}$, and a radiation resistance of $R_A = 72\,\Omega$ of a typical broadband antenna, an ideal NEP of $4\,\mathrm{pW}/\sqrt{\mathrm{Hz}}$ is expected at room temperature.

3.4. Thermoelectric detection mechanism

The introduced (plasmonic) Dyakonov-Shur rectification mechanism is not the only mechanism which is able to generate a THz induced DC current or voltage. An additional mechanism is due to thermoelectric effects. The asymmetric coupling of THz power to semiconductors leads to a local heating of the electron gas. The local temperature difference results in diffusion currents and hence a DC voltage by the thermoelectric effect or Seebeck effect [68–72]. The electron diffusion current is proportional to the spatial gradient of the product of local charge carrier Temperature T_e and electron density $n^{(2D)}$

$$J_d = k_B \frac{\partial}{\partial x}\left(\mu n^{(2D)} T_e \frac{F_1}{F_0}\right), \tag{3.44}$$

with the Fermi-Dirac integral $F_m(x) = \int_0^\infty \frac{t^m}{\exp(t-x)+1}\mathrm{d}t$. The resulting diffusion current depends on the geometry of the transistor, the incoupling of THz radiation, and on the charge carrier density gradient between gated $n^{(2D)}$ and ungated areas $n_{acc}^{(2D)}$. The thermoelectric contribution is therefore also expected to depend on the gate bias, which influences the charge carrier density in the gated area $n^{(2D)}$. The thermoelectric diffusion has opposite direction compared to the other terms of the hydrodynamic equation Eq. 3.5. It can therefore superimpose the read-out signal from the Dyakonov-Shur rectification.

The heating of the charge carriers does not depend on the frequency of the THz radiation. Therefore, the thermoelectric contribution in a FET could become dominant at high frequencies, due to the f^{-2} roll-off in η_{El} for the Dyakonov-Shur mechanism. However, a different coupling to the FET channel may potentially alter the heating of the charge carriers for a different polarization or frequency. The quantitative contribution of this effect to the total THz induced currents in the FET is not fully understood and requires further investigation.

3.5. Concept of antenna-coupled and large-area field-effect transistors

Broadband antennas

FETs are fabricated on the semiconductor surface. Patch antennas can be placed directly on the semiconductor surface and connected directly to the FET for integration of the antenna during fabrication on a conductive substrate. The broadband operation of a detector requires a broadband antenna with a radiation impedance Z_A being ideally constant over the desired frequency band. Resonant antennas with $Z_A = Z_{dev}^*$ can only be designed for operation in a narrow band. The bandwidth of a dipole antenna can be increased by widening the antenna to a bow-tie as shown in Fig. 3.5a). Self-complementary antennas are another possible choice that can be implemented on non-conductive substrates. They offer a constant radiation resistance within the limits of their size. Due to Babinet's principle the radiation resistance of a self-complementary antenna can be calculated analytically as [73; 74]

$$Z_A Z_A^* = \frac{Z_0^2}{4n^2} \tag{3.45}$$

$$Z_A = R_A = \frac{Z_0}{2n_{eff}} = \frac{Z_0}{\sqrt{2(\epsilon_1 + \epsilon_2)}}, \tag{3.46}$$

with Z_0 as the wave impedance of free space and the effective refractive index $n_{eff} = \sqrt{\epsilon_1 + \epsilon_2}/\sqrt{2}$ of the interface of materials with the dielectric constants ϵ_1 and ϵ_2, respectively. For self-complementary antennas, the theoretical radiation impedance is real. For the air-GaAs interface a radiation resistance of $R_A = 72\,\Omega$ is obtained. Fig. 3.5b) shows a log-periodic self-complementary antenna with linear polarization. As a result of the discrete arms, the linear polarization axis oscillates with f around an axis perpendicular to the central bow-tie. The resonance frequency of a single arm is $f_n = 2c/(\pi n_{eff}(r_n + R_n))$ [75]. The spacing of the arms increases exponentially, with a constant increase between neighboring arms ($r_n/r_{n+1} = const$). The lowest frequency is limited by the largest arm, the highest frequency by the smallest arm. The ultimate limitation is the required space for the semiconductor device in the middle of the antenna. The semiconductor device also alters the characteristics of the antenna, especially for high frequencies, where the radiation induced current in the antenna is located closer to the semiconductor device.

A self-complementary logarithmic spiral antenna as shown in Fig. 3.5c) features a circular polarization and therefore avoids a frequency dependent change in polarization within its operation range. The inner and outer arms of the logarithmic spiral antenna are described by the formula $r = r_0 \exp(a(\varphi - \varphi_0))$ and $R = R_0 \exp(a(\varphi - \varphi_0))$ with $r_0 < R_0$, respectively. For real antennas with a finite size, the minimum operation frequency is determined by the outer dimensions of the spiral, the maximum operation frequency by the size of the semiconductor device connected to the spiral antenna in the center of the antenna. The spiral antennas used in this thesis have 1.5 turns and a flare rate of $a = 0.34$. For a 15 μm wide semiconductor

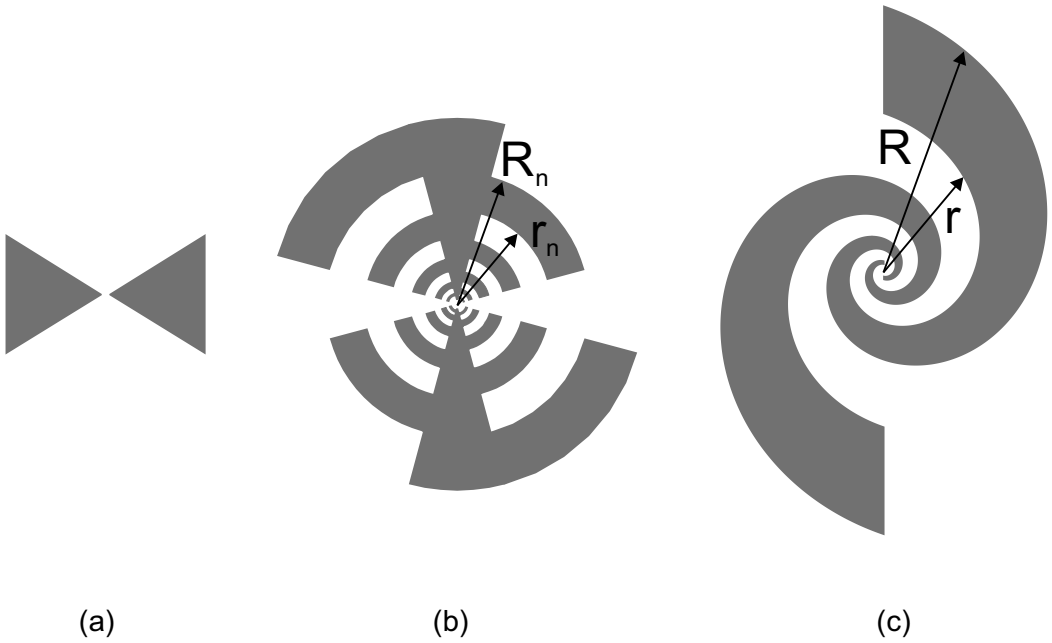

Fig. 3.5: *a) Bow-tie antenna for linear polarization. b) Self-complementary log periodic antenna. c) Self-complementary spiral antenna with circular polarization.*

device in the center of the antenna altering the theoretical self-complementary design CST simulations show a R_A oscillating around 72 Ω between 50 GHz and 0.7 THz. The simulated polarization is circular below ≈ 1 THz, reaching an ellipticity (ratio between the polarization half axes) of 3 at 1.5 THz.

Within this thesis, the radiation impedance Z_A is simulated from 50 GHz up to 12 THz. Already at 5 THz, the outer part of the antenna with mm dimensions shows a negligible surface current, only the inner part of the antenna with the device in the tens of μm range shows a significant surface current. For a simulation at very high frequencies, the outer part of the antenna can thus be excluded from simulation. The simulation is divided into three different frequency areas with different dimensions of the simulated model, to account for the finite amount of memory (24 GB RAM) in the PC used for the simulations. The three different simulation models are overlapping in frequency to evaluate the influence from a cut of the model at high frequencies, by comparing the different simulation models for the same frequency: Full model simulation with 1.5 turn spiral antenna and contact pads from 50 GHz up to 2 THz, smaller model simulation with 1.0 turn spiral antenna from 0.5 up to 5.5 THz (shown in Fig. 3.6), smallest model simulation with 0.5 turn spiral antenna from 1 up to 12 THz. Triangles are added to the outer ends of the spiral models at higher frequencies where the outer parts of the antenna are excluded from simulation. The triangles ensure a smooth transition between metalization and pure semiconductor at the artificially introduced boundary not present in the real antenna. The low frequency model includes all metalization layers from the lithographic mask used for fabrication. The metal layer is modeled as a perfect electrical conductor, giving no

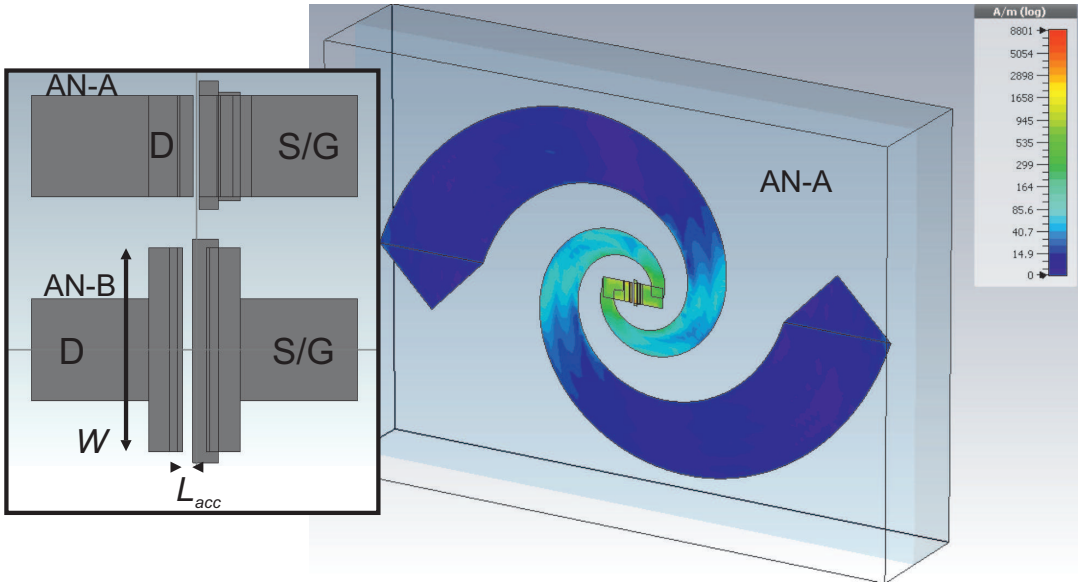

Fig. 3.6: *Model for the simulation of the radiation impedance Z_A from 0.5 up to 5.5 THz with an one turn spiral (cut) for the 15 µm wide design AN-A. The color indicates the simulated RMS value of the surface current at 3.3 THz, being suppressed by 2 orders of magnitude in the outermost half-turn of the spiral antenna. The inset on the left compares the designs of the 15 µm wide device AN-A with the 30 µm wide device AN-B.*

ohmic losses in the antenna (input) impedance.

Fig. 3.7 shows the simulated radiation impedance Z_A for the two different antenna designs. Between the different simulation models there are minor offsets in the simulated radiation impedance for the very same frequency. The simulated radiation impedance is therefore combined with a linear transition from the low frequency model to the mid frequency model from 1.6 to 2.0 THz and with a linear transition from the low frequency model to the mid frequency model from 4.9 to 5.5 THz.

The antenna-coupled FETs with strong gate-source coupling have an AC shunt between source and gate. Therefore, there is only one single antenna gap with the length L_{acc} between gate and drain contact. For the calculation of the coupling efficiency η_{El}, it is necessary to simulate the capacitor C_{GD} between source and gate. CST simulations yield $C_{GD} = 3.09$ fF for a 15 µm wide device (AN-A) with an antenna gap of $L_{acc} = 0.8$ µm, and $C_{GD} = 3.66$ fF for a 30 µm wide device (AN-B) with an antenna gap of $L_{acc} = 1.5$ µm in the center.

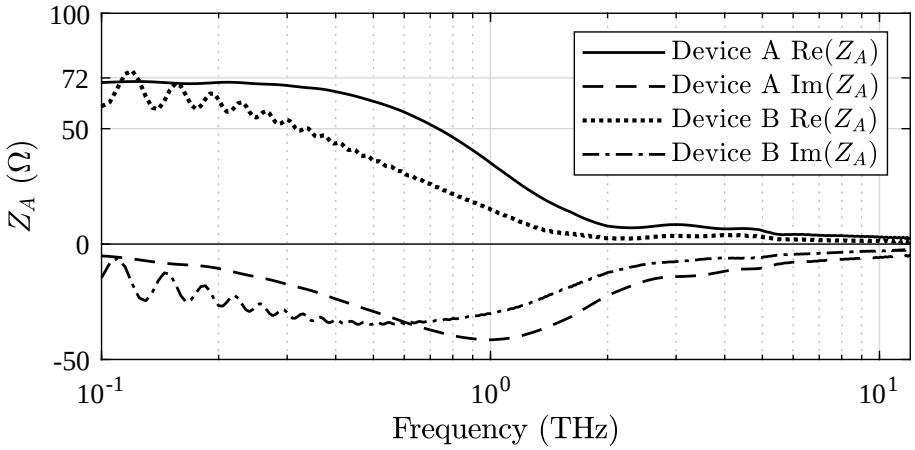

Fig. 3.7: *Simulated radiation impedance Z_A from 0.1 up to 12 THz for a 1.5 turn spiral antenna with the 15 μm wide device AN-A with an antenna gap of $L_{acc} = 0.8\,\mu m$ and the 30 μm wide device AN-B with with an antenna gap of $L_{acc} = 1.5\,\mu m$ in the center. At low frequencies, Re(Z_A) is close to the theoretically expected value of $R_A = 72\,\Omega$.*

Large-area designs

Large-area designs circumvent narrowband antenna resonances and limitations through the finite size of antennas and semiconductor devices. They show a smooth antenna behavior over an extreme frequency range. This enables the study of THz induced currents in FETs in the frequency range from 0.1 up to 30 THz. LA-FETs can further be used as detectors for the exceptional frequency range with large linearity range and simultaneous detection of 800 nm pulses.

Fig. 3.8 shows the scheme of a LA-FET. The radiation resistance of a large-area emitter can be calculated from single Herztian dipoles. The calculated radiation resistance can also be used for the inverse problem, the detection with a large-area detector. The resulting radiation resistance for a LA-FET is [1, Eq. 90]

$$R_A^{LA} = \frac{Z}{6\pi} \frac{(l_0 k)^2}{1 + (0.82\, k\rho_0)^2}, \tag{3.47}$$

where $k = 2\pi f n_{eff}/c$ is the effective wave vector of the THz wave, $Z = Z_0/n_{eff}$ the effective impedance, l_0 the length of the Hertzian dipoles, and ρ_0 the beam waist.

Fig. 3.9a) shows the radiation resistance of Eq. 3.47 for 0.3 and 2.0 THz for different beam waists. The radiation resistance increases for illumination from the substrate side due to the smaller beam waist in substrate. For a Herztian dipole length of $l_0 = 7.5\,\mu$m (typical source-drain distance including contacts) in an array with a total size of $0.3 \times 0.3\,\mathrm{mm}^2$, a radiation resistance of 6 mΩ at 0.3 THz is expected. Fig. 3.9b) shows the radiation resistance of Eq. 3.47 vs frequency. For a diffraction-limited beam waist the R_A increases quadratically with frequency, whereas for a fixed beam waist, the radiation resistance saturates with increasing frequency.

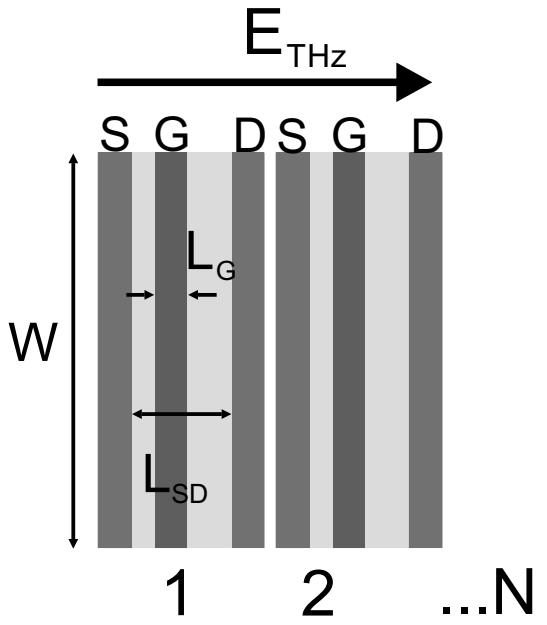

Fig. 3.8: *Schematic of the LA-FET structure. The THz radiation couples directly to the channel of the transistor channel or through ohmic (S and D) and Schottky (G) contacts.*

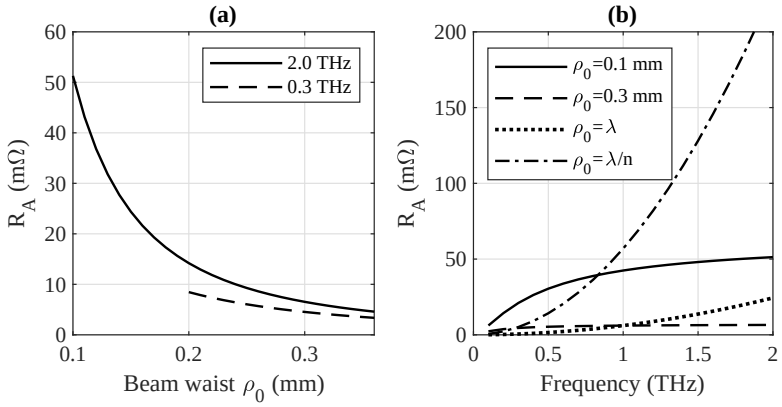

Fig. 3.9: *a) Radiation resistance R_A vs beam waist ρ_0 for 0.3 and 2.0 THz. b) R_A vs frequency for a beam waist ρ_0 of 0.1 mm, 0.3 mm, λ, λ/n. Diffraction-limited beam waists scale with the wavelength λ. In a substrate the beam waist shortens by the refractive index n. Here $n = 3.6$ for GaAs is used.*

3.6. Semiconductor structure

The semiconductor material is a key component in the FET. For simplification of the fabrication, a long effective rectification length is preferred, that can be obtained with a material featuring a high mobility (cf. Eq. 3.20). As the rectified current scales with the gate-channel capacitance (cf. Eq. 3.30), a high gate-channel capacitance is needed for a high rectified current. For a high coupling efficiency (cf. Eq. 3.40), a low access resistance Z_{acc} is needed, that can be obtained with a small sheet resistance and thus a high mobility and high charge carrier density.

Based on these considerations HEMTs and MOSFETs are compared. (Al)GaAs-based HEMTs have a mobility in the range of 4000 up to 8000 $\mathrm{cm}^2/\mathrm{Vs}$ at room temperature, Si-based MOSFETs have a mobility in the range of 100 up to 400 $\mathrm{cm}^2/\mathrm{Vs}$ at room temperature [76; 77]. The charge carrier mobility in channels of Si-based MOSFETs is lower than that of intrinsic silicon with 1450 $\mathrm{cm}^2/\mathrm{Vs}$ for electrons at room temperature [78]. A MOSFET channel is doped and has therefore impurities, that reduce the mobility. In GaAs-based HEMTs the 2DEG channel forms at the interface between an intrinsic GaAs layer and a barrier with a large band gap such as $\mathrm{Al}_x\mathrm{Ga}_{1-x}\mathrm{As}$, where the conduction band (CB) dips underneath the Fermi level E_F. A simulated band structure of a (Al)GaAs-based HEMT is shown in Fig. 3.10. The important feature of this structure is the remote δ-doping in the barrier. This allows to omit doping of the channel. The mobility of the undoped GaAs channel reaches therefore values of 4000 up to 8000 $\mathrm{cm}^2/\mathrm{Vs}$ at room temperature. (Al)GaAs-based semiconductors directly form a Schottky contact with a sufficient barrier height; therefore the fabrication is facilitated, as an additional thin insulator layer with a high dielectric constant is not needed. A thin $\mathrm{Al}_x\mathrm{Ga}_{a-x}\mathrm{As}$ barrier between the Schottky contact and the 2DEG channel leads to a high gate-channel capacitance c. One disadvantage of a remotely doped thin barrier is the lower achievable charge carrier density as compared to directly doped channels. The remotely doped samples feature a charge carrier density $n^{(2D)} < 10^{12}\,\mathrm{cm}^{-2}$.

In summary, (Al)GaAs-based HEMT semiconductors are expected to allow similar responsivity and sensitivity in comparison with Si-based MOSFETs with facilitated fabrication. More established foundry processes of Si-based technology allow a fabrication with much more precise design parameters. However, the use of foundry processes without industry-scale funding usually requires months for a finished device and therefore impedes rapid-prototyping. For this thesis, (Al)GaAs-based HEMT semiconductors with superior material parameters are chosen, allowing inexpensive UV-contact lithography. All devices used in this thesis are produced in the university clean room.

The modulation-doped (Al)GaAs semiconductors used for fabrication of FET devices in this thesis were grown by molecular beam epitaxy (MBE) at University of California, Santa Barbara by Hong Lu in the group of Arthur C. Gossard. Fig. 3.10 shows the band structure of a semiconductor underneath the gate as used in this thesis. The band structure is simulated with the software "1Dpoisson" from G. Snider at University of Notre Dame, USA. There are two boundary conditions for the band

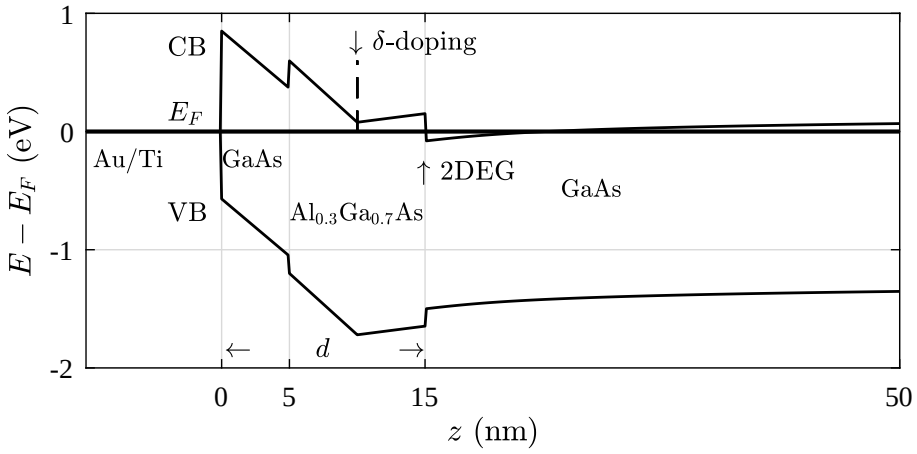

Fig. 3.10: *Simulated band structure of a semiconductor underneath the Schottky contact. The 2DEG forms at the interface between the $Al_{0.3}Ga_{0.7}As$ barrier and the intrinsic GaAs layer, where the conduction band (CB) dips under the Fermi level E_F. The barrier thickness d between the Schottky contact and the 2DEG of this structure is only* 15 *nm.*

structure: One is the surface with the Schottky barrier to the gate contact on top, the other is the semi-insulating GaAs substrate. Starting from the semiconductor surface in Fig. 3.10, there is a 5 nm GaAs cap layer, to prevent oxidation, followed by a 10 nm $Al_{0.3}Ga_{0.7}As$ layer with a Si remote doping. The 1.42 eV band gap in GaAs is increased to 1.80 eV by adding 30% Al to the layer. The barrier is followed by a 1 μm thick GaAs layer for the 2DEG and another thicker $Al_{0.3}Ga_{0.7}As$/GaAs buffer layer between the channel and the substrate. The semiconductor structure is completed by the semi-insulating substrate.

The material parameters of the fabricated devices are listed along with the geometrical dimensions of the FETs in Table 5.1.

4. Free electron laser pulse shape modeling

Within this thesis, LA-FET and A-FET devices are characterized with FEL pulses. FELs offer an extreme tunability of the frequency of operation and a high intensity. FELBE at the Helmholtz-Zentrum Dresden-Rossendorf offers a tunability from 1.3 up to 75 THz with its two undulators. For the experiments it is operated in a mode continuously delivering pulses at a constant repetition rate; the generated pulses are detected with FET detectors and compared to the measured intensity spectra. The (maximum) linewidth $\Delta\lambda/\lambda$ depends on the number of periods in the undulator and is in the range of $\approx 1\%$ for FELBE [79]. The natural linewidth arises from the finite gain width of the undulator. According to Madey's theorem, the stimulated emission is proportional to the negative derivative of the spontaneous emission with respect to the argument [80, p.35]. Fig. 4.1 shows the theoretical linewidth from spontaneous and stimulated emission for a $N_U = 38$ period undulator. The U100 undulator at FELBE radiating between 1.3 and 16 THz has 38 periods and is used for the THz frequency range in this thesis. The U27 undulator radiating between 14 and 75 THz is used for the MIR range and has $2 \cdot 34$ periods. The spontaneous emission calculates to $\mathrm{sinc}^2(\pi N_U \Delta f/f_0)$, due to the finite length of the undulator from the electron frame [79; 80]. For a positive net transfer of energy from the electron beam to the electromagnetic field, the electron energy has to be higher compared to the resonant case defined by Eq. 2.1.

The measurement of the THz peak power and pulse shape is essential for experiments on non-linear effects using ultra-short pulses. For pump-probe experiments, FELs can also be synchronized with NIR lasers. Jitter and drift of the FEL impede experiments that require the measurement of peak power, pulse shape and temporal delay to a NIR laser on the single pulse level. Therefore a FET detector being able to measure the pulse shape and pulse width in real-time is highly desirable.

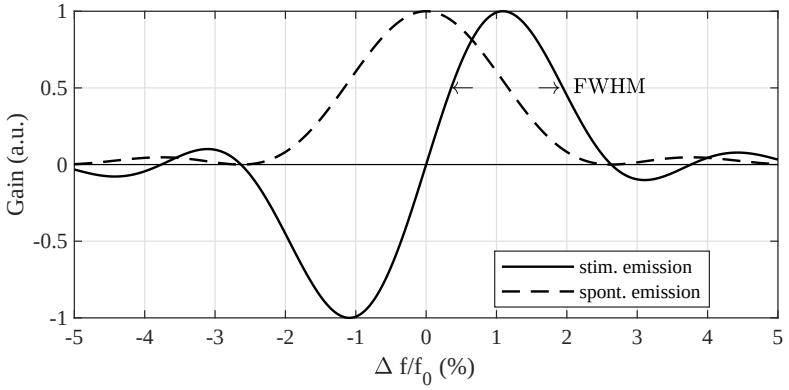

Fig. 4.1: *Spontaneous (dashed line) and stimulated emission (solid line) for a 38 period undulator. The resulting natural linewidth (FWHM) from the stimulated emission is 1.6 %.*

4.1. Conventional pulse modeling

The pulse width at a given frequency can be altered by changing the cavity length. In this thesis FETs are used to measure the resulting pulse shape in comparison with the intensity spectra of the FEL pulses. In this chapter, a novel convolution ansatz for the description of FEL pulses from a detuned cavity, with an exponential rising edge is compared to the state-of-the-art piecewise model [30]. For both models, the power spectrum of the pulses is calculated through Fourier transform of the respective field quantities.

The output power of an FEL depends on the cavity length L. Due to the dynamics of the FEL lasing process, the required cavity detuning is *negative*, i.e. the cavity length needs to be shortened. There is no stable lasing at exactly zero or positive cavity detuning ($\Delta L \geq 0$) [79; 81]. At the optimum working point, the pulse shape is Gaussian and the FEL delivers maximum power. The maximum output power is reached for a slightly negative cavity detuning ΔL of around $-0.2\,\lambda$ [82].

FEL pulses from a strongly negative detuned cavity $\Delta L \ll 0$ feature an exponential rising edge and a Gaussian falling edge [25; 30; 31; 83]. In every round trip of the pulse in a cavity shortened by $|\Delta L|$, the leading edge of the pulse is arriving $\Delta t = 2|\Delta L|/c$ before the electron bunch and is not achieving gain in the undulator. As a result, the leading edge of the pulse is attenuated exponentially with the loss factor $\alpha < 0$ of the cavity. The resulting pulse shape of the rising edge of the pulse is $\propto e^{c\alpha t/2\Delta L} = e^{t/\tau}$ with $\tau = 2\Delta L/(c\alpha)$.

The state-of-the-art piecewise ansatz for the resulting intensity pulse envelope is [31]

$$\begin{aligned} p_{pw}(t) &= p_0 \cdot \begin{cases} \exp(+t/\tau) & \text{for } t < 0 \\ \exp(-t^2/[2\sigma^2]) & \text{for } t \geq 0 \end{cases} \\ &= p_0 \cdot \left[X_\tau(t) + H(t) \cdot G_\sigma(t)\right], \end{aligned} \tag{4.1}$$

where the exponential rise is given by $X_\tau(t) = H(-t)\exp(+t/\tau)$, with the Heaviside step function $H(t)$, and the Gaussian part by $G_\sigma = \exp(\frac{-t^2}{2\sigma^2})$. The piecewise ansatz $p_{pw}(t)$ is discontinuously differentiable at the peak $t = 0$ and shows strong deviations from the measured pulse shape at the peak [31]. The piecewise ansatz further cannot describe a rising edge dominated by a Gaussian, as it is expected for the optimum working point $\Delta L \to 0$, as well as it cannot describe a rising edge with a combination of Gaussian and exponential behavior. It is therefore only suitable for large negative cavity detunings ($\Delta L \ll 0$).

Fig. 4.2 shows an exemplary pulse shape of the piecewise model as dashed line.

From the pulse intensity $p_{pw}(t)$, the field ($\propto \sqrt{p_{pw}(t)}\exp(j\omega_0 t)$) calculates to

$$E_{pw}(t) = E_{pw0} \cdot e^{j\omega_0 t} \cdot \left[X_{2\tau}(t) + H(t) \cdot G_{\sqrt{2}\sigma}(t)\right], \tag{4.2}$$

with the angular oscillation frequency $\omega_0 = 2\pi f_0$. The oscillation frequency f_0 can be measured e.g. in an auto-correlation setup using direct detectors such as a Schottky

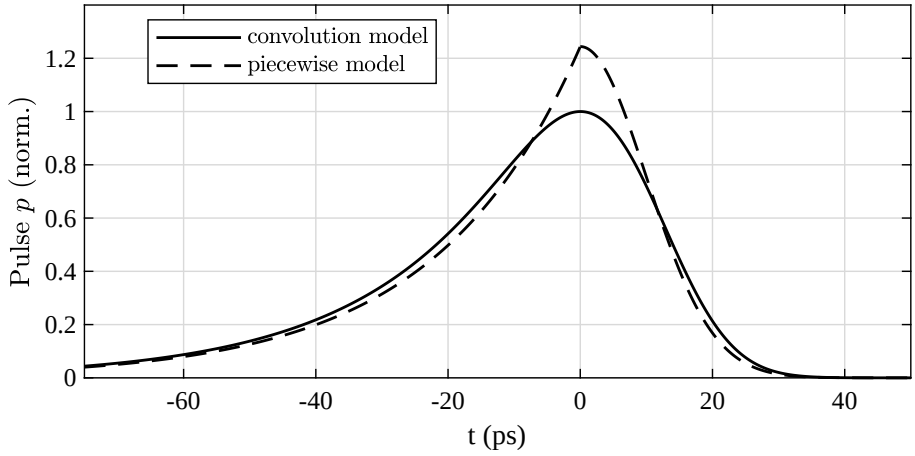

Fig. 4.2: *FEL pulse shape of a detuned cavity modeled with the state-of-the-art piecewise model (dashed line) and the novel convolution ansatz (solid line). The exponential and Gaussian widths are* $\tau = 21\,\mathrm{ps}$ *and* $\sigma = 8\,\mathrm{ps}$ *, respectively. For closer resemblance of the piecewise model to the convolution model a Gaussian width of* $\sigma = 10\,\mathrm{ps}$ *is used for the plot of the piecewise function.*

diode or a FET [26], or also with a grating spectrometer. The intensity spectrum $\hat{p}_{pw}(f)$ can be obtained as $\hat{p}_{pw}(f) \propto |\hat{E}_{pw}(f)|^2$ with the Fourier transform of $E_{pw}(t)$

$$\hat{p}_{pw}(f) = \hat{p_0}\left|\frac{\tau/2 - j\tau^2 2\pi f_{IF}}{1/4 + \tau^2 4\pi^2 f_{IF}^2} + \sigma\sqrt{\pi}e^{-\sigma^2 4\pi^2 f_{IF}^2} + 2j\sigma\,\mathrm{D}(\sigma 2\pi f_{IF})\right|^2, \tag{4.3}$$

where $\mathrm{D}(x) = e^{-x^2}\int_0^x e^{t^2}\,\mathrm{d}t$ is defined as the Dawson function and $f_{IF} = f - f_0$ the base band frequency.

4.2. Convolution pulse modeling

The unphysical non-differentiable peak at $t = 0$ of $p_{pw}(t)$ of the state-of-the-art ansatz can be circumvented by a refined model developed in this thesis. It assumes a convolution of a rising exponential edge with a Gaussian. In this section, this ansatz is evaluated, and in Chapter 8 compared with experimental results. The refined ansatz allows the description of pulses that feature close to zero cavity detuning, where the rising edge is dominated by a Gaussian ($\sigma \gg \tau$), as well as rising edges with both Gaussian and exponential contribution ($\sigma \approx \tau$). Further, this ansatz yields better agreement around the peak position. Finally, it allows to extend the ansatz in order to include the temporal resolution limitations in an easy way as discussed in the following section. The intensity of the pulse is modeled as

$$\begin{aligned} p(t) &= p_0\big(\exp(-t^2/[2\sigma^2]) * [H(-t)\exp(t/\tau)]\big) \\ &= p_0(G_\sigma(t) * X_\tau(t)), \end{aligned} \tag{4.4}$$

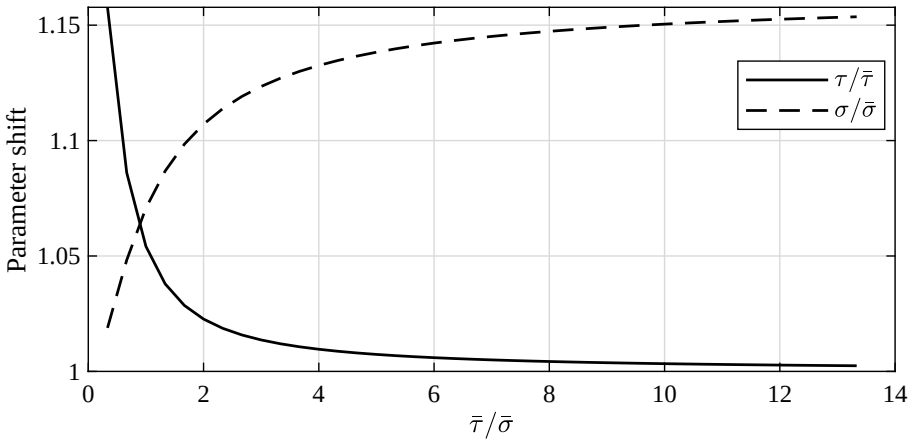

Fig. 4.3: *Parameter shift for the Gaussian and exponential width for the approximation in Eq. 4.5.* $G_\sigma(t) * X_\tau(t)$ *is fitted to* $(G_{\sqrt{2}\bar{\sigma}}(t) * X_{2\bar{\tau}}(t))^2$ *for* $\bar{\sigma} = 3\,\mathrm{ps}$ *and a range of* $\bar{\tau}$ *from* 1 *up to 40 ps.*

where "$*$" is the convolution operator. Fig. 4.2 compares the refined model with the piecewise ansatz. For strong exponential broadening $\tau \gg \sigma$ the rising edge of $p(t)$ is dominated by an exponential behavior $\propto \exp(+t/\tau)$ in agreement with the state-of-the-art model, whereas for the limit of no exponential broadening, the pulse features a Gaussian shape $\lim_{\tau\to 0} p(t) = G_\sigma(t)$. For a spectral analysis of this ansatz, a Fourier transform of the respective field quantity $E(t)$ is performed. The convolution operator and the square root do note commute, therefore there is no simple analytical expression for the Fourier transform of $\sqrt{p(t)}$. For simplification of the transformation, the pulse $p(t)$ can be approximated very well by

$$p(t) = p_0 \left(G_\sigma(t) * X_\tau(t)\right) \approx p_0 \left(G_{\sqrt{2}\bar{\sigma}}(t) * X_{2\bar{\tau}}(t)\right)^2, \tag{4.5}$$

with $\sigma/\bar{\sigma} = 1.0$ for an (almost) Gaussian pulse with $\tau \ll \sigma$, while $\sigma/\bar{\sigma} \approx 1.2$ and $\tau/\bar{\tau} = 1.0$ for $\tau \gg \sigma$. Fig. 4.3 shows the numerically calculated parameter shift $\sigma/\bar{\sigma}$ and $\tau/\bar{\tau}$ for the approximation in Eq. 4.5.

The best approximation for the generated pulses at FELBE is obtained with parameters in the range of $\sigma/\bar{\sigma} \approx 1.1$ and $\tau/\bar{\tau} \approx 1.03$. In Fig. 4.4a) the intensity pulse $G_\sigma(t) * X_\tau(t)$ (dashed line) is compared with the approximation $(G_{\sqrt{2}\bar{\sigma}}(t) * X_{2\bar{\tau}}(t))^2$ (solid line) for pulses from FELBE for two different pulse shapes. Fig. 4.4b) shows the deviation of the two functions in time domain, its maximum is in the range of 0.5%, being smaller than the experimental noise. The envelope of the electrical field can therefore be described very well by the convolution of a Gaussian with a exponential rise with modified temporal widths. The electrical field is obtained as

$$E(t) = E_0 \left(G_{\sqrt{2}\bar{\sigma}}(t) * X_{2\bar{\tau}}(t)\right) \exp(2\pi j f_0 t). \tag{4.6}$$

Through Fourier transformation, the resulting spectrum of the electrical field is

$$\hat{E}(f) = \hat{E}_0 G_{(2\pi\sqrt{2}\bar{\sigma})^{-1}}(f_{IF}) \cdot \frac{2\bar{\tau}}{1 - 4\pi j \bar{\tau} f_{IF}}. \tag{4.7}$$

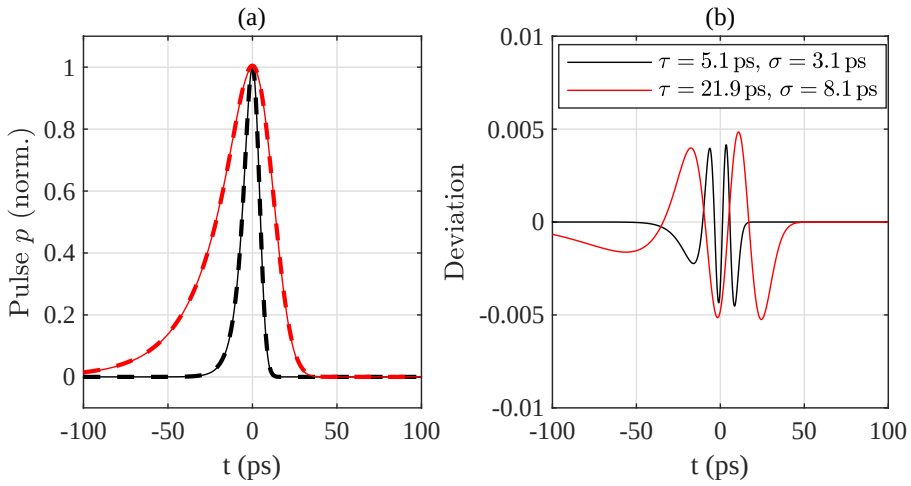

Fig. 4.4: *a) Comparison of the approximation in Eq. 4.5 for $G_\sigma * X_\tau$ (dashed line) and $(G_{\sqrt{2}\bar{\sigma}} * X_{2\bar{\tau}})^2$ (solid line) for two different FEL pulse shapes generated at FELBE. The two functions show excellent agreement. b) Absolute deviation of the functions from a) for each of the two FEL pulse widths shown in a). Adapted from [30] ©IEEE 2019.*

The corresponding power spectrum of $p(t)$ can be calculated to

$$\hat{p}(f) = \hat{p}_0 G_{(4\pi\bar{\sigma})^{-1}}(f_{IF}) \cdot L_{2\bar{\tau}}(f_{IF}), \tag{4.8}$$

with the Lorentz function $L_{2\bar{\tau}} = \frac{(2\bar{\tau})^2}{1+(4\pi\bar{\tau}f_{IF})^2}$ and the Gaussian $G_{(4\pi\bar{\sigma})^{-1}} = e^{-8\pi^2\bar{\sigma}^2 f_{IF}^2}$. For a comparison of the models with the measured spectra, Eq. 4.8 for the refined convolution ansatz and Eq. 4.3 for the state-of-the-art ansatz have to be fitted to the measured data. The measured data for the comparison is presented in Chapter 8 in Fig. 8.3.

As demonstrated by the theoretical considerations in this section, the developed convolution ansatz is much more general and physical than the state-of-the-art piecewise ansatz.

4.3. Circumventing temporal resolution limits

In a real detector, the measured pulse is broadened by the temporal instrument resolution. A THz pulse with the field $E(t)$ is rectified with a quadratic non-linear process, measuring the envelope $p(t) \propto |E(t)|^2$ of the pulse with read-out electronics. Due to the rectification, the pulse $p(t)$ is mapped to DC, and the frequency f is shifted by the carrier frequency f_0 to the base band frequency $f_{IF} = f - f_0$. The measured pulse $m(t)$ is a convolution of the pulse intensity, $p(t)$, with the transfer function of the rectification, $r(t)$, and the measurement electronics, respectively the IF-path, $IF(t)$[30]:

$$m(t) = p(t) * r(t) * IF(t) = p(t) * IF_{eff}(t). \tag{4.9}$$

Both $r(t)$ and $IF(t)$ consider frequency dependent losses, typically a low pass behavior. If the pulse duration of $p(t)$ is (much) shorter than the temporal width of either $r(t)$, or $IF(t)$, the temporal shape, width and also amplitude are strongly altered due to the measurement process. $r(t)$ denotes the speed limitations of the rectification process in the transistor. The gate bias alters the plasma wave velocity in the transistor channel and is therefore expected to influence the speed of the rectification [84]. For electron mobilities and gate biases comparable to those used in this study, simulations in ref. [84] yielded a time constant for $r(t)$ of $< 2\,\mathrm{ps}$. In contrast, MOSFETs show a more slowly detection speed with a time constant in the range of 12-18 ps, due to low mobilities in the $200\,\mathrm{cm}^2/\mathrm{Vs}$ range [27].

The transfer function of the rectification and the measurement electronics can be summarized to $IF_{eff}(t) = r(t) * IF(t)$. $IF_{eff}(t)$ can be measured experimentally as the impulse response function with an incident pulse $p(t)$ being temporally much shorter than $IF_{eff}(t)$. The amplitude of the measured pulses $m(t)$ depends on the temporal width of the incident pulses $p(t)$ and the low pass filtering of $IF_{eff}(t)$.

This section discusses the temporal limitations in direct detection for the initial FEL pulse shape assuming the proposed convolution model (cf. Eq. 4.4).

For the case of a Gaussian transfer function $IF_{eff}(t)$, the two Gaussian components in $p(t)$ and $IF_{eff}(t)$ can be combined. The convolution is commutative and the convolution of two Gaussian yields a Gaussian again, the Gaussian width σ_m is broadened by the Gaussian transfer function, while the exponential rise τ_m is not affected at all. Eq. 4.9 simplifies to

$$m(t) = m_0 G_{\sigma_m}(t) * X_{\tau_m}(t), \tag{4.10}$$

with the Gaussian width $\sigma_m = \sqrt{\sigma^2 + \sigma_{IF,eff}^2}$ and $\tau_m = \tau$, the index "m" refers to quantities measured in time domain with $m(t)$.

Eq. 4.10 shows that the measurement of the exponential broadening τ_m in the initial pulse $p(t)$ is possible even in case the temporal shape is below the Gaussian IF limitation ($\tau_m < \sigma_{IF,eff}$).

While mathematically a Gaussian broadening $\sigma_{IF,eff}$ does not show any influence on τ_m, the influence of noise and a finite number of data points on τ_m and σ_m is simulated numerically. In the simulation of $m(t)$, the pulses $p(t)$ are broadened by a Gaussian $IF_{eff}(t)$, random noise is added, and the pulses are finally discretized. The parameters σ_m and τ_m are then extracted from $m(t)$ by fitting, as it is also done for extraction of the temporal widths from measured data. The process is repeated 1000 times with new random noise in each repetition, comparing the extracted σ_m and τ_m with the defined σ, τ, and $\sigma_{IF,eff}$.

For a realistic comparison with the experiments performed at the FEL with the FET detectors, a Gaussian broadening of $\sigma_{IF,eff} = 14\,\mathrm{ps}$, and a Gaussian pulse width of $\sigma = 7.5\,\mathrm{ps}$ is used. The expected Gaussian width is subsequently $\sigma_m = \sqrt{\sigma_{IF,eff}^2 + \sigma^2} = 16\,\mathrm{ps}$. Fig. 4.5 shows the results of the simulated measurement accuracy. The noise level was chosen such that the same or worse SNR as in real measurements at FELBE with FET detectors is obtained.

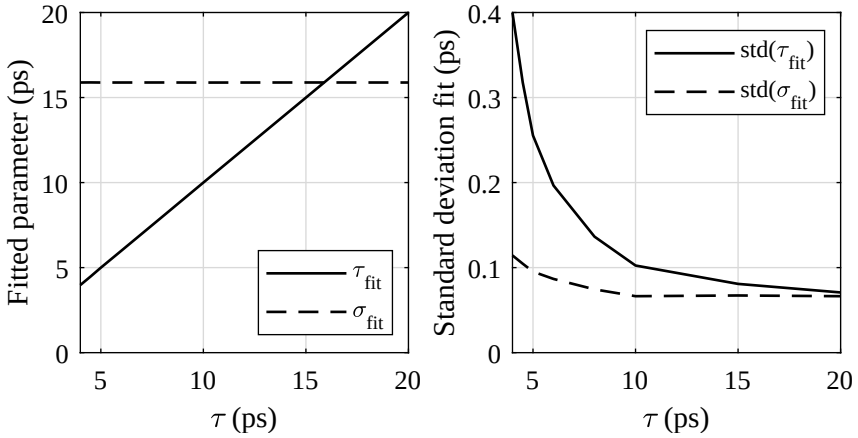

Fig. 4.5: *Simulation the measurement vs initial exponential FEL pulse width for a SNR of* 77*, an IF broadening* $\sigma_{IF,eff} = 14\,ps$ *and a Gaussian FEL pulse width of* $\sigma = 7.5\,ps$*. a) Mean of the 1000 fitted parameters for each initial pulse width. b) Deviation of the 1000 fitted pulse widths for each initial pulse width.*

For an exponential broadening of $\tau \geq 4\,\mathrm{ps}$ the standard deviation of σ_m and τ_m from the respective expected values $\sqrt{\sigma_{IF,eff}^2 + \sigma^2}$ and τ is smaller than 0.5 ps.

For an exponential broadening of $\tau < 3\,\mathrm{ps}$, numerical instabilities are observed in the fitting routine and the distribution of the fitted parameters, because of the small difference of $m(t)$ from a pure Gaussian. From this simulation, the theoretical resolution limit for the exponential rise time τ_m can be estimated to $3 - 4\,\mathrm{ps}$, with a total Gaussian part of $\sigma_m = 16\,\mathrm{ps}$ and a temporal resolution of $\sigma_{IF,eff} = 14\,\mathrm{ps}$. The simulations show that even in the presence of noise, an exponential time constant τ much below the Gaussian temporal resolution limitation $\sigma_{IF,eff}$ can be measured.

The time domain traces can be fitted using only two width parameters, a Gaussian width and an exponential width (cf. Eq. 4.10). The Gaussian width includes both the Gaussian IF limitation and the Gaussian part of the FEL pulse. For the piecewise ansatz, a three-parameter fit or a deconvolution would be required to include the Gaussian IF limitation. Both, a three-parameter fit and especially a deconvolution show larger errors of the extracted pulse width parameters and are numerically less stable. The convolution operator in Eq. 4.10 can be replaced by using an error function and an exponential function. This allows easy fitting without performing a convolution or Fourier transformation, which is a further advantage of the convolution model. It only requires a simple fit that allows to obtain the exponential width below the Gaussian IF limitation.

Amplitude suppression The measurement of fast pulses with a realistic detector and limited temporal resolution does not only broaden the measured pulse width, but also leads to a suppression in the measured peak height of the pulse (cf. Fig. 4.6a)). Peak quantities are crucial for the precise measurement of non-linear processes. For a purely Gaussian pulse $p(t) = G_\sigma(t)$ and a Gaussian filter function $IF(t) = G_{\sigma_{IF}}(t)$,

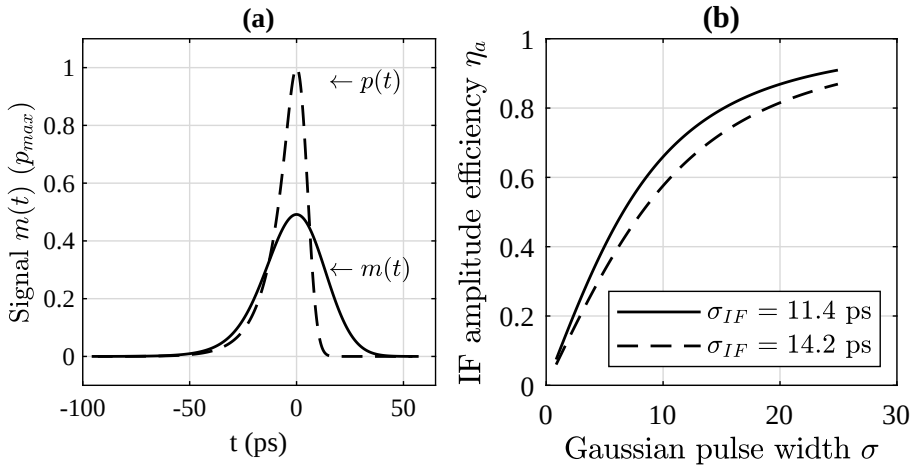

Fig. 4.6: *a) Pulse broadening and amplitude suppression due to limited IF bandwidth of $\sigma_{IF,eff} = 11.4\,ps$ for a pulse with exponential width $\tau = 9.3\,ps$ and Gaussian width $\sigma = 3.7\,ps$. b) IF amplitude efficiency η_a of the detection vs Gaussian input pulse width for two different Gaussian IF filters.*

the measured IF amplitude decreases by a factor of [85]

$$\eta_a = \frac{\sigma}{\sqrt{\sigma^2 + \sigma_{IF}^2}}. \tag{4.11}$$

Fig. 4.6b) shows the amplitude suppression for the range of pulse widths that can be generated by FELBE and the corresponding IF amplitude efficiency η_a for a fixed IF bandwidth.

Including an exponential rise, the IF amplitude efficiency η_a increases, thus the pulse amplitude is less suppressed. The amplitude suppression for those pulses is calculated numerically as shown in Fig. 4.6a).

Using the introduced convolution model of the pulse therefore enables a more precise characterization of both the FEL pulse shape as well as the peak amplitude.

5. Transistor fabrication and DC characterization

5.1. Design

With the theoretical considerations from chapter 3, different FETs are designed and fabricated within the limits of the processing technology described in this chapter. Fig. 5.1 shows an overview of the different concepts used in this thesis: LA-FET devices, A-FET devices and reference devices without Schottky contact. LA-FET detectors are designed with separate mesa, shown in Fig. 5.1a). For enhanced incoupling the design was improved in a second generation of LA-FET devices, where an AC source-gate shunt capacitance was added as shown in Fig. 5.1b). Fig. 5.1c) shows the scheme of a sample without Schottky contact. This gate-less device is no FET, it is a reference sample to quantify the THz response without a gate electrode.

The dimensions of processed, packaged and THz characterized FETs or samples without Schottky contact and respective material parameters are given in Table 5.1. Different designs with gate lengths L_G from 1 up to 4 μm and channel lengths L_{SD} from 2.4 up to 11 μm are evaluated.

The active area of the large-area devices is chosen to be able to cover the full diffraction-limited beam at FELBE. The low frequency limit of FELBE with the U100 undulator in a stable operation mode is 1.3 THz. The diffraction-limited beam waist is $\rho_0 = 1.22\lambda/\mathrm{NA} = 1.1$ mm from the air side for a numerical aperture (NA) of 0.25. For incoupling of THz power through the GaAs substrate with a refractive index of $n = 3.6$, the diffraction-limited beam waist calculates to 0.3 mm. Therefore

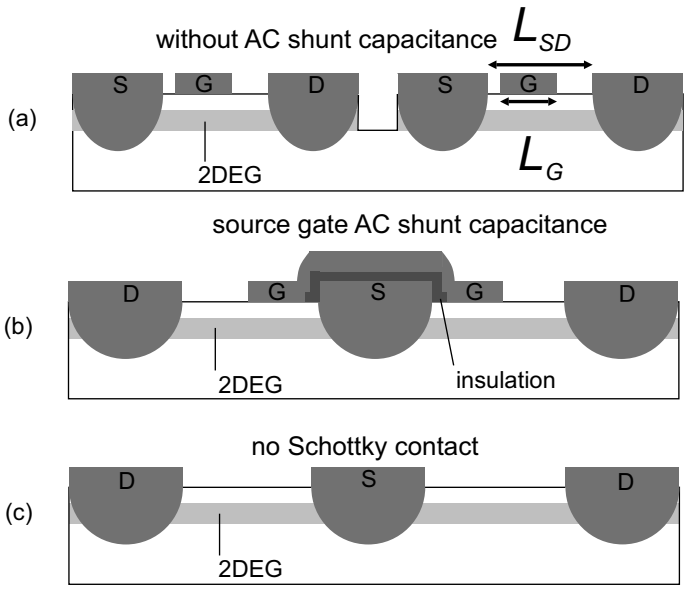

Fig. 5.1: *Overview of different concepts of samples fabricated within this thesis. a) LA-FET with separate mesa and without source-gate AC shunt capacitance. b) LA-FET or A-FET with combined mesa and with source-gate AC shunt capacitance. c) Gate-less large-area reference sample without Schottky contact.*

devices with $1 \times 1\,\mathrm{mm}^2$ active area for coupling from the air side, as well as devices with $0.3 \times 0.3\,\mathrm{mm}^2$ active area from the substrate side through a silicon lens are fabricated.

For antenna-coupled FETs, a small device in the center of the antenna is preferable, resulting in less influence on the antenna performance. The radiation impedance Z_A is simulated for a $15\,\mu$m and a $30\,\mu$m wide FET device. The narrower devices show a behavior closer to the theoretical value of $R_A = 72\,\Omega$ at high frequencies compared to the wider device (see Fig. 3.7).

At the same time, a device impedance close to the radiation impedance is preferred for a higher electrical coupling efficiency. A broadband detector operation requires a broadband antenna. A broadband self-complementary spiral antenna has a radiation resistance of $R_A = 72\,\Omega$ on the GaAs air interface (cf. Eq. 3.46). For semiconductors with a k$\Omega/\square$ sheet resistance, the device impedance usually has to be minimized. The channel resistance of an exemplary device with $1.5\,\mathrm{k}\Omega/\square$ sheet resistance, $3.8\,\mu$m channel length, and $30\,\mu$m width calculates to $190\,\Omega$. Narrowband antennas can also be designed with higher radiation resistances.

Table 5.1: *Parameters of the fabricated samples, where L_G is the gate length, L_{eff}^{∞} the effective rectification length, L_{SD} the channel length, N the number of parallel connected FETs, W the width of the FETs, μ the electron mobility, n the charge carrier density, and d the channel depth. The mobility μ and carrier density n are determined by Hall measurements of ungated structures. The sample denomination starts with information on the type, LA for a LA-FET, LAS for a LA-FET with AC source-gate shunt capacitance, AN for an A-FET, and NG for a sample without gate contact.*

sample	type Fig. 5.1	L_G (μm)	L_{eff}^{∞} (μm)	L_{SD} (μm)	N	W (μm)	μ ($\frac{\mathrm{cm}^2}{\mathrm{Vs}}$)	n ($\frac{10^{11}}{\mathrm{cm}^2}$)	d (nm)
LA-A	a)	1	0.1	3.5	38	300	4323	1.8	15
LA-B	a)	4	0.3	11	16	300	6022	5.3	25
LA-C	a)	1	0.3	11	16	300	6022	5.3	25
LA-D	a)	2	0.3	7	19	300	6022	5.3	25
LA-E	a)	3	0.1	12	48	1000	4323	1.8	15
LAS-A	b)	1	0.4	4.5	44	300	5750	7.1	30
LAS-B	b)	1.5	0.4	4.5	44	300	5750	7.1	30
LAS-C	b)	3	0.4	8	28	300	5750	7.1	30
LAS-D	b)	1.5	0.4	4.5	138	1000	5750	7.1	30
LAS-E	b)	2	0.3	6	116	1000	6022	5.3	25
AN-A	b)	1.2	0.3	2.4	1	15	5990	4.6	30
AN-B	b)	1.2	0.4	3.8	1	30	5750	7.1	30
NG-A	c)			6	36	300	5750	7.1	30
NG-B	c)			8	90	1000	5750	7.1	30
NG-C	c)			11	16	300	6022	5.3	25

5.2. Fabrication

This section provides an overview of the different processing steps for fabrication of a FET. The following processing steps are illustrated in Fig. 5.2. For the structuring of the semiconductor in each processing step, the semiconductor sample is first spin-coated with resist. The sample with the resist is then illuminated selectively with UV light by using a structured chrome glass mask (see Fig. 5.2a)). After selective illumination in the mask aligner, the resist is dipped into a developer solution (MIF 726). Depending on the type of resist, either the illuminated areas or the non-illuminated areas of the resist are dissolved by the developer. The wavelength of the used UV light limits the resolution for contact lithography to about $1\,\mu$m. Smaller structure widths in UV contact lithography require the combination of at least two processing steps. A controlled distance between two structures can be created with a precision below $0.5\,\mu$m, limited by the optical alignment precision of the mask aligner.

In this thesis, gaps between metal contacts with a controlled minimum width of $0.7 \pm 0.1\,\mu$m between two different layers are fabricated. The roughness of the edges of the metalization with UV contact lithography in the range of $0.1\,\mu$m ultimately limits the minimum gap width.

A metalization or insulation can be structured by evaporation on top of a structured resist. In the areas, where the metalization is on top of the resist, it is lifted off by dipping the sample in a solvent for the resist (Fig. 5.2b)). A successful lift-off requires a resist being thicker than the metal and an undercut in the resist. The undercut ensures that the resist layer is not completely covered by the metalization or insulation and allows the solvent to remove the complete resist layer.

The processing steps for the fabrication of a (Al)GaAs-based FET with a 2DEG channel are as follows:

- Fig. 5.2b): Ge/Au/Ni/Au metalization of source and drain contacts.
- Fig. 5.2c): Temperature-assisted annealing of ohmic source and drain contacts. The eutectic Ge/Au alloy diffuses into the semiconductor, creating ohmic contacts to the 2DEG channel.
- Fig. 5.2d): Mesa structure created by dry-etching of the semiconductor. This step removes the 2DEG channels in areas of the antenna or device, where electrical conductivity is unintended.
- Fig. 5.2e): Growth of the insulation layer. For devices with a strong gate-source coupling or crossing DC interconnects a 100 nm SiN layer is grown by a CVD process.
- Fig. 5.2f): Evaporation of Ti/Au Schottky contacts. Only after the temperature assisted annealing of the ohmic contacts and the growth of the insulation layer, the Schottky contacts can be evaporated. An antenna or electrical connections can also be created in this step.

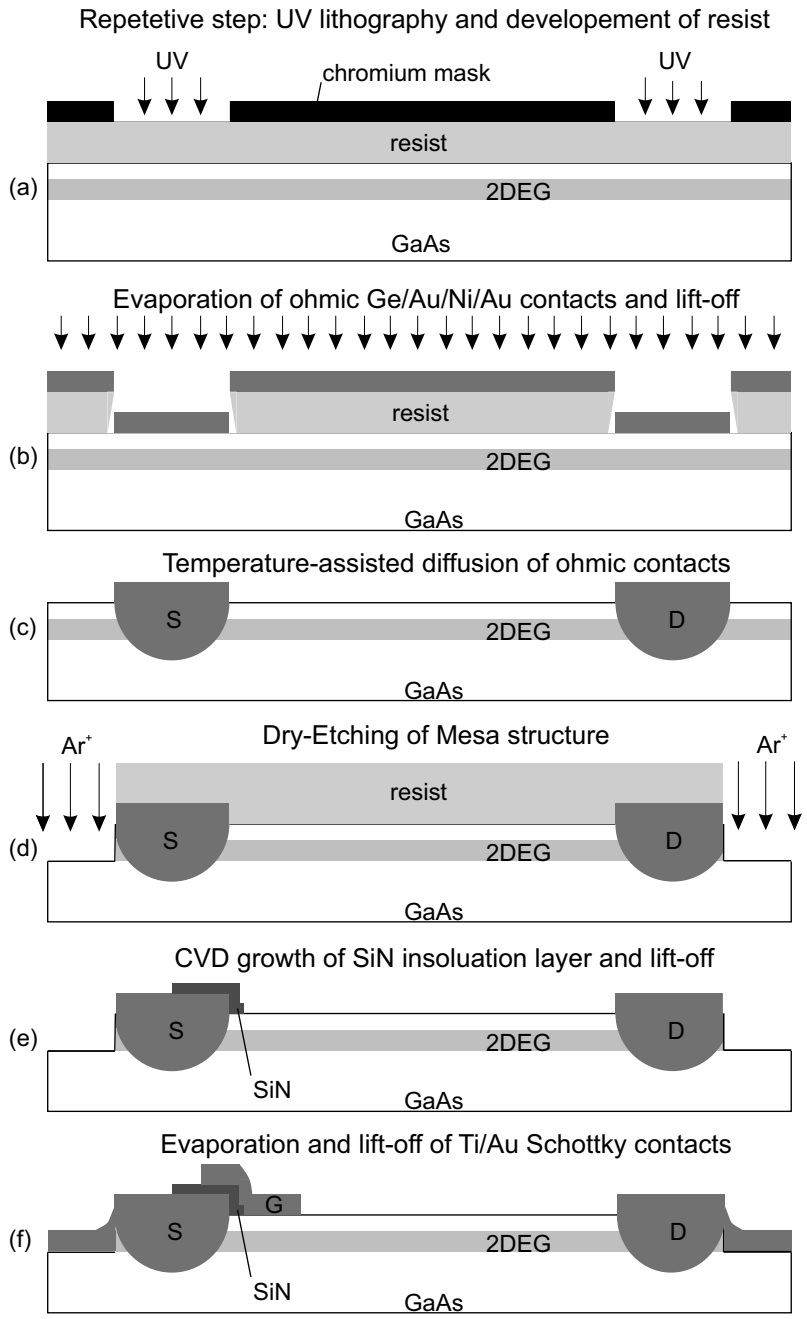

Fig. 5.2: *Processing steps of a (Al)GaAs-based FET device for THz detection. Adapted from [9].*

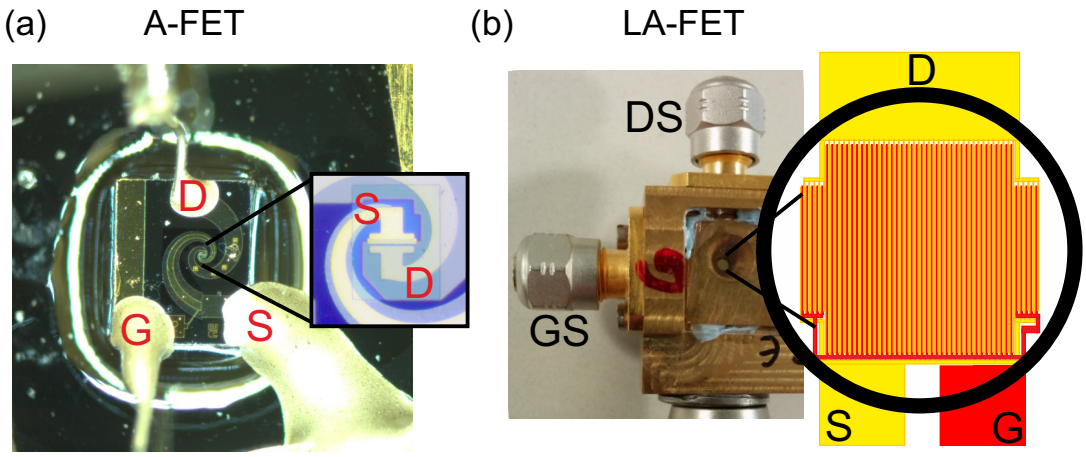

Fig. 5.3: *FET devices packaged in compact metal cases for noise reduction and simple alignment in experiments. The source (S) contact is connected to the metal case; the gate (G), and drain (D) contacts are connected via respective pads and bond wires to the coaxial SMA connectors, one for the U_{DS} read-out, the other one for the U_{GS} bias. a) Antenna-coupled FET (device AN-B) mounted on top of a silicon lens. Zoom-in: microscope image of* 30 *µm wide A-FET AN-B. b) Metal case with packaged LA-FET device LA-E for incoupling through air with metal aperture in front. zoom-in: design of device LA-E and indication of the* 1.5 *mm metal aperture. Adapted from [30]* ©*IEEE 2019.*

Special precautions should be taken because a single unintended short between source, drain or gate wiring cannot be separated and (DC) shorts the whole LA-FET. Therefore, the processing of LA-FET devices with an exceptionally large active area of $1 \times 1\,\mathrm{mm}^2$ or $0.3 \times 0.3\,\mathrm{mm}^2$ requires extremely clean working conditions, a careful control of imperfections in the resist, metalization and insulation layers during processing. For devices with a strong gate-source coupling, a large gate-source capacitance is required. The capacitance is fabricated by placing the gate metalization partly on top of the source metalization only with a thin SiN insulation layer in between. This design is challenging for fabrication, as the area of the overlapping contacts should be large for strong coupling, but the probability of a DC short increases also with the area of the overlap.

After and during the processing, the DC characteristics of the finished devices are measured with needle probes. Finally, the wafers are cleaved and selected devices packaged. A-FETs and LA-FETs using THz incoupling through the substrate are mounted on top of a hyper-hemispherical silicon lens for an increased numerical aperture (NA). Fig. 5.3a) shows an antenna-coupled FET mounted on top of a silicon lens. Gate, source, and drain are connected with conductive epoxy to coaxial SMA connectors through respective on-chip pads and interconnects. LA-FETs with an $1 \times 1\,\mathrm{mm}^2$ active area, designed for THz incoupling from the air side, are also mounted directly in a metal package. For most measurements, a metal aperture is placed in front of the active area for the air-side incoupling, as shown in Fig. 5.3b).

The metal cone acts as an aperture ensuring that THz radiation is not coupled to the bond wires. The 1.5 mm aperture is especially important while aligning the FET detector in a THz measurement setup, ensuring that the THz radiation is focused only on the active area [86]. $0.3 \times 0.3\,\mathrm{mm}^2$ LA-FET devices mounted on a silicon lens can be used for incoupling from both the substrate through the silicon lens, and from the air with a 0.5 mm aperture [87].

The first generation of devices LA-A, LA-B, LA-C, LA-D, and LA-E without strong source-gate coupling were fabricated prior to this thesis by Sascha Preu. The devices LA-B, LA-C, and LA-D from the first generation of devices, are bonded directly to custom coaxial cables. The coaxial cables feature a 3 dB corner frequency of only about 8 GHz and strong standing waves due to imperfections of the self-manufactured SMA connector [28]. An additional pre-amplifier further limits the IF bandwidth.

Within this thesis, the packaging is improved with a CNC-drilled brass package and the source-drain SMA connector (Radiall R125.512). For all improved devices source and drain pads of the FETs are connected by short wires with a length of about 1 mm to the SMA connector as shown in Fig. 5.3a). The IF path is therefore greatly improved for the second generation of detectors in combination with commercial high-quality cables with a 3 dB corner frequency above 20 GHz.

The LA-FETs and A-FETs fabricated within this thesis with improved designs (source-gate shunt capacitance) also provide a higher responsivity not requiring additional pre-amplification before the oscilloscope.

5.3. DC Characterization

The DC characterization during and after fabrication allows to control the annealing of the ohmic contacts and identify defective devices. Fig. 5.4a) shows the DC channel current I_{DS} vs gate bias U_{GS} of large-area device LA-E. Fig. 5.4b) compares the source-drain resistance R_{DS} of the LA-FET devices LA-E and LAS-A with the A-FET device AN-B. The devices LA-E and AN-B feature a threshold bias of $U_{th} \approx -0.4\,\mathrm{V}$ and $U_{th} \approx -0.5\,\mathrm{V}$, respectively. For a strongly negative gate bias the DC resistance R_{DS} of device LA-E shows a deviation from an exponential increase. This can be attributed to a small part of the 48 mm wide FET, where the channel does not fully close with gate bias. At zero gate bias, the DC resistance R_{DS} of the LA-FETs is between 10 and 20 Ω, dominated by the serial resistance from the DC wiring from to the source and drain contact pads on the semiconductor. The expected resistance from material parameters obtained by Hall measurements is $R_{DS} = 2\,\Omega$ ($R_{DS} = 0.05\,\Omega$) for device LA-E (LAS-A).

A FET with a transconductance peaking close to $U_{GS} = 0\,\mathrm{V}$ is desirable for zero-bias operation. Fig. 5.5 shows the transconductance of device AN-A, peaking at $0.05 \pm 0.05\,\mathrm{V}$. This qualifies device AN-A for zero-bias operation. Zero-bias devices do not require an external bias source, potentially adding more noise and allow to facilitate fabrication of future devices requiring only a connection to source and drain.

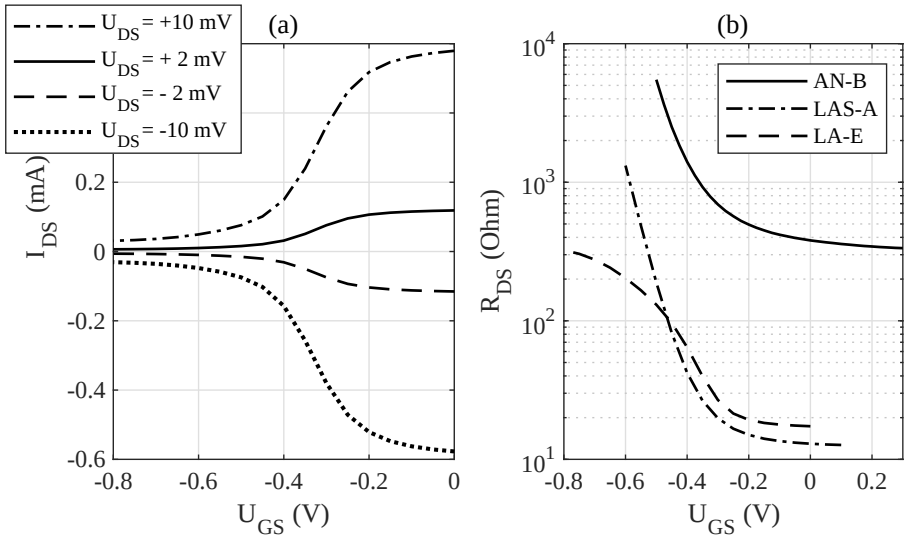

Fig. 5.4: *a) I_{DS} vs U_{GS} for device LA-E with a threshold bias of $U_{th} \approx -0.4$ V. b) Exponentially increasing channel resistance R_{DS} for decreasing gate bias U_{GS}. The 30 μm wide antenna-coupled device AN-B ($U_{th} \approx -0.5$ V) shows larger resistance compared with the LA-FET devices LAS-A and LA-E of 13 mm and 48 mm for all of the mesa connected in parallel, respectively. LA-E shows a deviation from the exponential behavior for strongly negative U_{GS} voltage.*

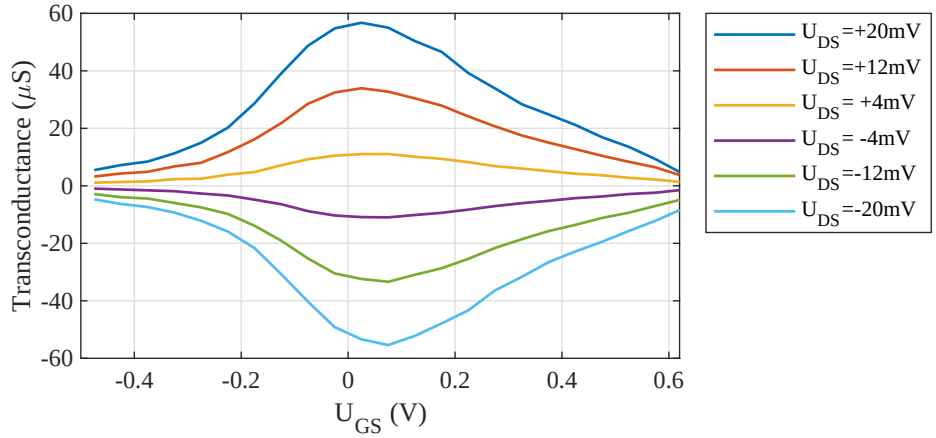

Fig. 5.5: *Transconductance of device AN-A. The transconductance peaks close to $U_{GS} = 0$ V. Adapted from [29] ©IEEE 2018.*

6. Terahertz characteristics

This chapter first introduces the various experimental setups used for the CW THz characterization on the low frequency end of the THz band and the pulsed THz characterization from 1.3 up to 30 THz. The experimental results for the CW characterization, as well as the picosecond-scale response to pulsed characterization are presented regarding the responsivity, saturation and gate bias dependence. First, the measurements of the LA-FET devices without AC shunt capacitance are discussed. The results of this study were published in ref. [28]. Subsequently, the results are compared to the improved the LA-FETs with AC shunt capacitance. Finally, the measurements of A-FET detectors are presented and compared to the results from the large-area devices. The results of the A-FET detectors were published in ref. [29].

6.1. Experimental setup

Continuous wave setups

The fabricated and packaged devices are characterized with CW and pulsed THz and MIR radiation. For the experiments conducted in the lab at TU Darmstadt, the CW characterization is carried out using two different table-top sources: an ELVA-1 BWO in the W-band and a frequency-tunable table-top photomixing setup with a commercial HHI/Toptica pin-diode driven by a 1550 nm laser system. A scheme of the characterization setup is shown in Fig. 6.1, the output power of the pin-diode is shown in Fig. 2.4. The THz frequency for characterization can be tuned via the frequency difference of the two DFB laser diodes. The rectified signal from the FET is recorded with a lock-in amplifier connected to source and drain. The THz signal is modulated by biasing the pin-diode at 12 kHz. The bias signal is also fed to the lock-in amplifier as a reference signal for demodulation. The lock-in amplifier (SR 7265 or SR 7270) demodulates the amplitude of the signal at the given modulation frequency. Additionally, it measures the phase difference between the FET signal and the reference modulation signal. The rectified current is measured with a transimpedance amplifier (PDA-S) between FET and lock-in amplifier.

For LA-FET devices of the first generation with lower responsivity, the BWO is used for characterization around 100 GHz. THz is coupled out from the BWO and is fed through an isolator, a variable attenuator, and a horn antenna for outcoupling from the waveguide. Two TPX lenses focus the beam onto the FETs. The power is measured with a thermal power meter (PM4) at the output and at the sample position. The resulting power at the FET position is in the mW range.

The A-FET devices are also characterized using a quantum cascade laser (QCL) in the group of Prof. K. Unterrainer at TU Wien. The QCL operates at 3.8 THz and is bias-modulated at 1.11 kHz for demodulation with a lock-in amplifier [29; 32]. A TPX lens ($f = 50$ mm) and a parabolic mirror collimate the elliptical THz beam. A 28.3 mm^2 pyroelectric detector measured the reference power. The coupling loss to the FET due to the ellipticity of the beam is estimated to 1.75.

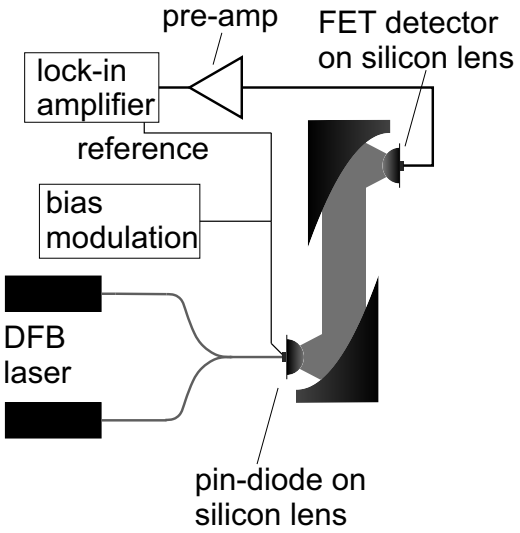

Fig. 6.1: *Table-top photomixing setup for characterization of FET response to THz radiation.*

Free electron laser

For the characterization of the physical detection mechanism of radiation in the THz band and beyond in the FETs, the THz/MIR FEL at the Helmholtz-Zentrum Dresden-Rossendorf (FELBE) is used for measurements at higher frequencies. Further, the measurements at FELBE also allow to demonstrate the capabilities of LA-FETs and A-FETs as direct real-time detectors for picosecond-scale THz pulses with an exceptional frequency coverage. FELBE features two undulators: The U100 undulator covers 1.3 up to 16 THz, the U27 undulator 14 up to 75 THz. The pulses feature a repetition rate of 13 MHz and a linewidth around 1%. The pulse shape at maximum output power is Gaussian [79; 88]. Non-Gaussian pulses due to cavity detuning are studied in chapter 8. The pulses are known to be Heisenberg-Gabor transform limited without additional chirp in the time domain [11]. Due to the fixed linewidth, the Gaussian pulse width is approximately inversely proportional to the frequency. Around 14 to 16 THz, there is a small offset in this behavior, as the two undulators have slightly different natural linewidths. For the frequency range used in this thesis, the resulting Gaussian pulse widths are between $\sigma = 13\,\mathrm{ps}$ (FWHM = 31 ps) at 1.3 THz and $\sigma = 0.9\,\mathrm{ps}$ (FWHM = 2.0 ps) at 30 THz. Strong negative cavity detuning additionally broadens the pulse, and will be discussed in chapter 8. Peak powers of up to 65 kW are used for the study of the FET response.

Fig. 6.2a) shows a scheme of the measurement setup at FELBE at HZDR in Dresden-Rossendorf. The intensity spectrum of the FEL can be measured with a grating spectrometer. The radiation is generated in the FEL and guided to the experimental site with a N_2 flooded beam line. The length of the N_2 flooded beam line between the experimental site and the grating spectrometer is 22 m. Elements for focusing and optional rotation of the linear polarization are placed after the

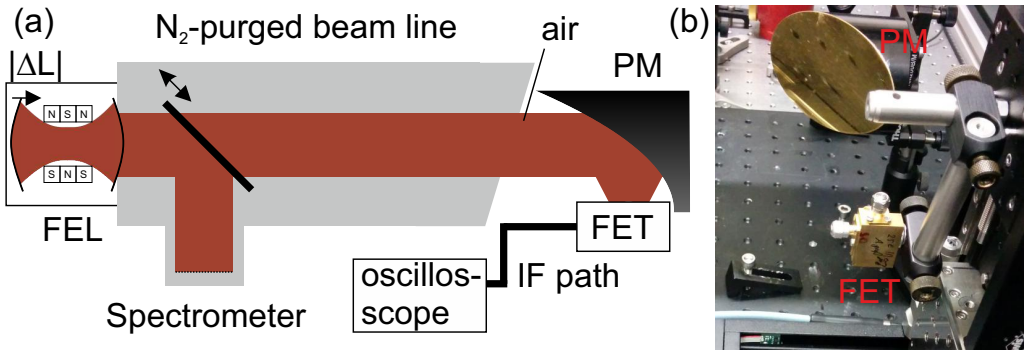

Fig. 6.2: *Measurement setup at FELBE. a) Schematic drawing of the FEL, with N_2-purged beam line, spectrometer and FET with IF path and oscilloscope. Moving one of the mirrors of the FEL cavity determines the cavity detuning ΔL. b) Photograph of the parabolic mirror (PM) focusing THz on a LA-FET in air. Adapted from [30]* ©*IEEE 2019.*

exit window of the N_2 flooded beam line. Selective absorption of THz radiation from water lines narrows the linewidth and widens the temporal pulse width in air. Therefore, care is taken to measure at water vapor transmission windows in the frequency domain. The distance traveled by the FEL pulse in air until reaching the FET is in the range of 3 m. Fig. 6.2b) shows a photograph with the parabolic mirror focusing on the FET detector.

A 30 GHz oscilloscope (Tektronix 80E08 on DSA8200) is used for the fast measurements of the THz/MIR-induced signals in FETs. The oscilloscope's impulse response is in the range of $\sigma_{scope} = 7$ ps for a Gaussian approximation of the rise time specified in the data sheet. For noise reduction, the measured signals are averaged 50 or 100 times. The measured noise floor is still that of the oscilloscope. However, the FETs are capable of real-time detection and measurements on the single pulse level.

A part of the measurements with the devices from the first generation are also carried out with a 10 GHz pre-amplifier for an improved signal-to-noise ratio, however limiting the IF bandwidth.

A thermal power meter is used to measure the average power $\bar{P}_{THz}$. The peak power is calculated as $P_{THz} = \bar{P}_{THz}/(f_{rep} \cdot \mathrm{FWHM})$, with the repetition rate of the FEL and the FWHM pulse width in time domain calculated from the intensity spectra.

CO_2 laser

Additionally, a CO_2 laser in the group of Professor Ganichev at the THz-Zentrum Regensburg is used for characterization at 30 THz. The resulting pulses on the nanosecond-scale are much longer as compared to the FEL pulses at 30 THz on the picosecond-scale. However the CO_2 laser does not show a Gaussian spatial beam profile and shows a temporal instability of competing modes. Therefore the measurements at FELBE show more precise results.

6.2. Large-area field-effect transistors

The devices from Table 5.1 are characterized with THz and MIR radiation from 0.1 up to 30 THz. For each frequency point the optimum gate bias is first identified by measuring the rectified signal. Fig. 6.3 compares the responsivity vs frequency for different LA-FET devices without an AC gate-source shunt capacitance [28]. The plotted responsivity is the ratio of the measured oscilloscope signal referenced to the THz peak power P_{THz}. The LA-FET detectors also work well above the Reststrahlen band of the GaAs substrate which is situated around 8.3 to 10 THz. A measurement at 7.1 THz with a LA-FET device did not give a signal (above the oscilloscope's noise level) [54]. This can be attributed to the tail of the Reststrahlen band leading to absorption in the 500 μm thick GaAs substrate. The LA-FET devices in Fig. 6.3 feature a responsivity of 15 mV/W at 0.1 THz and 0.05 μV/W at 30 THz.

The responsivity is multiple orders of magnitude below antenna-coupled FETs, as the radiation resistance is in the mΩ range. State-of-the-art A-FETs reach responsivities in the range from ten V/W to multiple kV/W [49; 77; 89; 90]. It is to be noted, that the given LA-FET responsivity is referenced to the total peak power and not corrected for the effective antenna aperture [77; 89; 90]. However, for the targeted application as THz detector for ultra-short pulses at high-power facilities, the LA-FET is ideally suited. Further, the antenna-less design allows to achieve an unprecedented frequency coverage without resonances from 0.1 up to 30 THz. Therefore it is ideally suited for ultra-broadband detection of Terahertz radiation.

The measured response of the different detector designs features a f^{-2} roll-off, as indicated by the solid line in Fig. 6.3 [28]. The measured roll-off agrees to the roll-off expected from the electrical coupling efficiency η_{EL} to the FET. η_{EL} is dominated by the RC roll-off from the access impedance Z_{acc} and the gate-drain capacitance C_{GD} (cf. Eq. 3.40). All investigated detectors with different gate lengths and designs show a similar behavior over the large frequency range. The results show that the fabricated FETs with their gate lengths allow ultra broadband THz detection. The LA-FETs do not show resonant features at certain frequency points. Device LA-C features the longest effective rectification length of 0.6 μm at 0.1 THz and 0.3 μm in the high frequency limit in combination with the shortest gate length of 1 μm, fitting only about 2 effective rectification lengths at 0.1 THz. However, it does not show a smaller responsivity around 0.1 THz as compared to the other devices.

This shows that the detectors are well-designed and a gate length of 2 to $3L_{eff}$ suffices for an efficient detection even at low frequencies.

At 1.3 THz and higher frequencies the measurements are carried out at FELBE with pulsed radiation. The THz pulse width of FELBE is approximately inversely proportional to the frequency. At 1.3 THz, the fairly long pulses (Gaussian width $\sigma = 13$ ps, FWHM = 31 ps) can still be resolved well with the 30 GHz oscilloscope. The measured amplitude of pulses with higher frequency is suppressed with η_a, when using FELBE with decreasing pulse width with higher frequency as shown in Fig. 4.6. The dashed line corresponds to the guide to the eye corrected for the limited IF bandwidth from the impulse response of device LA-E and the 30 GHz

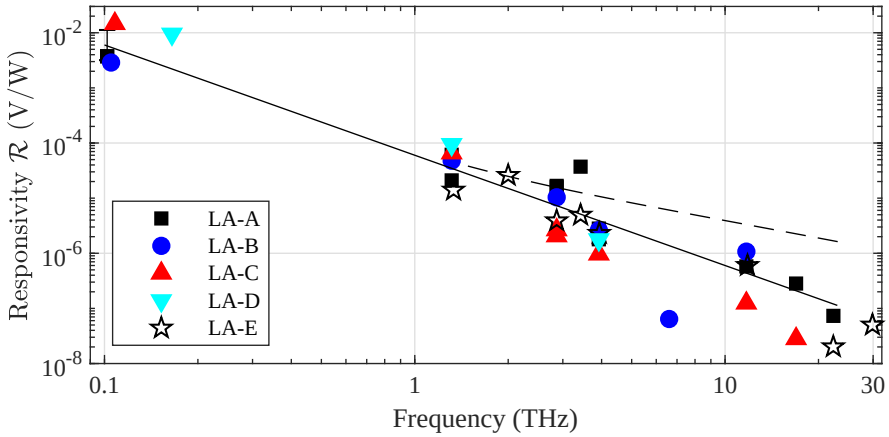

Fig. 6.3: *Measured responsivity of LA-FETs without a gate-source shunt capacitance from* 0.1 *up to* 30 *THz. The data above* 1.3 *THz are measured at FELBE, the data close to* 100 *GHz in a CW setup. Filled symbols represent THz incoupling through a silicon lens, open symbols incoupling from air side. The detectors with different designs show only a slightly different frequency behavior around the* f^{-2} *guide to the eye (solid line). The amplitude suppression due to the IF bandwidth is not corrected for the individual measurements. The dashed line gives a guide to the eye corrected for the amplitude suppression* η_a*. Error bars are included for device LA-A, being smaller than the marker size except for the CW measurement close to* 100 *GHz. Adapted from [28].*

oscilloscope. The CW measurements at the low frequency end are not affected by the IF bandwidth.

Fig. 6.4 shows the data of device LA-E with correction of the limited IF bandwidth using the measured impulse response function. It also includes a comparison to measurements that were done with a CO_2 laser (circle symbol) having much longer pulses compared to the FEL (star symbol). Therefore the measurements at the CO_2 laser are not influenced from an IF limitation with tens of GHz. However the spatial beam profile and temporal stability of lasing modes of the CO_2 laser was not as good as from FELBE. It was non-Gaussian and showed two competing modes on the time domain leading to a larger error in the measurement of the power available to the FET. Despite these technical difficulties, the results with IF correction of FELBE and the CO_2 laser still show good agreement within one order of magnitude.

The observed $f^{-1.4}$ roll-off with corrected amplitude suppression η_a is less strong than a f^{-2} RC roll-off expected for a constant resistance R and capacitance C. The

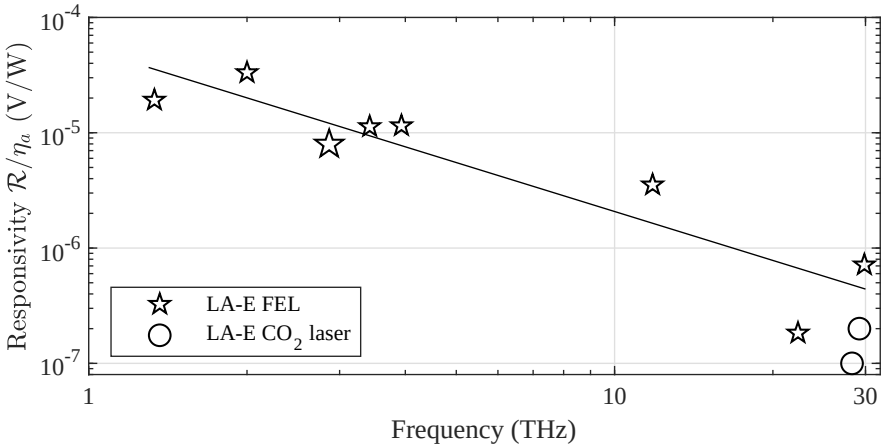

Fig. 6.4: *Measured responsivity of LA-FET LA-E at FELBE and with a CO_2 laser. The amplitude suppression η_a of the limited IF bandwidth has been corrected for the measurement with short pulses at FELBE. A $f^{-1.4}$ guide to the eye is included as a solid line. The larger marker at 2.9 THz indicates the higher error in η_a, due the amplifier.*

responsivity scales as (cf. Eq. 3.37)

$$\mathcal{R} \propto R_A \cdot \frac{1}{1 + (2\pi f (R_A + R_{acc})C)^2} \tag{6.1}$$

$$\lim_{f\to\infty} \mathcal{R} \propto \begin{cases} \frac{R_A}{(2\pi f R_{acc} C)^2} & \text{for } R_{acc} \gg R_A \\ \frac{1}{(2\pi f C)^2 R_A} & \text{for } R_A \gg R_{acc} \end{cases}. \tag{6.2}$$

An increasing radiation resistance R_A with higher frequencies and smaller beam waists $\rho_0 \propto \lambda/\mathrm{NA}$ causes thus a roll-off smaller than f^{-2} for $R_{acc} \gg R_A$ (cf. Eq. 3.47 and Fig. 3.9b)). For the case of a dominating radiation resistance $R_A \gg R_{acc}$, a stronger than f^{-2} roll-off is expected. Further research has to be conducted for a detailed study that could not be realized within the granted beam time at FELBE.

Device LA-A reaches a NEP of $2.7\,\mu\mathrm{W}/\sqrt{\mathrm{Hz}}$ at 0.1 THz in the CW measurements, and a NEP of $0.16\,\mathrm{mW}/\sqrt{\mathrm{Hz}}$ and $45\,\mathrm{mW}/\sqrt{\mathrm{Hz}}$ at 1.3 THz and 22 THz, respectively, in the pulsed measurements. The NEP is limited by the used oscilloscope, as the measured noise was at the value given in the oscilloscope's data sheet.

Linearity

The large active area allows to distribute the THz power, instead of focusing it into a lumped element device. The linearity range should thus be very large for LA-FETs, given that the THz spot size is kept large. In this thesis, up to 65 kW peak power are used. The saturation of the FETs with THz power is modeled with the following ansatz [91]

$$U_{det}(P_{THz}) = U_N + \frac{\mathcal{R} P_{THz}}{1 + [10^{0.1} - 1] P_{THz}/P_{1dB}}. \tag{6.3}$$

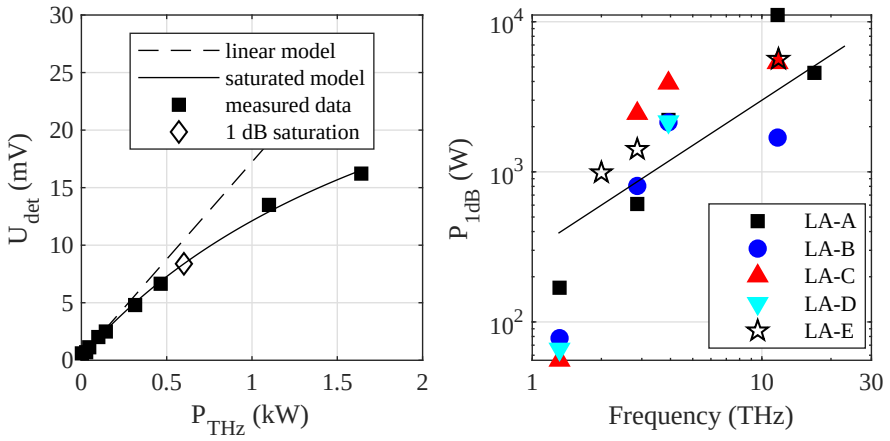

Fig. 6.5: *a) Measured oscilloscope signal from LA-FET LA-A at* 2.9 THz. *At* 0.6 kW *peak power the signal is compressed by* 1 *dB vs linear behavior with* $\mathcal{R} = 17\,\mu V/W$. *b) Peak power of* 1 *dB compression points vs frequency for different LA-FET devices at optimum gate bias. The solid line is a* f^1 *guide to the eye. Adapted with permission from [28], OSA.*

P_{1dB} denotes the 1 dB compression point, where the output signal is saturated 1 dB below the unsaturated linear behavior $\mathcal{R} \cdot P_{THz}$. For the CW measurements, the available power is not high enough to measure saturation. The linearity range from the noise level to the 1 dB compression point is $66 \pm 3\,\mathrm{dB}/\sqrt{\mathrm{Hz}}$ at 1.3 THz, normalized to the oscilloscope bandwidth. With an additional pre-amplifier, it increases to $69 \pm 3\,\mathrm{dB}/\sqrt{\mathrm{Hz}}$.

Fig. 6.5a) shows the detected bias vs THz peak power at 2.9 THz of device LA-A. The 1 dB compression point is marked with an open diamond symbol. Fig. 6.5b) shows the 1 dB compression power P_{1dB} of different detectors vs frequency each at optimum gate bias. The different LA-FET detectors show a 1 dB compression in the order of kW, depending on the frequency. P_{1dB} rises approximately as f^1 for the different devices. The saturation behavior is therefore approximately inversely proportional to the $f^{-1.4}$ responsivity roll-off. P_{1dB} is expected to depend on the (frequency-dependent) beam waist and thus the THz power density on the LA-FET for each measurement. Therefore, there is a strong variation of P_{1dB} for different frequencies with different experimental alignment of the FEL focused to the FET.

The increase in P_{1dB} corresponds to a f^{-1} decrease in the corresponding detected voltage V_{1dB} in the LA-FET, as shown in Fig. 6.6a). After correcting the measured oscilloscope voltage with the frequency dependent amplitude suppression η_a of device LA-E, V_{1dB}/η_a is approximately constant. For the amplitude suppression of LA-A, also the IF bandwidth of LA-E is used, as LA-E features a clear main peak. While the coupling from the detector to the active rectifying element is frequency dependent, the transmission from the FET to the oscilloscope depends on the rectified pulse length and the IF bandwidth. Correcting the amplitude suppression, the output

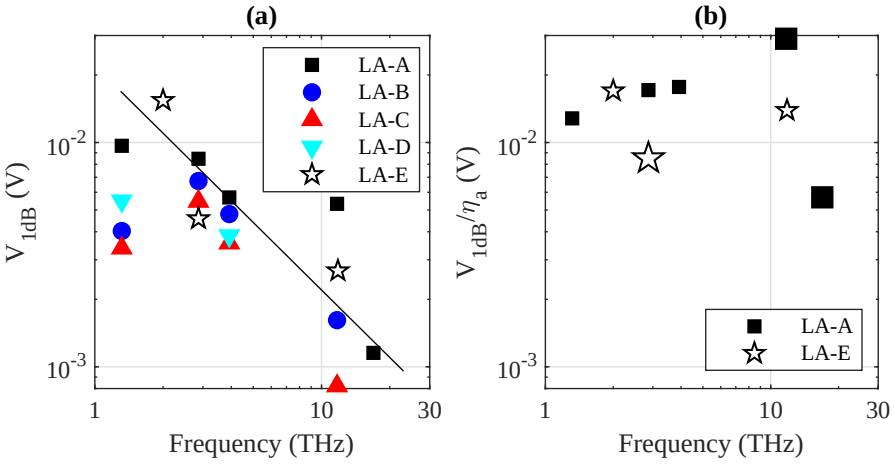

Fig. 6.6: *a) Output LA-FET voltage V_{1dB} at the 1 dB compression point vs frequency. The solid line is a f^{-1} guide to the eye. b) Output LA-FET voltage V_{1dB} corrected for amplitude suppression η_a for device LA-A and LA-E. Larger symbols indicate an increased error in the η_a, due to the use of a pre-amplifier.*

voltage at the 1 dB compression point is therefore expected to be constant with respect to the THz frequency.

Gate bias

For voltage detection, the responsivity is inversely proportional to the charge carrier density (cf. Eq. 3.28). Above threshold, the responsivity scales with the gate bias as $\mathcal{R} \propto \frac{1}{U_{GS}-U_{th}}$ (cf. Eq. 3.39). With more negative gate bias the channel resistance increases and causes also a higher intrinsic noise level originating from the FET.

Fig. 6.7a) shows the change of the rectified signal with gate bias U_{GS} vs frequency for different devices for the pulsed measurements at and above 1.3 THz. The change in signal is normalized to the signal at $U_{GS} = 0$ V. Fig. 6.7b) shows the measurements of device LA-A vs gate bias U_{GS} for each frequency. For higher frequencies the influence of the gate bias on the rectified signal decreases. At 30 THz, there was no change in the measured signal with gate bias of device LA-E. This behavior hints to an additional detection mechanism at high frequencies, other than the Dyakonov-Shur rectification. A diffusion current of thermoelectric origin from heating of the electron gas from the THz/MIR radiation is a possible mechanism generating a THz/MIR induced voltage that can be detected also on a tens of picosecond timescale with a 30 GHz oscilloscope. Slow ($\gg$ 10 ps) thermal effects can be excluded as they would not appear in the oscilloscope measurement. However, as the thermoelectric drift current should depend on differences in charge carrier concentration between gated and ungated areas in the transistor channel, it should also depend on the gate bias (cf. chapter 3.4). Another possible reason for the weaker gate bias dependence is rectification occurring already in the fringing fields of the gate, where the charge carrier density is only weakly affected by the gate bias [92].

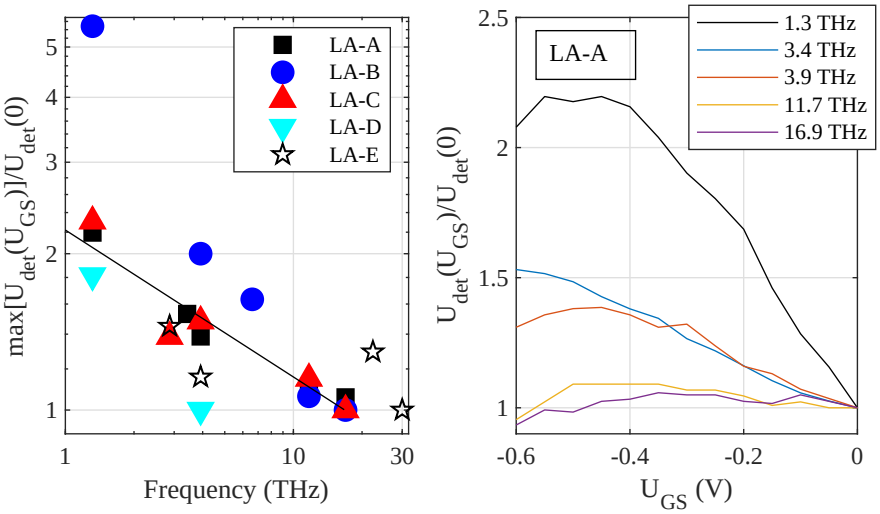

Fig. 6.7: *a) Signal enhancement with gate bias vs frequency. The maximum detected voltage is normalized to the detected voltage at $U_{GS} = 0$ V. The straight line is a $f^{-0.3}$ guide to the eye for the data of device LA-A. b) Respective measurements of device LA-A at the frequency points vs gate bias normalized to detected voltage at $U_{GS} = 0$ V. Adapted from [28].*

The signal changes smoothly with gate bias, there are no sharp resonances visible. For devices with short channels sharp resonances are expected in the plasma resonant regime. For the presented devices the transition to plasma resonant operation ($\omega\tau = 1$) is between 0.7 and 1.0 THz. For higher frequencies ($\omega\tau \geq 1$), plasmons can be excited. Device LA-C with a relatively short gate of 1 μm has an effective rectification length of 0.34 μm at 0.73 THz ($\omega\tau = 1$). The gate length of 3 L_{eff} suffices to reach attenuation of the THz wave along the channel to only have a negligible reflection at the end of the channel. Therefore there are no resonant features visible in the measurements, even though the devices are operated in the plasma-resonant regime ($\omega\tau \geq 1$).

For the pulsed measurements with the oscilloscope with 50 Ω port impedance, the optimum point of operation is at a corresponding DS resistance of $60 \pm 20\,\Omega$ for all investigated devices, matching the impedance of the oscilloscope.

Fig. 6.8a) shows the gate bias dependence at 93 GHz for device LA-B at CW excitation with the BWO. The rectified voltage is measured with a lock-in amplifier. A 180° jump in the phase of the lock-in amplifier indicates a change of the sign of the measured voltage. Fig. 6.8b) shows the measured voltage for different frequencies around 0.1 THz. The gate bias, where the sign flips shifts with respect to the frequency. This behavior can be explained with the symmetry of the FET between the ohmic source and drain contacts [49; 67]. If the THz wave is coupled to the FET from both directions, the two DC signals from the respective rectification compete. At points with zero amplitude, the two rectified DC signals just cancel each other

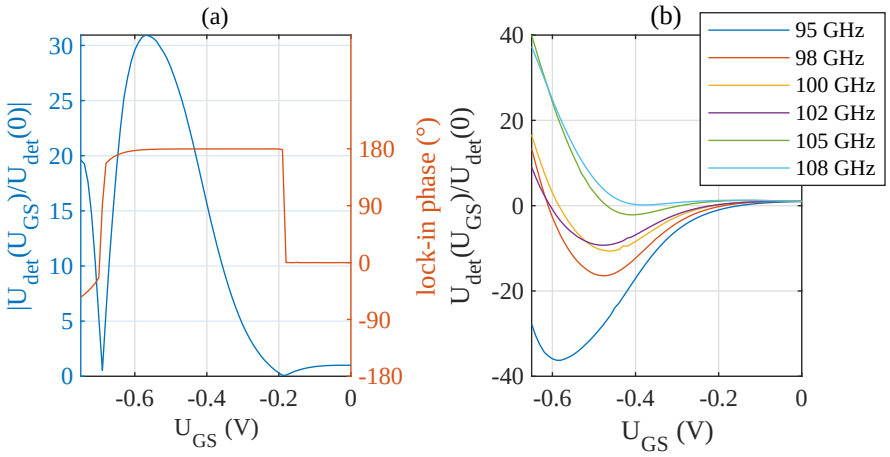

Fig. 6.8: *Signal enhancement with gate bias for device LA-B around* 0.1 *THz. a) The sign of the read-out voltage changes at* $U_{GS} = -0.18$ *V at* 93 *GHz, shown by the 180° phase flip. The change of sign indicates competing rectification processes from both sides of the gate, due to the symmetry of the ohmic source and drain contacts. b) The gate bias, where the sign flips changes with frequency.*

out. The incoupling to the FET can be changed through the gate bias, creating asymmetry in the channel potential. The frequency dependence hints to a change in the incoupling depending on the incident frequency from the BWO.

Devices without strong AC source-gate coupling show a change in the sign of the read-out voltage. A strong AC source-gate coupling should therefore lead to higher measured signals at the output. An AC shunt capacitance can ensure THz coupling from the drain side only, therefore devices with an AC shunt are fabricated and characterized subsequently.

6.3. Large-area field-effect transistors with AC shunt capacitance

Improved FETs with an AC shunt capacitance are designed and fabricated to ensure a well-defined coupling of THz radiation to the FET, proving the superior performance of source-gate coupled devices. The symmetry between the ohmic source and drain contacts is broken in order to achieve coupling of the THz power to the drain side of the gate only. Therefore, there are no competing rectified signals from both sides of the channel. A much higher responsivity can be expected, especially at low frequencies, where the competing rectification is proven by the change of the sign of the read-out bias (cf. Fig. 6.8). Fig. 6.3 compares the responsivity of LA-FETs with and without a source-gate AC shunt capacitance. FETs with an AC shunt, show a strongly improved responsivity. The devices with strong AC source-gate coupling feature about two orders of magnitude higher responsivity on the low frequency end and about one order of magnitude higher responsivity at 2.0 THz for incoupling from the air side.

Device LAS-A features a NEP of $60\,\mathrm{nW}/\sqrt{\mathrm{Hz}}$ at 0.6 THz. At 2.0 THz the NEP is $11\,\mu\mathrm{W}/\sqrt{\mathrm{Hz}}$, limited by the oscilloscope's noise level. The 1-2 orders of magnitude lower NEP allows a more sensitive measurement of pulses with less peak power. Further, an additional pre-amplifier, that limits the IF bandwidth is not required anymore for the measurement. The measured pulse width is therefore less broadened by the IF limitations of a pre-amplifier.

At 2.0 THz, the THz coupling from the air (open red triangle) and substrate side (closed red triangle) is compared for the very same device [87]. Fig. 6.10b) shows the setup for incoupling from the air with the cone aperture and from the substrate side. Fig. 6.10a) shows the measured pulses for incoupling from the air and substrate side of device LAS-A at 2.0 THz, respectively. The temporal pulse width is unaffected, only the ringing after the main pulse changes slightly.

The diffraction-limited beam waist is estimated to $\rho_0 = \frac{1.22\lambda}{\mathrm{NA}} = 1.3\,\mathrm{mm}$ (0.36 mm) in air (substrate) at 2.0 THz for the used experimental setup with a NA of 0.14. The aperture efficiency η_A, i.e. the power of a Gaussian beam contained in the radius r relatively to the total power can be calculated as

$$\eta_A = P(r)/P_{tot} = 1 - e^{-2(r/\rho_0)^2}. \tag{6.4}$$

Through the incoupling from the air side and the larger spot, a factor $\eta_a \approx 2.2$ of THz power is lost compared to the incoupling from the substrate. The beam intensity is concentrated on a smaller part of the LA-FET for incoupling from the substrate. Therefore, the radiation resistance R_A is expected to increase by about a factor 1.5 for incoupling from the substrate (cf. Fig. 3.9), yielding a total improvement of a factor 3.3 by substrate coupling. The measured ratio between incoupling from the air and substrate side is about 5.5, with no significant dependence on the gate bias as discussed later. The measured difference is therefore slightly above the expectations.

The incoupling from the substrate is thus beneficial for an improved signal-to-noise ratio (SNR) and thus higher sensitivity, with unaffected temporal rise time.

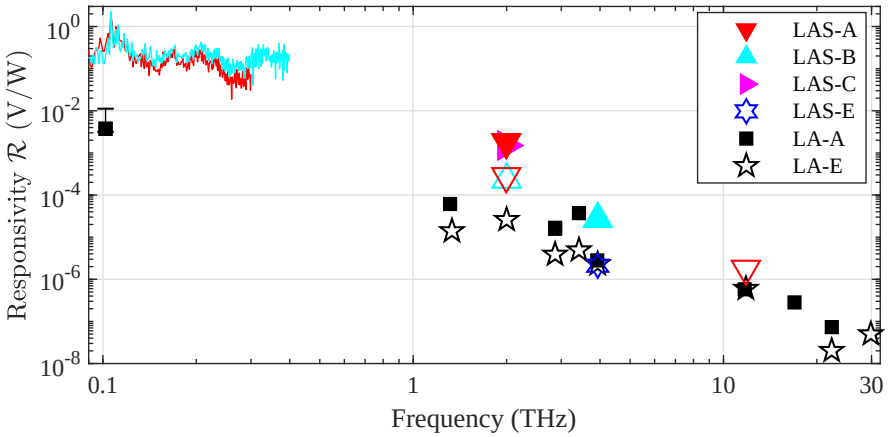

Fig. 6.9: *Measured responsivity of LA-FETs with and without an AC source-gate shunt capacitance. Filled symbols represent THz incoupling through a silicon lens, open symbols incoupling from the air side. The devices with strong coupling show about two orders of magnitude improved responsivity at* 0.1 *THz on the low frequency end and a factor* 3 *improvement at* 11.8 *THz. At* 3.9 *THz device LAS-B with strong AC coupling shows an order of magnitude enhanced responsivity compared with device LA-A, both measured with incoupling from the lens side. Whereas the devices LA-E and LAS-E with THz coupled from the air side show a similar responsivity at* 3.9 *THz, despite different design. The THz beam is coupled to the* $0.3 \times 0.3\,mm^2$ *device LAS-A from the lens (filled triangle) and from the air side (empty triangle). At* 2.0 *THz there is about a factor* 6 *enhanced incoupling from the silicon lens compared to the incoupling from the air side.*

Linearity and gate bias

Fig. 6.11a) shows the linearity range of device LAS-A at 2.0 THz for front and backside coupling. The 1 dB compression is $P_{1dB} = 12 \pm 3\,\mathrm{W}$ ($\approx 370 \pm 100\,\mathrm{W}$) for coupling from the lens side (air side), respectively. This factor 30 difference is a factor 5.5 higher compared to the difference in responsivity. This agrees very well with a power concentrated in a factor n^2 smaller area for coupling from the substrate side ($n = 3.6$) together with a factor 2.2 power loss.

Device LAS-A with AC shunt features a (IF corrected) responsivity of 0.8 mV/W at 2.0 THz, whereas device LA-E without ac shunt features a (IF corrected) responsivity of 0.03 mV/W at 2.0 THz with a 1 dB compression $P_{1dB} = 1.0\,\mathrm{kW}$, both for coupling from the air side. While the responsivity increases by more than an order of magnitude, the 1 dB compression power P_{1dB} only decreases by a factor of 3, proving the superior performance of the design with AC shunt for THz detection.

Fig. 6.11b) shows the change in the responsivity of device LAS-A with the gate bias for incoupling through the substrate and from the air side, respectively. The incident THz power from the FEL was 7.4 times lower for incoupling from the lens side, to account for the higher responsivity for incoupling from the substrate. There

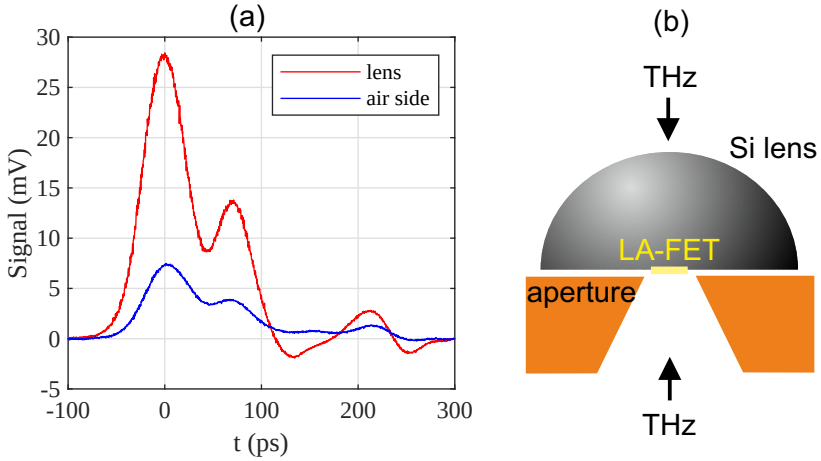

Fig. 6.10: *a) Measured pulses with device LAS-A at 2.0 THz for incoupling through the lens and from the air side. Both measurements are with the same THz power and under the same gate bias $U_{GS} = -0.3$ V. Incoupling from the substrate side increases the signal by a factor 5.5. b) Schematic of incoupling though the lens and from the air side. The inner 0.5 mm cone aperture shields the wiring of the LA-FET from undesired incoupling. With its outer diameter of 3.6 mm it can also partially focus THz beams with large beam waists onto the $0.3 \times 0.3\,mm^2$ active area of the LA-FET.*

is no strong difference of the gate bias dependence for incoupling from the lens or the substrate side, for $U_{GS} > 0.38$ V there is a small offset in the responsivity. The optimum gate bias is $U_{GS} = -0.3$ V, where the SD resistance is $\approx 20\,\Omega$, being close to impedance matching of the used $50\,\Omega$ oscilloscope.

Fig. 6.12a) shows the dependence of the rectified signal in device LAS-A at 200 GHz at a lock-in amplifier with MΩ impedance, where the device is operated in the photovoltaic mode. The signal increases for more negative gate bias along with higher channel resistance. This is an expected behavior, due to the MΩ impedance of the lock-in amplifier. For the current read-out, the device is attached to a transimpedance amplifier prior to lock-in detection, that features an input resistance in the range of $20\,\Omega$. Fig. 6.12b) shows the read-out current vs gate bias, reaching a maximum signal at $U_{GS} = -0.45$ V with a threshold bias of $U_{th} = -0.51 \pm 0.05$ V. Along with the channel resistance, also the noise generated by the FET increases, therefore the operation point with maximum responsivity and minimum NEP may differ. The minimum NEP was achieved in current read-out at a gate bias of $U_{GS} = -0.38$ V with a value of $60\,\mathrm{nW}/\sqrt{\mathrm{Hz}}$.

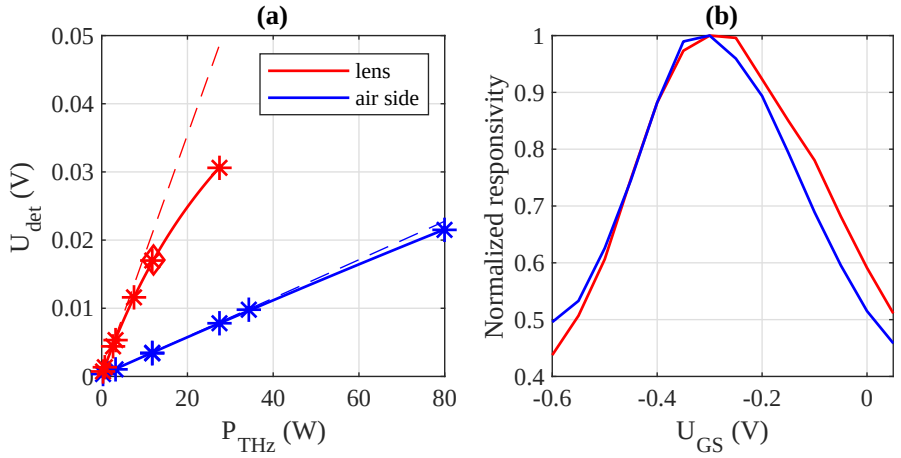

Fig. 6.11: *a) Comparison of linearity for coupling through substrate (red symbols) and air (blue symbols) at 2.0 THz for device LAS-A at $U_{GS} = -0.3$ V. b) Signal vs gate bias at 2.0 THz for device LAS-A. For incoupling through the substrate (red line), the signal enhancement is similar compared to incoupling from the air side (blue line). The responsivity is normalized to the respective maximum value.*

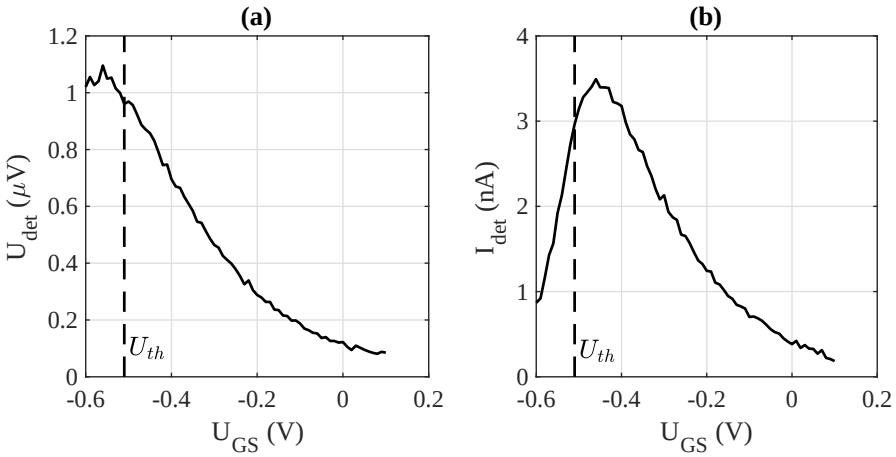

Fig. 6.12: *Measured signal vs gate bias U_{GS} for device LAS-A at 0.2 THz. a) Voltage signal increases with more negative U_{GS}. b) Current signal with a maximum at $U_{GS} = -0.45$ V.*

6.4. Antenna-coupled field-effect transistors

An antenna enhances the incoupling of THz power to the FET strongly due to the much higher radiation resistance of the A-FET in comparison with the LA-FET devices (cf. Fig. 3.7). Fig. 6.13 compares the responsivity of the A-FET device AN-B from 0.1 up to 12 THz along with LA-FETs. In the following paragraphs, the results of the LA-FET device LAS-A and the A-FET device AN-B, both with an AC shunt capacitance, are compared. The responsivity $\mathcal{R}$ is proportional to the radiation resistance R_A, channel resistance R_{ch} and the coupling efficiencies $\eta_{tot} = \eta_p \eta_{Op} \eta_A \eta_{El} \eta_{DCV}$ (cf. Eq. 3.37). The ratio of the respective responsivities calculates to:

$$\frac{\mathcal{R}^{AN}}{\mathcal{R}^{LA}} = \frac{\eta_{tot}^{AN} R_{ch}^{AN} R_A^{AN}}{\eta_{tot}^{LA} R_{ch}^{LA} R_A^{LA}}. \tag{6.5}$$

To facilitate the comparison of the concepts, LA-FET device LAS-A and A-FET device AN-B were fabricated with the same semiconductor material, η_p^{AN}/η_p^{LA} is thus 1. Both devices feature similar channel and gate lengths, thus η_{El} is similar for both FETs, therefore expecting $\eta_{El}^{AN}/\eta_{El}^{LA} \approx 1$ (cf. Table 5.1).

For both devices the radiation is coupled through a silicon lens to the FETs, except for 11.8 THz, where the device LAS-A with an active area of $0.3 \times 0.3\,\mathrm{mm}^2$ is only characterized from the air side. The effective receiving area of an antenna is $A = \lambda^2 G/(4\pi)$, with the gain $G = 10$ for the spiral antenna [73]. At 300 GHz the resulting effective receiving area with $0.34 \times 0.34\,\mathrm{mm}^2$ is therefore about the same as the active area of the LA-FET [93]. Thus the aperture efficiency η_A is similar for both devices at 300 GHz. The optical efficiency differs by $\eta_{Op}^{AN}/\eta_{Op}^{LA} = 0.55$, as the spiral features a circular polarization at 300 GHz. The read-out efficiency η_{DCV} is similar for both devices, as the MΩ-resistance of the lock-in amplifier is orders of magnitude above the kΩ-resistance of the FET devices. The A-FET shows a factor $\frac{\mathcal{R}^{AN}\eta_{Op}^{LA}}{\mathcal{R}^{LA}\eta_{Op}^{AN}} \approx 300$ higher responsivity at 300 GHz, with a comparable receiving area at optimum gate bias, accounting for the circular polarization of the A-FET [93].

The radiation resistance of the LA-FET and A-FET can thus be compared experimentally as follows: The simulated radiation resistance is $R_A^{AN} = 53\,\Omega$ for the A-FET (cf. Fig. 3.7), the ratio of the channel resistances is $R_{ch}^{AN}/R_{ch}^{LA} \approx 4$ at the respective optimum gate bias (cf. Fig. 5.4b)). The radiation resistance of the LA-FET, calculated from the difference of the responsivities using Eq. 6.5 is thus $0.04\,\Omega$ at 300 GHz. This is about one order of magnitude higher as the analytically calculated value of $6\,\mathrm{m}\Omega$ with a beam waist of 0.3 mm (cf. Eq. 3.47).

Though both devices feature the very same material parameters, the much wider design of the LA-FET potentially causes a smaller parasitic resistance and suggests a higher efficiency η_{El}. This would also cause a deviation between calculated and indirectly measured radiation resistance.

At higher frequencies, the responsivity difference between the LA-FET and the A-FET device becomes smaller. At 2.0 THz, there is only a factor of $\mathcal{R}^{AN}/\mathcal{R}^{LA} = 1.6$ difference in the measured responsivities for incoupling from the substrate side for

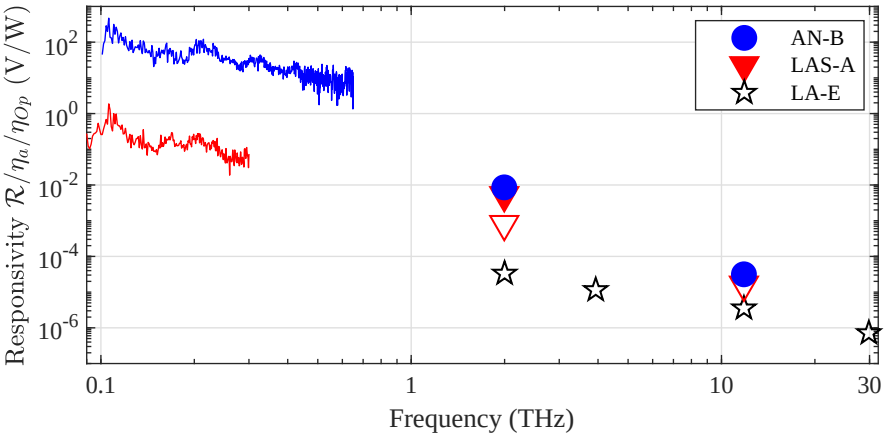

Fig. 6.13: *Comparison of responsivity between LA-FET (black and red) and A-FET (blue) devices. The displayed responsivity is corrected for the amplitude suppression η_a and for the polarization mismatch of the A-FET η_{Op}. Filled symbols represent THz incoupling through a silicon lens, open symbols incoupling from air side. The CW measurements below 1 THz are for coupling through the silicon lens.*

both devices. The smaller difference at higher frequencies is expected, as 2.0 THz is about a factor of 2 larger than the design operation range of the antenna. The performance is further altered by the 30 μm wide FET in the center of the antenna. This leads to a simulated radiation resistance of only $R_A = 2.6\,\Omega$ compared to the theoretical value for a self-complementary antenna of $R_A = 72\,\Omega$. At 2.0 THz the effective antenna area is only $0.05 \times 0.05\,\mathrm{mm}^2$, therefore the aperture efficiency ratio calculates to $\eta_A^{AN}/\eta_A^{LA} \approx 0.1$. From the measured responsivity difference $\mathcal{R}^{AN}/\mathcal{R}^{LA}$, η_A^{AN}/η_A^{AN}, and $R_{ch}^{AN}/R_{ch}^{LA} \approx 4$ the radiation resistance calculates to $R_A^{LA} = 41\,\mathrm{m}\Omega$ for the simulated value of the A-FET using Eq. 6.5. This is in very good agreement with the theoretically expected $R_A = 32\,\mathrm{m}\Omega$ of the LA-FET.

At higher frequencies the responsivity of the A-FET drops to the level of the LA-FET. When the wavelength is similar to the dimensions of the FET in the center of the antenna, the THz wave directly interacts with the 30 μm wide FET, similar to a LA-FET.

For an improved NEP, zero-bias operation is desirable. An additional voltage source connected to the gate can be omitted, that can introduce excess noise to the read-out signal. Further, the setup and fabrication of the FET devices can be facilitated, not requiring electrical connection of the gate terminal. Device AN-A qualifies for zero-bias operation with a DC transconductance peaking close to $U_{GS} = 0\,\mathrm{V}$ (cf. Fig. 5.5). Fig. 6.14 compares the current responsivity for both A-FET devices AN-A and AN-B with the theoretically expected current responsivity from the transmission line model. The theoretically expected current responsivity takes the access impedance, as well as the simulated radiation resistance and gate-drain capacitance into account (cf. Eq. 3.42). The pulsed measurements of device AN-B at 2.0 and 11.8 THz are

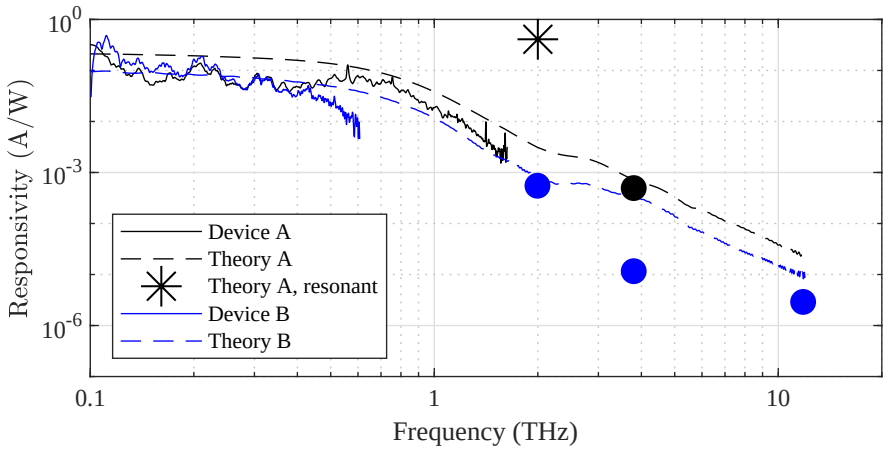

Fig. 6.14: *Comparison of measured and simulated current responsivity $\mathcal{R}_I$ of A-FET devices vs frequency. The given responsivity is referenced to the total peak power of the different THz sources and corrected for the amplitude suppression η_a for the pulsed measurements at 2.0 and 11.8 THz, the frequency dependent polarization η_{Op}, the aperture efficiency η_A and the DC read-out efficiency η_{DCI}. The star at 2 THz corresponds to the expected responsivity of a narrowband resonant antenna.*

corrected for the limited IF bandwidth of the A-FET from the measured impulse response. The data are further corrected for the optical efficiency η_{Op}, determined by the 30% reflection of the silicon lens and the frequency dependent polarization mismatch between the spiral antenna and the linearly polarized THz sources, DC read-out efficiency η_{DCI} and the aperture efficiency η_A. The aperture efficiency η_A calculates to $\eta_A = P(r)/P_{tot} \approx 0.6$ ($\eta_A = P(r)/P_{tot} \approx 0.4$) for the parameters of the CW (FEL) measurements, the read-out efficiency η_{DCI} calculates to ≈ 0.8 (cf. Eq. 6.4 and Eq. 3.42).

There is excellent agreement over the large frequency span from 0.1 up to 11.8 THz between the rather simple theoretical model and the measured data. To the knowledge of the author, this is the largest frequency range reported so far on the comparison of single devices to the equivalent circuit model [29].

For the zero-bias device AN-A with a 15 μm wide FET there is only a minor drop in responsivity from 0.1 up to 0.6 THz with less than a f^{-1} roll-off. This in agreement with theoretical expectations with neglible access resistance in the non-resonant regime ($\omega\tau < 1$) [55]. Above 0.6 THz the gate-drain capacitance, access impedance and a drop in the radiation resistance from the ideal value can not be neglected anymore, leading to a roll-off between f^{-3} and f^{-4} in the used model as well as the measured data. With the measured noise level, measurement bandwidth and only correcting for the 30% reflection of the silicon lens and the polarization mismatch and referencing to the total power of the THz beam, that may easily be obtained experimentally with an ARC coating and using a linearly polarized antenna, the NEP calculates to 250 pW/$\sqrt{\text{Hz}}$ [29]. 250 pW/$\sqrt{\text{Hz}}$ are only one order of magnitude

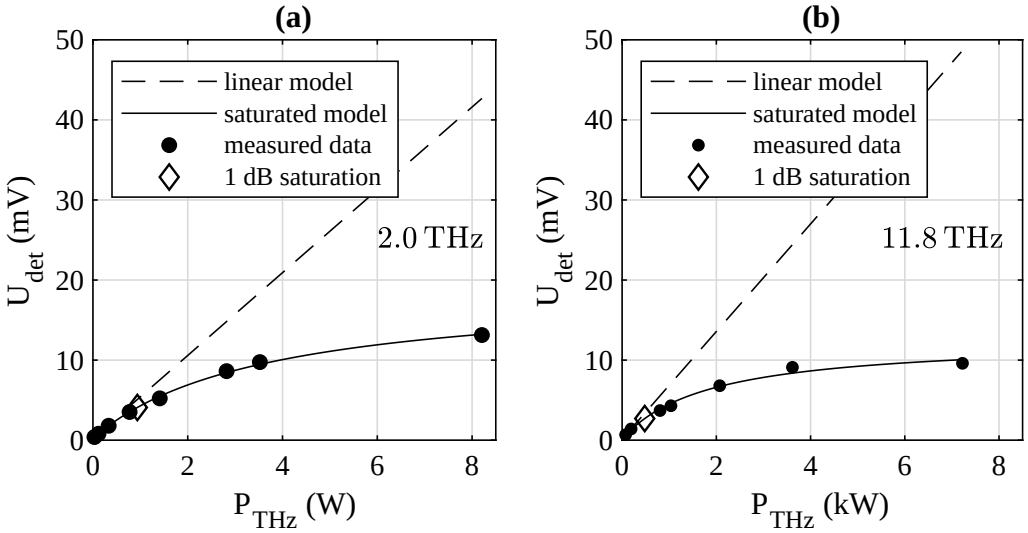

Fig. 6.15: *a) Measured signal of device AN-B vs peak power at* 2.0 *THz. The* 1 *dB saturation point is* $P_{1dB} = 1$ *W. b) Measured signal of device AN-B vs peak power at* 11.8 *THz. The* 1 *dB saturation point is at* $P_{1dB} = 0.48\,\mathrm{kW}$.

above FETs fabricated in 65 nm foundry processes, though the A-FET is fabricated with simple UV-contact lithography. Additionally correcting the responsivity for the aperture efficiency η_A and the DC read-out efficiency η_{DCI}, the NEP calculates to $120\,\mathrm{pW}/\sqrt{\mathrm{Hz}}$ at 0.6 THz. The star in Fig. 6.14 indicates the expected two orders of magnitude improved responsivity for a narrowband conjugate-matched antenna at 2.0 THz.

In comparison with the published study in ref. [29], the CST simulations of the radiation impedance Z_A are improved (cf. Fig. 3.7) and the IF limitations η_a are corrected. The antenna simulations showed an unphysical mode perpendicular to the FET channel leading to a resonance at 3.7 THz, that was also not observed experimentally. The improved CST simulations feature a 2 dimensional port in the center of the metalization connecting the FET instead of a 1 dimensional port as used in ref. [29]. The improved simulations of Z_A, correction of the limited IF suppression η_a, read-out efficiency η_{DCI}, and aperture efficiency η_a result in better agreement of the calculated responsivity to the experimental data.

Linearity and gate bias

For antenna-coupled devices with μm-dimensions a much smaller linearity range is expected as compared to large-area devices with $0.3 \times 0.3\,\mathrm{mm}^2$ or $1 \times 1\,\mathrm{mm}^2$ active area. In the antenna-coupled devices, the THz power is coupled to a lumped element FET, while large-area devices allow the distribution of the power. Fig. 6.15a) shows the detected signal with respect to the FEL peak power at 2.0 THz. The respective 1 dB compression point is at $P_{1dB} = 1\,\mathrm{W}$. Fig. 6.15b) shows the saturation behavior of device AN-B at 11.8 THz. The 1 dB compression point is at $P_{1dB} = 0.48\,\mathrm{kW}$.

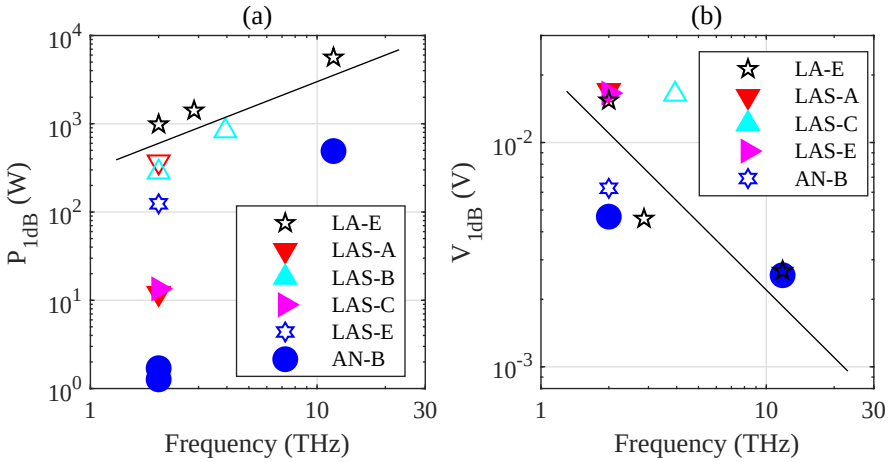

Fig. 6.16: *a) Comparison of 1 dB compression of antenna-coupled device AN-B with large-area devices with and without AC shunt capacitance. A f^1 guide to the eye is included as solid line. b) Respective output voltage V_{1dB} at 1 dB compression point. A f^{-1} guide to the eye is included as solid line. Filled symbols represent THz incoupling through a silicon lens, open symbols incoupling from air side.*

Fig. 6.16a) compares the saturation behavior of the different devices with different concepts: antenna-coupled FET, large-area FET with AC shunt, and large-area FET without AC shunt. At low frequencies, where the responsivity of antenna-coupled devices is orders of magnitude higher compared to the LA-FETs, the linearity range is accordingly smaller. At higher frequencies along with smaller responsivity, the linearity range increases. The respective detector output voltage V_{1dB} at the 1 dB compression point decreases with increasing frequency (cf. Fig. 6.16b)). The strong variation of P_{1dB} vs frequency is accounted to the amplitude suppression and different beam waists for different frequencies at FELBE. The difference between the A-FET and LA-FET device becomes smaller for higher frequencies, as the beam waist becomes a factor ≈ 6 smaller from 2 to 12 THz. The similar behavior can be accounted to the dimensions of the A-FET being in the range of the wavelength and the focusing the THz power on a smaller fraction of the LA-FET. Correcting for the amplitude suppression η_a, all different detector concepts show a similar V_{1dB} output voltage in the 10 mV range (cf. Fig. 6.17a)). The output voltage V_{1dB} can therefore be regarded as measure for saturation for both μm wide A-FETs, as well as for mm wide LA-FETs.

Fig. 6.17b) shows the signal detected with the oscilloscope vs gate bias at 2.0 THz. There is only a slight signal enhancement at $U_{GS} = -0.2$ V. Approaching the threshold of $U_{th} = -0.53 \pm 0.05$ V with more negative gate bias, the signal drops. The resistance of device AN-B is already higher than 50 Ω at the most positive gate bias, therefore impedance matching to the 50 Ω oscilloscope cannot be obtained.

Fig. 6.18 compares the relative change in responsivity for the devices AN-B and LAS-A vs gate bias. The photovoltaic response is measured at a lock-in amplifier

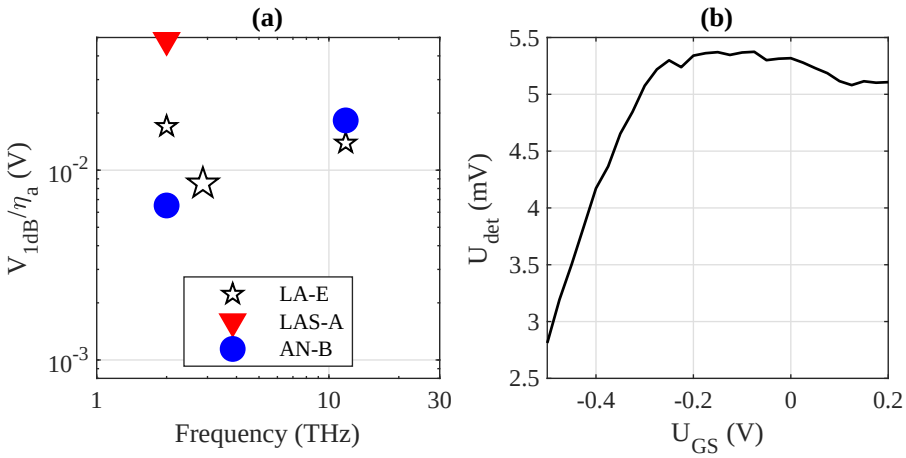

Fig. 6.17: *a) Output voltage V_{1dB} at 1 dB compression point corrected for amplitude efficiency η_a (cf. Fig. 6.16b)). b) Measured signal vs gate bias at 2.0 THz. There is only a weak signal enhancement of device AN-B compared to $U_{GS} = 0$ V.*

with MΩ impedance, the photocurrent response with a transimpedance amplifier. The photovoltaic response is expected to be proportional to the channel resistance $\mathcal{R} \propto 1/n_0 \propto R_{ch}$ (cf. Eq. 3.37). The antenna-coupled device AN-B features a much stronger responsivity enhancement compared to the large-area device LAS-A at 200 GHz [93]. The respective threshold biases of the devices AN-B and LAS-A are $U_{th} = -0.53 \pm 0.05$ V and $U_{th} = -0.51 \pm 0.05$ V and thus identical within the measurement accuracy, as they are processed on the same semiconductor material. This agrees with a higher channel resistance R_{ch} of the antenna-coupled device and a stronger increase of $R_{DS} = R_{ch} + R_{acc}$ with more negative gate bias (cf. Fig. 5.4). The access resistance R_{acc} is constant.

The photocurrent response $\mathcal{R}_I$, mainly depends on the material parameters of the HEMT material and the coupling efficiencies (cf. Eq. 3.38). The read-out current increases with more negative gate bias, but reaches a maximum at $U_{GS} = -0.4$ V ($U_{GS} = -0.45$ V) for device AN-B (LAS-A) and drops again.

De-embedding the internal responsivity

The internal responsivity of the rectifying element with the impedance Z_{TL} can be obtained from the measured responsivity by de-embedding [66]. Dividing the responsivity from the transmission line model by the coupling efficiencies as $\mathcal{R}_I/(\eta_{El}\eta_{Op}\eta_A\eta_{DCI})$ gives the ideal responsivity $\mathcal{R}_I^{id} \propto \mu R_a \eta_p$ (cf. *Eq.* 3.38).

Fig. 6.19 shows the de-embedded responsivity $\mathcal{R}_I^{de} = \mathcal{R}_I/(\eta_{El}\eta_{Op}\eta_{DCI}\eta_A)$ in comparison with the ideal responsivity $\mathcal{R}_I^{id}$, that is calculated from the radiation resistance and material parameters. At 0.6 THz, an ideal responsivity of $\mathcal{R}_I^{id} = 6$ A/W is expected. The de-embedded measured responsivity shows excellent agreement to the ideal responsivity. The ideal responsivity can be further increased by using an antenna with larger radiation resistance. The ideal responsivity including a radiation

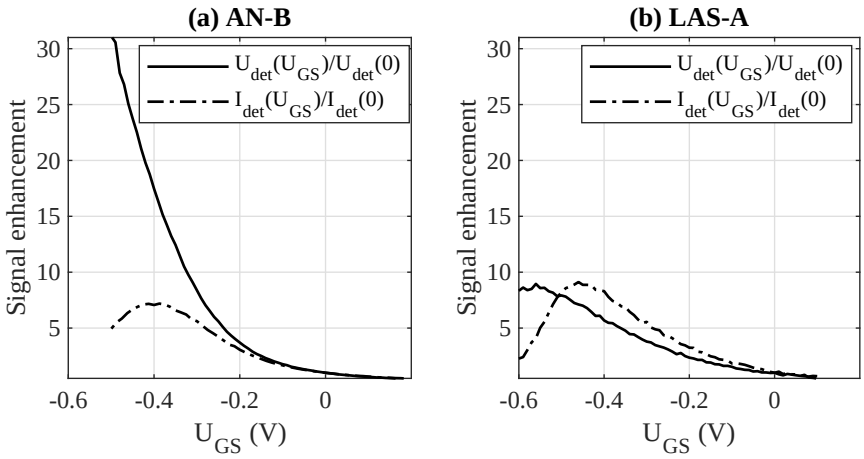

Fig. 6.18: *Comparison of signal enhancement for the photovoltaic and photocurrent detection mode with gate bias at* 0.2 *THz. a) Device AN-B b) Device LAS-A.*

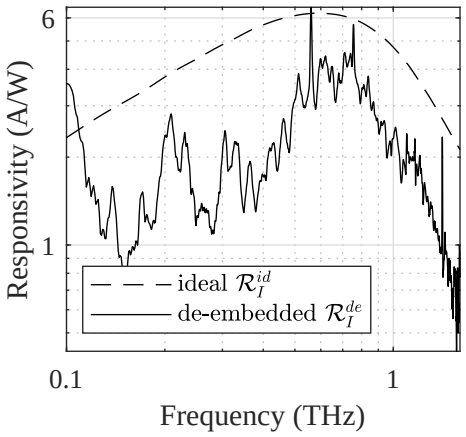

Fig. 6.19: *De-embedded current responsivity* $\mathcal{R}_I^{de}$ *and ideal responsivity* $\mathcal{R}_I^{id}$.

resistance is close to the intrinsic responsivity of Schottky diodes of 20 A/W.

7. Discrimination of non-Dyakonov-Shur-like response

This chapter compares the FET response to reference samples without gate contact. First, the picosecond-scale response is discussed. Second, the picosecond-scale response is compared to the millisecond-scale response including 2D raster scans of the detector area.

7.1. Quantification of signal contribution

In order to discriminate FET detection from other fast detection mechanisms on the piscosecond-scale, the fast FET response from the previous chapter is compared with gate-less reference samples.

One possible additional mechanism for rectification of kW THz pulses is a faint non-linear current voltage $\chi^{(2)}$ characteristic in imperfect source and drain contacts. The non-linear processes leading to a DC read-out from ohmic contacts can be quantified with reference samples. The reference samples do not have gate electrodes, and are thus no FETs (cf. Fig. 5.1c)). The THz induced voltage of reference devices without Schottky contacts is measured at 2.0, 3.9, 11.8 and 30 THz at FELBE. The difference between the measured responsivity of a FET and a reference sample without gate contacts can then only arise from Dyakonov-Shur-like rectification or other mechanisms that require a gate electrode, such as a thermoelectric diffusion coefficient (cf. chapter 3.4).

Fig. 7.1 shows the comparison between the large-area gate-less devices NG-A and NG-B with the FET devices LAS-A and LAS-B with strong source-gate coupling and device LA-E with weak source-gate coupling. The devices were fabricated on the same semiconductor material to facilitate the comparison, except for device LA-E (cf. Table 5.1). Device NG-A features a channel length of 6 μm similar to device LAS-A and LAS-B with 4.5 μm. The responsivity is measured at FELBE with a 30 GHz oscilloscope. At 2.0 THz the signal of the gate-less device is suppressed by more than two orders of magnitude in comparison with FET device LAS-A, both for incoupling from the air side. For incoupling through the lens at 3.9 THz, the responsivity of device LAS-B is a factor 60 larger, compared to device NG-A. At 11.8 THz the signal from device NG-A without gate is a factor 10 below device LAS-A. The responsivity at 11.8 THz of device LA-E without strong gate-source coupling is only a factor 4 (factor 2) above the gate-less device NG-A (NG-B).

At 30 THz, no signal could be measured with the oscilloscope with the gate-less device NG-B. With the oscilloscope noise floor and the available peak power, the upper limit for the responsivity calculates to 1.2 nV/W. The responsivity is therefore at least a factor 40 below the measured responsivity of FET device LA-E. With the CO_2 laser, no signal could be measured for device NG-C. With the noise level in the measurement, the upper limit of the responsivity can be calculated to an order of magnitude below the response of device LA-E in agreement with the upper limit

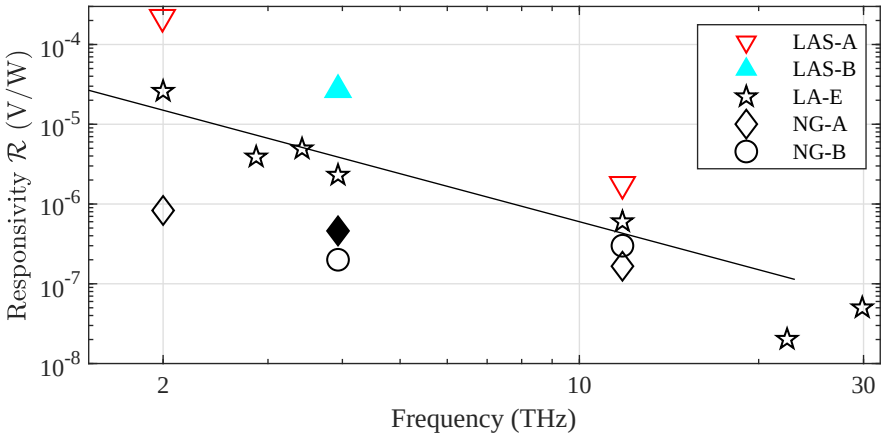

Fig. 7.1: *Responsivity of gate-less samples measured at FELBE. Comparison with FET devices LAS-A, LAS-B, and LA-E. Open symbols represent incoupling from air side, filled symbols incoupling through the lens. The responsivity of the devices LAS-A and LAS-B is at least one order of magnitude above device NG-A without gate contact with similar design.*

from the FELBE measurements.

From the oscilloscope measurements of the reference devices it can be concluded that the fast response from rectification mechanisms not including a gate electrode, such as from imperfections of the contacts is at least an order of magnitude lower for a similar channel length and the same material parameters. However, for FETs without strong gate-source coupling, the difference from the FET response to the gate-less response is less than an order of magnitude at 11.8 THz.

Fig. 7.2a) shows the signal of device NG-B vs THz peak power at 3.9 THz. With the power available at 3.9 THz from FELBE at the specific user station, no saturation could be observed. Fig. 7.2b) shows a typical detected oscilloscope signal of device NG-A at 2.0 THz. First there is a small positive peak, followed by the larger negative main peak. The ringing after the main peak can be attributed to reflections in the IF path. The peak structure differs substantially from those found with FETs.

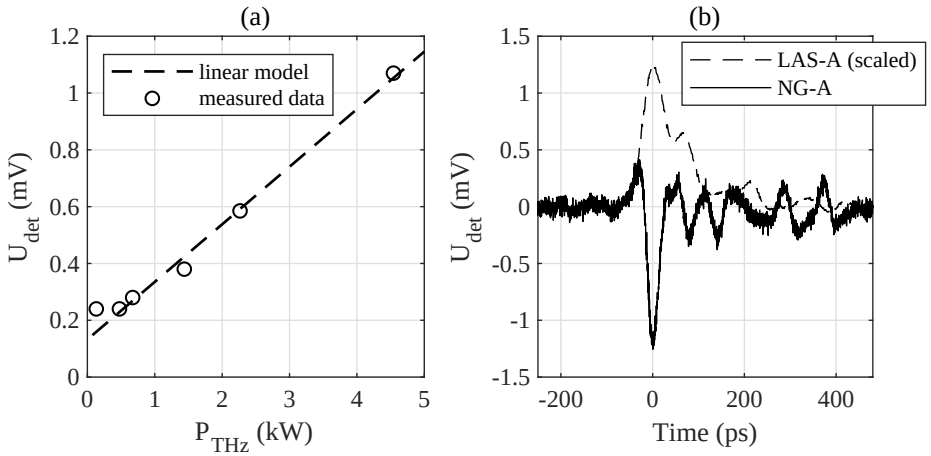

Fig. 7.2: *a) Oscilloscope signal vs peak power of device NG-B at* 3.9 *THz. With the available power, no saturation could be observed. b) Measured oscilloscope signal from device NG-A at* 2.0 *THz. The peak structure differs substantially from the signal from device LAS-A at* 2.0 *THz. The signal of device LAS-A is scaled to device NG-A for the comparison.*

7.2. Discrimination of picosecond-scale and millisecond-scale response

The preceding section discusses the fast response of LA-FETs, A-FETs and gate-less reference samples to picosecond-scale THz and MIR pulses. On this timescale, the measurement process is insensitive to bolometric effects which usually require several tens of nanoseconds for thermalization. This section compares the fast (picosecond-scale) response of LA-FETs and gate-less reference samples to their slow, thermal (millisecond-scale) response. In order to determine the part of the LA-FET where the detection takes place, a THz beam 2D scans the large-area samples. The LA-FET detectors and gate-less samples are therefore mounted on a motorized 2D stage. The measured image is thus a convolution of the active area of the detectors with the THz beam waist.

The fast response is measured with a 30 GHz oscilloscope, as in the preceding chapter, while the ms-scale response is measured with a lock-in amplifier. Slow thermal effects contribute thus only to the millisecond-scale response. A chopper wheel modulates the THz radiation at around 220 Hz for detection of the current with the lock-in amplifier. Both types, the fast, picosecond-scale and the integrated, millisecond-scale response are each measured with THz polarization and thus THz bias along the channel as well as perpendicular to the channel. The Dyakonov-Shur mechanism rectifies only a THz current along the channel. Simulations predict a response with a time constant $< 2\,\mathrm{ps}$ for the mobilities of the FETs used in this thesis [84]. Contributions from a polarization perpendicular to the channel can arise from incoupling to the FET through wiring acting as an antenna and feeding a THz bias to the FET. The 2D scans are performed from the lens side at 3.9 THz, with a factor 3.6 enhanced resolution due to the smaller beam waist of 0.2 mm in the substrate ($n = 3.6$) and the factor 12 magnification through the lens. Further 2D scans are measured from the air side in the range from 3.9 THz up to 30 THz with a spatial resolution of 0.6 mm and 0.1 mm, respectively. They allow to compare the generation of the THz induced biases in the different samples in an extreme frequency range from the THz band up to the MIR. At 3.9 THz the signal is expected to be clearly dominated by Dyakonov-Shur-like rectification, while other, e.g. thermoelectric effects may contribute significantly at 30 THz, due to the f^{-2} roll-off of the Dyakonov-Shur-like rectification (cf. chapter 3.4).

The oscilloscope measurements are referenced to the THz peak power P_{THz} and scaled with the $50\,\Omega$ impedance, as well as with the amplitude suppression η_a as $\mathcal{R}_I^{sc} = U_{det}/[50\,\Omega \cdot P_{THz}\eta_a]$. For each point, a time trace is measured and the maximum and minimum saved, to obtain the peak-to-peak amplitude. For quantitative comparability, the measured current of the lock-in amplifier is referenced to the average power as $\mathcal{R}_I^{li} = I_{det}/\bar{P}_{THz}$. The polarization is turned by 90° by using additional mirrors that may potentially introduce a slight shift of the beam position on the sample, as discussed for the measurements at 30 THz.

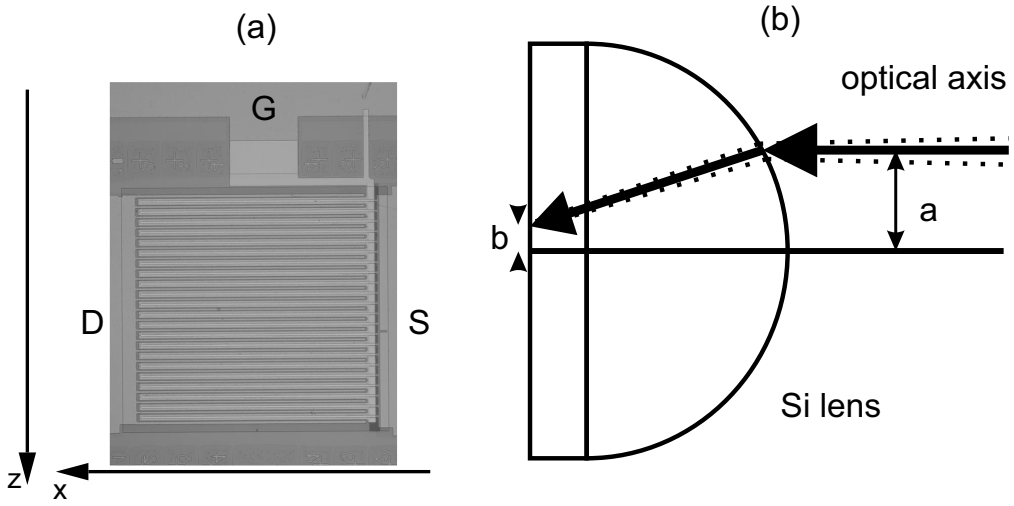

Fig. 7.3: *a) Microscope image of LA-FET device LAS-B. The drain pad is to the left, the source pad to the right, and the gate pad at the top of the* $0.3 \times 0.3\,mm^2$ *active area. The image is turned to correspond to the 2D beam scans in Fig. 7.4. b) Scheme for 2D scan of a LA-FET coupling through the substrate with an attached silicon lens. b) adapted from [86].*

7.2.1. 2D scans from the lens side

It is difficult to estimate the power coupled to lumped element devices without antennas that are much smaller than the THz wavelength [46; 86; 94; 95]. Often a significant amount of THz power is coupled to the actual device by bond wires. As a result, the power coupled to the lumped element FET is overestimated. The concept of LA-FETs with an active area much larger than beam waist effectively solves this problem. Scanning the active area with a much smaller THz focus allows to quantify the contributions of coupling THz radiation to the FET and to discriminate the response of the active area to that caused by undesired incoupling through bond wires. Fig. 7.3 shows a scheme of the 2D scan of the FET through the silicon lens. The LA-FET device LAS-B (depicted in Fig. 7.3a)) is mounted on the backside of a hyper-hemispherical silicon lens with a diameter of 10 mm. The source and drain pads are situated right and left of the active area, respectively, each with a size of $0.35 \times 0.25\,\mathrm{mm}^2$. The $0.13 \times 0.5\,\mathrm{mm}^2$ gate pad is connected with an on-chip connection at the top. The total hyper-hemisquerical offset from the center of the half sphere to the FET is 1.5 mm (scheme shown in Fig. 7.3b)). The silicon lens magnifies the dimensions of the $0.3 \times 0.3\,\mathrm{mm}^2$ active area of the LA-FET by a factor $a : b \approx 12$. The THz beam therefore has to raster an area in the range of $4 \times 4\,\mathrm{mm}^2$ to cover the whole active area.

Fig. 7.4 shows the rectified signal of the 2D scans in 0.25 mm steps for both polarizations along and perpendicular to the channel measured both with a lock-in amplifier and with a 30 GHz oscilloscope. The 30 GHz oscilloscope captures only the fast parts of the signal (cf. Fig. 7.4c) and Fig. 7.4d)), while the lock-in amplifier also

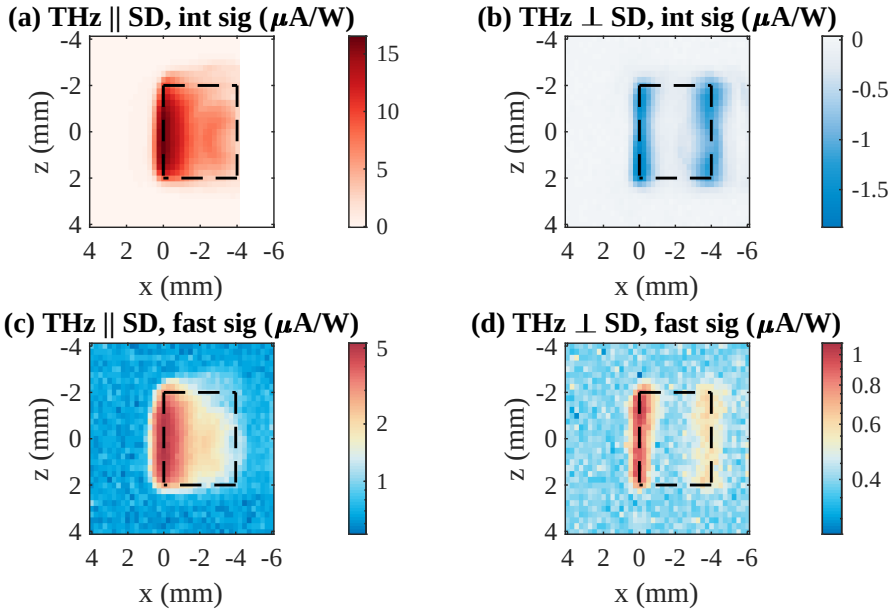

Fig. 7.4: *2D scan of device LAS-B at* 3.9 *THz magnified with a silicon lens to* $4.5 \times 4.8\,mm^2$. *a) Integrated response of THz polarization along SD direction. b) Integrated response of THz polarization perpendicular to SD direction. c) Fast response of THz polarization along SD direction. d) Fast response of THz polarization perpendicular to SD direction. The dashed square indicates the magnified* $0.3 \times 0.3\,mm^2$ *active area. The two stripes in b) and d) represent the boundary between the active area and the source and drain pad, respectively (cf. Fig. 7.3a)). a),b) adapted from [86].*

detects slow contributions (cf. Fig. 7.4a) and Fig. 7.4b)).

Fig. 7.4a) and Fig. 7.4c) show the measurements with a polarization along the SD direction, where Dyakonov-Shur-like FET rectification in the active area is expected. The device shows response in an area of $4.5 \times 4.8\,\mathrm{mm}^2$. This gives a non-magnified response area of about $0.38 \times 0.4\,\mathrm{mm}^2$ [86]. The measured response area agrees well with the expectation from the convolution of the device with the THz beam, that features a diffraction-limited beam waist of 0.2 mm for the experimental setup. The signal measured with the lock-in amplifier is about a factor 3 larger compared to the signal from the oscilloscope, thus there are additional slow components. The zero position corresponds to the center of the lens to the THz beam, aligned with a visible laser collinear to the THz beam. The shift in x direction of the actual image vs the alignment can be attributed to a 0.15 mm misalignment of the LA-FET in x direction on the backside of the lens. This misalignment also causes a larger beam waist and lower resolution on the right side of the images, as well as an increased response on the left side.

Fig. 7.4b) and Fig. 7.4d) show the measurements with a polarization perpendicular to the channel. For both, the lock-in and the oscilloscope measurements, two stripes

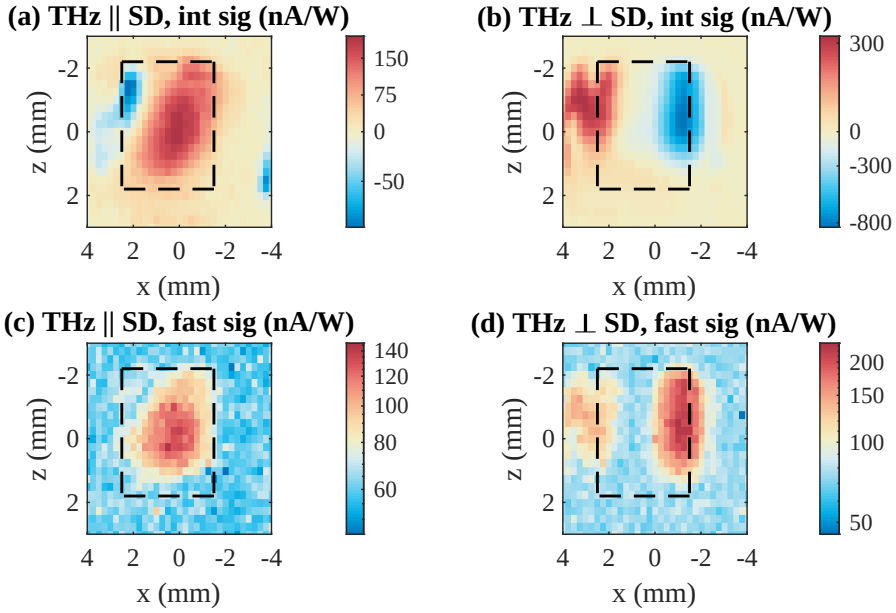

Fig. 7.5: *2D scan of gate-less device NG-A from silicon lens at* 3.9 *THz. a) Integrated response of THz polarization along SD direction. b) Integrated response of THz polarization perpendicular to SD direction. c) Fast response of THz polarization along SD direction. d) Fast response of THz polarization perpendicular to SD direction. The dashed square indicates the magnified* $0.3 \times 0.3\,mm^2$ *active area.*

with a response along the z direction are visible. This corresponds to a response from the boundary between the active area and the source and drain pads on the left and right (cf. Fig. 7.3a)). There is no response from the active area of the FET. There is further no response with the THz beam positioned on the gate pad. The signal with the polarization perpendicular to the channel is suppressed by a factor 9 (factor 5), for the lock-in (oscilloscope) measurement. The lock-in measurement shows a different sign for the rectified current. The oscilloscope measurement only depicts the peak-to-peak amplitude of the signal.

Further, the fast and integrated 2D response of device NG-A without Schottky contact is shown in Fig. 7.5. As there is no clear pulse structure of device NG-A with a single main peak, the measured impulse response of device LAS-B is used for the calculation of the amplitude suppression η_a (cf. Fig. 7.2b)). The four 2D beam scans show a 3.75 mm long area with response in z direction, corresponding to a length of 0.3 mm on the chip. The integrated response with polarization along the channel is a slightly tilted stripe with a width of 3.25 mm at the bottom. On the top left, the integrated response features a signal with opposite sign. The signal at the very bottom right corresponds to a position outside, coupling from a partial reflection of the THz beam on the metal case of the package. For this device without Schottky contact, the gate pad on the top is not connected to the active area. The fast response with a polarization along the channel appears more focused in the

image, due to a smaller dynamic range of the measurement (cf. Fig. 7.5d)). At the position of the two spots in the lock-in measurement with negative signal, there is no signal with the oscilloscope.

The fast response and the integrated response with a polarization perpendicular to the channel show two parallel stripes at the edge between the active area and the drain and source pads on the right and left side. Between the two stripes, there is no signal. The integrated response from the lock-in measurement gives an opposite sign for incoupling through the boundary of the left and right pad. For both measurements, the right pad shows about a factor 2 larger absolute response. This difference is unexpected, as both source and drain contacts are symmetrical with respect to the channel. The ohmic source and drain contacts were also metalized and annealed in the same processing step. Therefore the imperfection of the ohmic contacts should be similar. The only difference is a slightly larger distance of the drain contacts from the ohmic contacts on the right of 18 μm, compared to 8 μm on the left. The distance on the right is close to $\lambda/2$ for 3.9 THz, therefore the structure acts as an antenna enhancing the incoupling, while the distance on the left is much shorter than $\lambda/2$.

The positive signal from the lock-in measurement and the oscilloscope measurement compare well for the polarization along the channel. There is thus no strong additional temporally slow signal that cannot be detected with the oscilloscope. For the polarization perpendicular to the channel, the absolute response is a factor of 3 smaller.

The results show that the LA-FET is able to cover the full beam waist [86]. The 2D scans show that the signal from direct irradiation of the active area with the polarization perpendicular to the FET channel is suppressed compared with the polarization along the FET channel. Coupling the THz to the gate pad on the top does not give a rectified THz signal on the SD read-out. The wiring from the gate pad to the active area is fairly long ($\approx 100\,\mu$m), such that the radiative loss at 3.9 THz is high [86]. There is no off-axis contribution, therefore elements such as wiring other than the active area and boundary to the gate and drain pads do not couple THz radiation to the FET. It can be concluded, that the majority of the detected signal originates from the rectification of THz radiation along the channel. At the boundary between source and drain pad and the active area, the THz radiation couples to the FET with a polarization perpendicular to the FET channel. This proves that the pads act as antennas for a perpendicular polarization, while the active area does not show any noteworthy response.

The fast response of the reference sample shows that the fast response of the LA-FET has only a negligible contribution from a gate-less detection mechanism, such as the imperfections of SD contacts. Only for the integrated response perpendicular to the channel, the reference sample without gate shows about half the response compared to the LA-FET device. In conclusion, the measured response is compatible with a Dyakonov-Shur-like rectification mechanism in the FET at 3.9 THz. Other contributions are marginal.

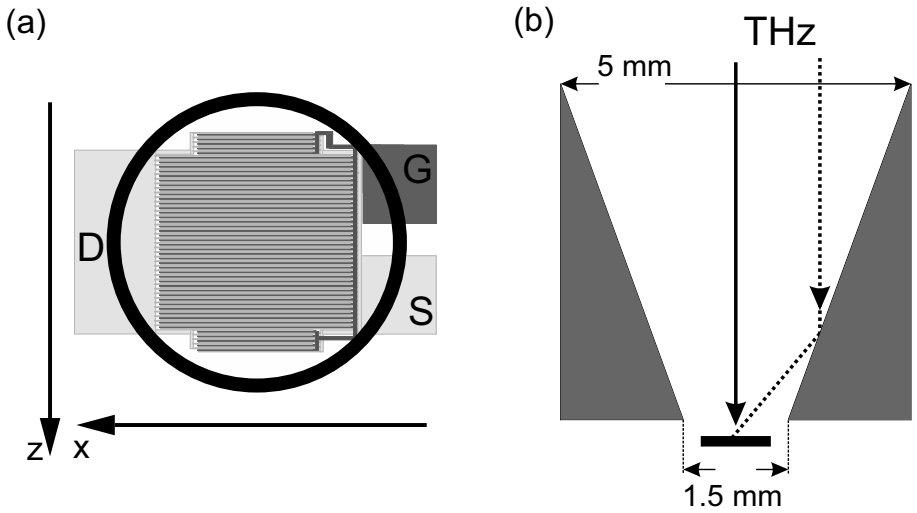

Fig. 7.6: *a) Schematic for 2D scan of device LA-E from air side with* 1.5 *mm cone aperture (black circle). The THz beam scans the LA-FET device. The* 1.5 *mm cone aperture shields the wiring and contact pads in order to prevent undesired incoupling. b) The cone aperture with* 5 *mm maximum opening reflects beams in a diameter of* 2.4 *mm around the center onto the center of the LA-FET.*

7.2.2. 2D scans from the air side

Fig. 7.6a) shows the layout of device LA-E with the 1.5 mm aperture for the lateral 2D scans. The scheme is oriented to correspond to the 2D scans of the $1 \times 1\,\mathrm{mm}^2$ LA-FET devices, such as device LA-E in Fig. 7.7 at 3.9 THz, Fig. 7.9 at 11.8 THz, and Fig. 7.11 at 30 THz. Fig. 7.6b) shows the reflection of THz beams from the 1.5 mm cone aperture onto the LA-FET. In a diameter between 1.6 mm and 3.2 mm around the center of the LA-FET, the beam is directly reflected onto the LA-FET for the dimensions of the cone aperture. Device LAS-A with a $0.3 \times 0.3\,\mathrm{mm}^2$ active area is packaged with a 0.5 mm cone aperture.

Response at 3.9 THz

Fig. 7.7 shows both the integrated and fast THz induced signal at 3.9 THz in 0.2 mm steps, each for a polarization along and perpendicular to the channel. At 3.9 THz, the diffraction-limited beam waist on the sample for the experimental setup calculates to 0.6 mm. All four measurements show a response of device LA-E in a circular area with about 3 mm diameter. The response outside of the 1.5 mm cone aperture and $1 \times 1\,\mathrm{mm}^2$ aperture can be attributed to reflection of the THz beam from the cone aperture onto the LA-FET as shown in Fig. 7.6b). Fig. 7.7a) shows the integrated response to 3.9 THz pulses with a polarization along the channel. The LA-FET shows a response in the center of the setup of a circle of 1 mm diameter, where the response from the active area is expected. The area with highest response is only slightly shifted along the z axis. In a 3 mm diameter around the center, the

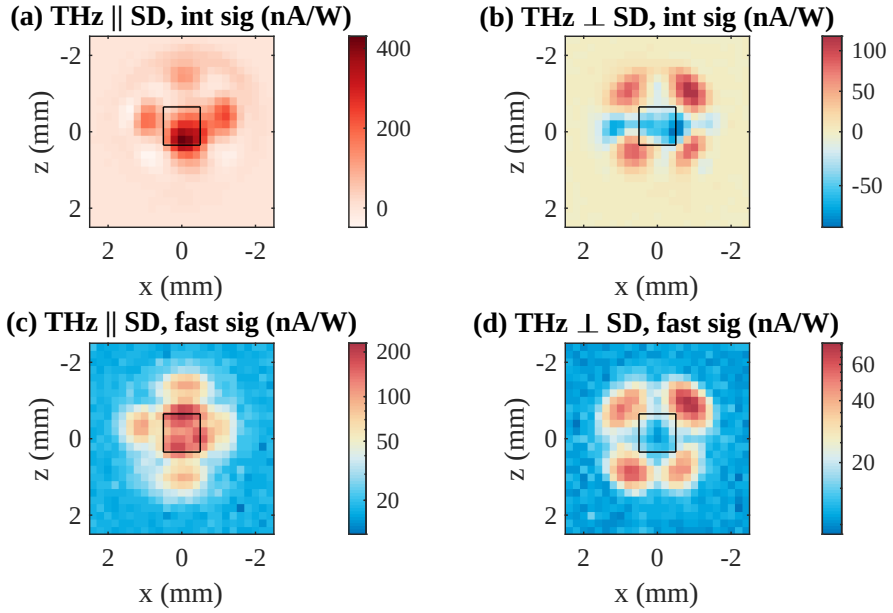

Fig. 7.7: *2D scan of LA-FET device LA-E at* 3.9 *THz. a) Integrated response of THz polarization along SD direction. b) Integrated response of THz polarization perpendicular to SD direction. c) Fast response of THz polarization along SD direction. d) Fast response of THz polarization perpendicular to SD direction. A* $1 \times 1\,mm^2$ *black square indicates the position of the active area.*

integrated response features areas with positive and negative sign. Fig. 7.7c) shows the fast signal components for a polarization along the FET channel. The response is centered in an area of about $1.2 \times 1.2\,\mathrm{mm}^2$ corresponding to the active area of the LA-FET convoluted with the THz beam waist. The integrated response in the center is a factor 2 higher compared to the fast response. The central responsive area is surrounded by a cross-like structure along the z and x direction. The cross originates from reflections from the cone onto the active area of the LA-FET. Fig. 7.7b) shows the integrated signal components for the polarization perpendicular to the channel. The signal originating from the active area in the center is negative in agreement with the findings for illumination from the lens side in Fig. 7.4b). The response shows four spots in a 3 mm diameter with positive signal in diagonal directions to the x and z direction outside of the active area of the LA-FET, that originate from reflections on the cone aperture. The reflection of the cone aperture under an angle of 45° rotates the THz polarization by 90°. Therefore, the signal arriving at the active area is polarized along the channel and induces a Dyakonov-Shur-like rectification. It should be noted that reflections under 45° in Fig. 7.9a) (THz||SD) cause a slightly negative signal, as the polarization is rotated to be perpendicular to the channel. Fig. 7.7d) shows the fast signal components for a polarization perpendicular to the channel. The fast response is about the same as the integrated response, except for the central area of the LA-FET and the cross area not showing a fast response to

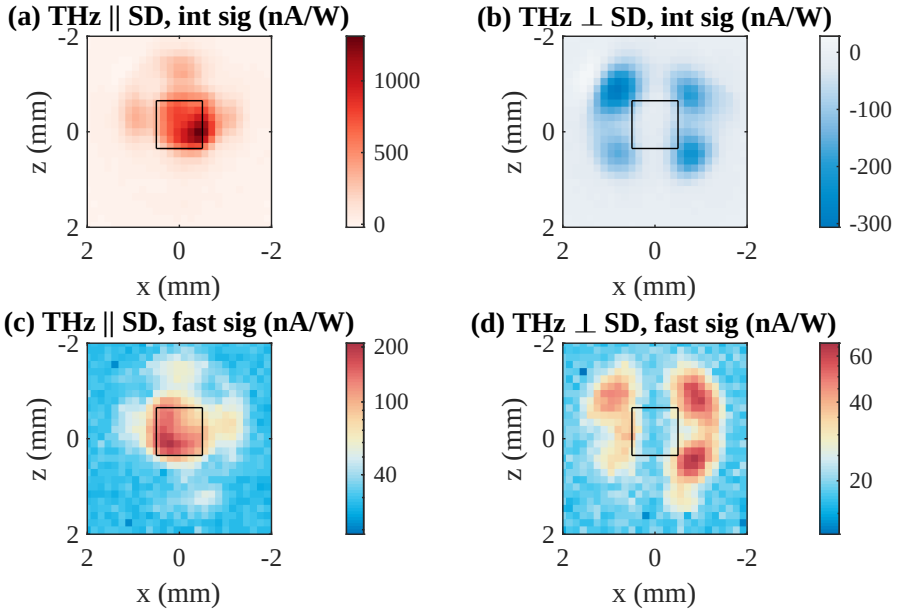

Fig. 7.8: *2D scan of LA-FET device LAS-E at 3.9 THz. a) Integrated response of THz polarization along SD direction. b) Integrated response of THz polarization perpendicular to SD direction. c) Fast response of THz polarization along SD direction. d) Fast response of THz polarization perpendicular to SD direction. A* $1 \times 1\,mm^2$ *black square indicates the position of the active area.*

the THz beam.

These findings prove that the FET predominantly responds to signals polarized parallel to the channel as expected for Dyakonov-Shur-like rectification.

Fig. 7.8 shows the fast and integrated 2D response of LA-FET LAS-E with strong gate-source coupling at 3.9 THz. Device LAS-E is mounted in the same direction to the THz beam as LA-E with similar active area, only the design of the individual FETs includes a strong AC gate-source coupling (cf. Fig. 7.6). The integrated and the fast measurements show a response in the center in an area of $1.2 \times 1.2\,\mathrm{mm}^2$, that can be assigned to direct irradiation of the active area (cf. Fig. 7.8a) and Fig. 7.8c)). The integrated response is a factor 6 larger, and has a different position than the peak response. The response in a 3 mm diameter around the center can be attributed to a reflection on the cone aperture.

Turning the polarization by 90° perpendicular to the channel, there is only an order of magnitude lower integrated response from the $1 \times 1\,\mathrm{mm}^2$ active area. In a 3 mm diameter, along the diagonal directions, there is a strong negative response, due to rotation of the polarization through a reflection on the aperture. The fast response shows a pattern similar to the negative part of the integrated response. It is a factor 5 smaller compared to the integrated response. The response from device LAS-E is thus similar to the response of device LA-E without strong gate-source coupling at 3.9 THz. In comparison to device LA-E, the integrated response of device

LAS-E with strong gate-source coupling is larger, while the fast response is on the same level.

In conclusion, the measurements of the LA-FETs LA-E and LAS-E at 3.9 THz are compatible with a fast plasmonic (Dyakonov-Shur-like) rectification mechanism in the FET underneath the gate. The higher integrated response can be accounted to an additional slow mechanism.

Response at 11.8 THz

Further 2D scans are performed at 11.8 THz at the transition from the THz band (0.1 - 10 THz) to the MIR, to obtain the characteristics of the underlying detection mechanism with the $1 \times 1\,\mathrm{mm}^2$ device LA-E without strong gate-source coupling and the $0.3 \times 0.3\,\mathrm{mm}^2$ device LAS-A with strong gate-source coupling. The diffraction-limited beam waist calculates to 0.2 mm. The three times smaller beam waist enables a higher resolution of the images from the 2D scan compared with 3.9 THz.

The integrated response of device LA-E is in a circular structure with both positive and negative sign around the center, due to the reflection from the cone aperture (cf. Fig. 7.9a)). In the center, there is a positive response in an $1 \times 1\,\mathrm{mm}^2$ area, that can be accounted to detection on the active area. Right above the central area, there is a response with negative sign, that can be accounted to partial reflection of the THz beam from the cone aperture onto the LA-FET. The fast response in Fig. 7.9c) in the central $1 \times 1\,\mathrm{mm}^2$ area agrees well to the integrated measurement from the direct irradiation of the active area. In a circular shape around the center, there is a response that can be assigned to the reflection in the cone aperture similar for fast and integrated response. Both the integrated response and the fast response in the center feature a maximum for $z < 0$ and $z > 0$ along the x direction (cf. Fig. 7.9a) and Fig. 7.9c)). Instead, a distribution with a maximum response in the center at $z = 0$ of the $1 \times 1\,\mathrm{mm}^2$ active area would be expected. This distribution suggests a non-uniform response of the active area of device LA-E. The 1.5 mm cone aperture is significantly larger than the beam waist, such that a strong diffraction behavior is not to be expected. On the top and bottom of the LA-FET, there are also no pads, or other wiring connected to the active area (cf. Fig. 7.6). The magnitude of the integrated and fast signal agree well, such that the response can be accounted to a fast detection mechanism.

Next, the polarization is turned by 90° perpendicular to the FET channel. The lock-in measurement shows an integrated response from the $1 \times 1\,\mathrm{mm}^2$ active area, as well as from reflections from the aperture (cf. Fig. 7.9b)). In contrast to measurements at 3.9 THz, the active area responds to both polarizations in the same manner. However, there is no fast response from direct irradiation of the active area, only through reflections from the aperture along the diagonal directions in the same manner as measurements at 3.9 THz (cf. Fig. 7.9d)). The THz polarization perpendicular to the channel results in a far smaller fast response compared to the polarization along the channel. The fast response agrees well with the expectations for a rectification of THz along the channel. The integrated response in the center includes thus an

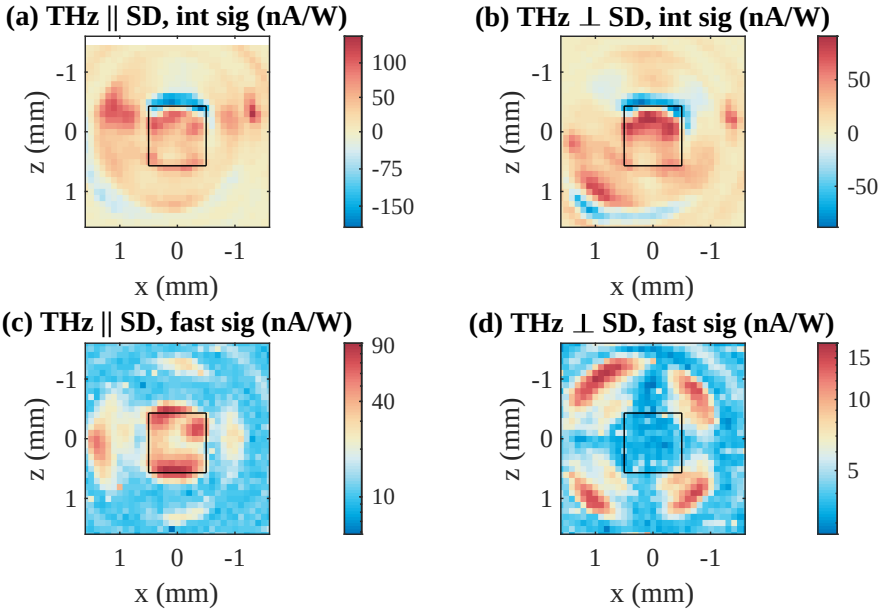

Fig. 7.9: *2D scan of LA-FET device LA-E at* 11.8 *THz. a) Integrated response of THz polarization along SD direction. b) Integrated response of THz polarization perpendicular to SD direction. c) Fast response of THz polarization along SD direction. d) Fast response of THz polarization perpendicular to SD direction. A* $1 \times 1\,mm^2$ *black square indicates the position of the active area.*

additional, slow detection mechanism, such as a thermal process. The integrated signal is also a factor 4 larger compared to the fast signal. The fast response at 3.9 THz shows a similar structure, however not as pronounced as at 11.8 THz and not for the integrated response.

Fig. 7.10 shows the 2D response of the $0.3 \times 0.3\,\mathrm{mm}^2$ device LAS-A with strong gate-source coupling. Device LAS-A has a smaller active area compared to the $1 \times 1\,\mathrm{mm}^2$ device LAS-E and features a cone aperture with 0.5 mm inner diameter (3.6 mm outer diameter). It is also irradiated from the air side, comparable to the scheme in Fig. 7.6b). The measured 2D scans are oriented to correspond to the layout of the $0.3 \times 0.3\,\mathrm{mm}^2$ active area and pads shown in Fig. 7.3a). The fast response is centered in a circle with 0.4 mm diameter, that can be accounted to the direct irradiation of the active area (cf. Fig. 7.10c)). The integrated signal shows a similar distribution with an additional area with negative signal (cf. Fig. 7.10a)). The additional signal of the integrated response is accounted to a reflection on the cone aperture and close to the position of the boundary to the source pad. The integrated response from the lock-in measurement is a factor 4 larger compared to the fast response from the oscilloscope measurement. The $0.3 \times 0.3\,\mathrm{mm}^2$ black square is located at the very same x and z coordinates.

Turning the polarization by 90°, the integrated response for direct irradiation of the active area in the center decreases by a factor 7, while the fast response is only

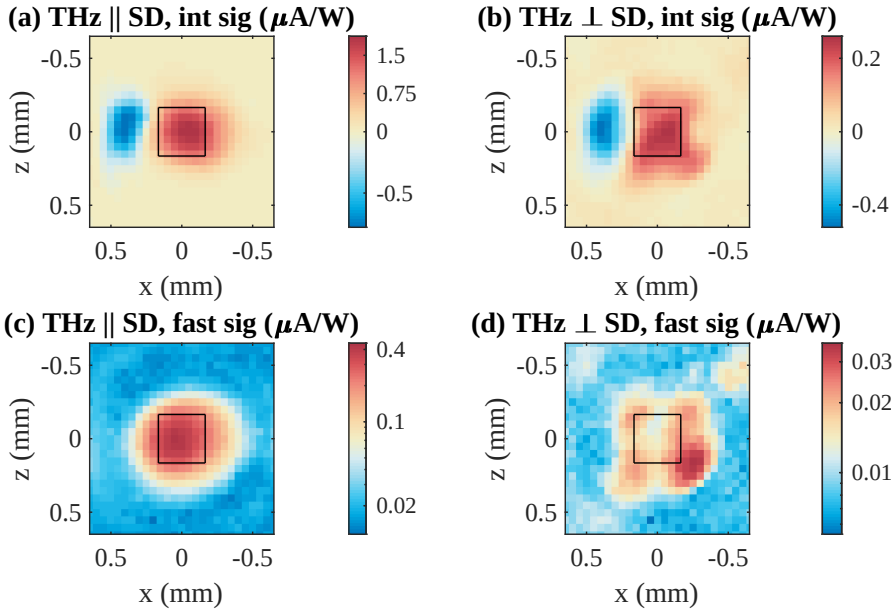

Fig. 7.10: *2D scan of* $0.3 \times 0.3\,mm^2$ *LA-FET device LAS-A at* 11.8 *THz from the air side. a) Integrated response of THz polarization along SD direction. b) Integrated response of THz polarization perpendicular to SD direction. c) Fast response of THz polarization along SD direction. d) Fast response of THz polarization perpendicular to SD direction. A* $0.3 \times 0.3\,mm^2$ *black square indicates the position of the active area.*

slightly above the noise level of the oscilloscope. The integrated response shows a similar negative signal on the right as for the polarization along the channel. The fast response shows a stronger signal through the reflection of the THz beam on the cone aperture under 45° in agreement with previous measurements. The fast signal is a factor 7 smaller compared to the integrated signal.

The measured fast response at 11.8 THz is compatible with a plasmonic rectification mechanism. However, compared to 3.9 THz, a larger part of the integrated signal originates from slow components, not included in the fast oscilloscope measurement. The lock-in measurements show fairly similar patterns for both polarizations although the absolute response is still about a factor 3-5 stronger for the polarization along the SD direction.

Response at 30 THz

At last, the 2D scans are performed at 30 THz in the MIR for LA-FET device LA-E and the reference device NG-B without Schottky contacts. The beam waist calculates to $\lesssim 0.1$ mm.

The integrated response of device LA-E has a similar, slightly shifted shape for the polarizations along and the polarization perpendicular to the channel (cf. Fig. 7.11a)

and Fig. 7.11b)). The shift is accounted to a slight shift of the beam along the x axis at 30 THz, when turning the polarization by 90° with additional mirrors.

There is no strong signal from the center of the active area, but from the bottom edge of the active area and the aperture for both polarizations. The fast response is within an $1 \times 1\,\mathrm{mm}^2$ area, distributed similar to the response for direct irradiation of the active area at 11.8 THz. This response can also be assigned to the active area (cf. Fig. 7.11c)). The fast response peaking within the active area is a factor ≈ 5 weaker compared to the integrated response peaking outside of the active area. Only left of the center there is a small signal above the noise level, from a reflection from the aperture onto the LA-FET. No fast signal above the oscilloscope's noise floor was found for the polarization perpendicular to the channel with the available power.

It can be concluded, that the integrated response at 30 THz is dominated by a slow detection mechanism, superposing a fast detection mechanism. The measured fast response at 30 THz agrees with a plasmonic (Dyakonov-Shur-like) rectification mechanism, however, with a much lower responsivity. The 1.6 (2.4) times larger average power for the measurement with device LA-E at 30 THz as compared to 11.8 THz (3.9 THz) suggests stronger thermal modulation, giving rise to thermal effects. In the (Al)GaAs semiconductor, the charge carrier density $n^{(2D)}$ and the mobility μ, depend on the semiconductor temperature. Therefore, the polarization-insensitive integrated response suggests a bolometric detection mechanism.

Additionally, sample NG-B without Schottky contact is characterized to quantify the contribution from the imperfection of ohmic contacts and unknown rectification processes in the response of the FET devices. The fast response was below the oscilloscope's noise level for the available power and could thus not be measured. Fig. 7.12 shows the integrated response, measured with the lock-in amplifier. For both polarizations, in the center two 1 mm long parallel stripes separated by 1 mm are present. This corresponds to the boundary between the $1 \times 1\,\mathrm{mm}^2$ active area and the drain and source pad. Around the active area, there is a circular structure in the response, caused by reflection of the MIR beam onto the device.

The integrated response of device NG-B has a similar magnitude compared to LA-FET device LA-E (cf. Fig. 7.11). Therefore it can be concluded, that the integrated response from device LA-E at 30 THz has a strong contribution from a detection mechanism other than plasmonic rectification in the FET channel. The higher thermal average power causes a slow signal induced by MIR radiation. However, the fast LA-FET response to THz radiation along the channel centered in the $1 \times 1\,\mathrm{mm}^2$ active area can be attributed to a detection mechanism including a gate electrode. The measurements are thus compatible with a fast Dyankonov-Shur rectification mechanism at 30 THz.

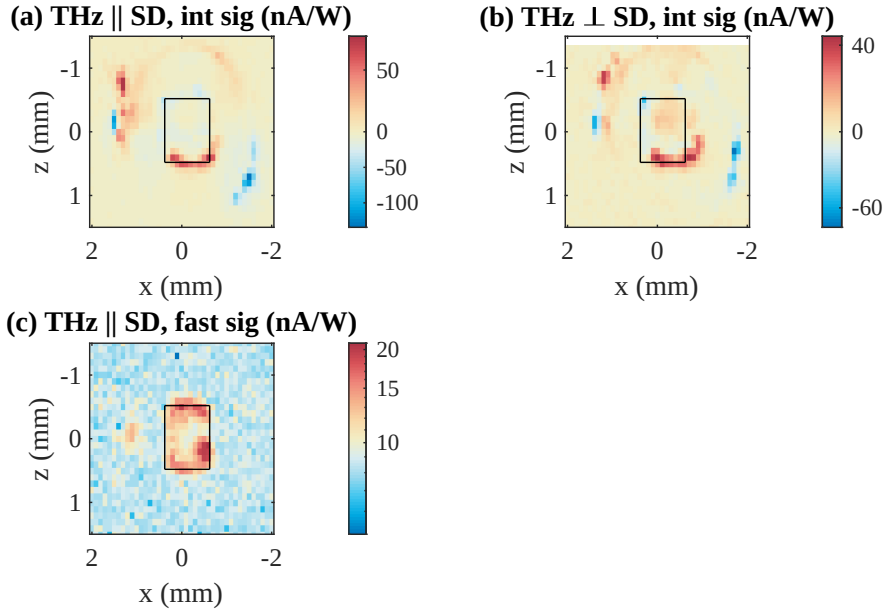

Fig. 7.11: *2D scan of LA-FET device LA-E at 30 THz. a) Integrated response of MIR polarization along SD direction. b) Integrated response of MIR polarization perpendicular to SD direction. c) Fast response of MIR polarization along SD direction. For the polarization perpendicular to SD, the fast response is below the noise level of the oscilloscope. A* $1 \times 1\,mm^2$ *black square indicates the position of the active area.*

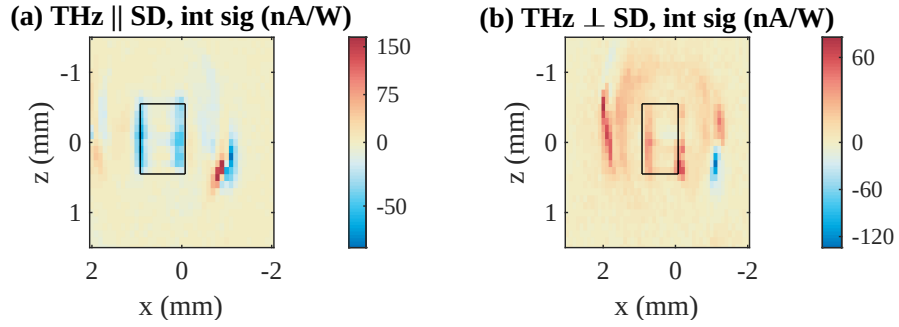

Fig. 7.12: *2D scan of reference device NG-B at 30 THz. a) Integrated response of MIR polarization along SD direction. b) Integrated response of MIR polarization perpendicular to SD direction. The fast response is below the noise level of the oscilloscope. A* $1 \times 1\,mm^2$ *black square indicates the position of the active area.*

8. Temporal response and measurement of temporal pulse shapes

The preceding chapters aimed for obtaining a detailed understanding of the rectification process in LA-FETs and A-FETs. This chapter shows a concrete application of FETs by determining the FEL pulse shape that is altered by tuning of the cavity length. Knowledge of the pulse shape at the experimental site is of utmost importance for a variety of experiments probing physics on the picoscecond-scale. The pulse shapes measured in time domain with A-FET device AN-B and LA-FET device LA-E are compared to the pulse shapes determined with a grating spectrometer in the frequency domain. Further, the refined ansatz introduced in chapter 4 is used for evaluation of the measured time traces and spectra and compared to the state-of-the-art ansatz. The results of this study were published in ref. [30]. The amplitude suppression η_a through the IF-limitation is measured experimentally and compared to the theoretical expectation, which is outlined in chapter 4.3 [85].

A FEL cavity fits a large number of THz wavelengths, therefore the cavity detuning is often only measured relatively instead of an absolute length measurement with a required precision in the range of $0.1\,\lambda$. The relative cavity detuning $\Delta L'$ is defined as $\Delta L = \Delta L' + L_0$ with an offset L_0. The offset L_0 can be obtained from the linear relation between the exponential broadening and the relative cavity detuning [31]

$$\tau = \frac{2}{\alpha c}(-\Delta L') - \frac{2}{\alpha c} L_0. \tag{8.1}$$

Pulses generated by FELBE with a cavity detuning in the range of $\Delta L' = -2.0 \ldots 0\,\lambda$ were used for this study.

Care is taken to minimize RF losses in the IF path. The drain pad of the FET is connected with about 1 mm long bond wires to a SMA connector (cf. Fig. 5.3). The IF path continues with a high quality coaxial cable with 3.5 mm connectors (Junflon MWX221, 3 dB attenuation at 26.5 GHz), and a large bandwidth (40 GHz) bias-tee (picosecond 5542) to the 30 GHz oscilloscope. The distance of the FEL pulse traveled in air to the FET is about 3.3 m (cf. Fig. 6.2a)).

8.1. Impulse response function

The impulse response function $IF_{eff}(t)$ for both devices is measured with a pulse much shorter than the rise time of the oscilloscope. The 30 GHz oscilloscope features an impulse response with a Gaussian width of $\sigma_{scope} = 7\,\text{ps}$, obtained by fitting the rise time given in the data sheet to a Gaussian behavior. The FELBE pulses at 11.8 THz feature a Gaussian pulse width of $\sigma_s = 2\,\text{ps}$. The pulse width is calculated from the measured spectrum of the FEL pulses, as indicated with the index "s". The measured pulse widths are therefore dominated by the IF limitations, as the pulse width is much shorter than the theoretical limitation from the oscilloscope. Fig. 8.1 shows the measured impulse response function. The first measured pulse

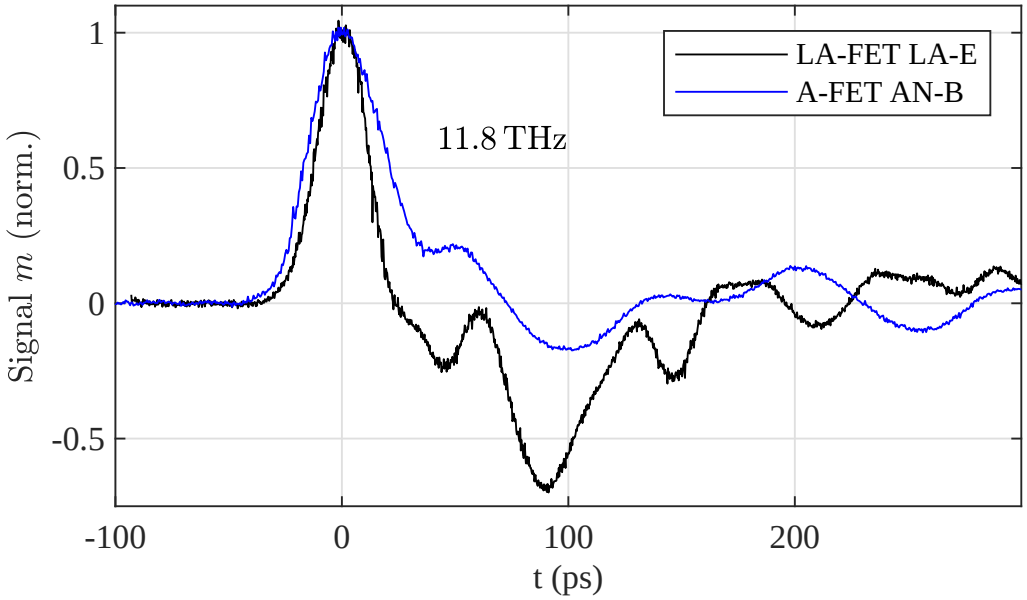

Fig. 8.1: *Measured impulse response of the LA-FET device LA-E and the A-FET device AN-B. The Gaussian pulse widths are* 11 *and* 14 ps *measured at a gate bias of* $U_{GS} = -0.5\,\mathrm{V}$ *and* $-0.3\,\mathrm{V}$*, respectively. The* 11.8 *THz pulse features a Gaussian pulse width of* $\sigma_s = 2\,ps$*. Adapted from [30]* ©*IEEE 2019.*

features a Gaussian shape, in very good approximation, with a Gaussian width of $\sigma_m = 11.4 \pm 0.3\,\mathrm{ps}$ ($\sigma_m = 14.2 \pm 0.3\,\mathrm{ps}$) for the main peak of the LA-FET (A-FET), corresponding to a FWHM of 27 ps (33 ps) [30]. The measured pulse width agrees to previous measurements at 22 THz with device LA-E, where a Gaussian width of $10.0 \pm 0.3\,\mathrm{ps}$, i.e. a FWHM of 24 ps was recorded with a slightly different IF path (responsivity shown in Fig. 6.3)[28].

The measured pulse $p(t)$ is the convolution of the initial pulse $p(t)$ with the rectification process $r(t)$ and the IF limitations $IF(t)$ that include the oscilloscope and the wiring in the IF path (cf. Eq. 4.9). From the difference of the measured Gaussian impulse response to the theoretical 7 ps Gaussian limitation of the 30 GHz oscilloscope, the upper limit of the rectification in the FETs $r(t)$ calculates to $\sigma_{r(t)} \lessapprox \sqrt{\sigma_m^2 - \sigma_{scope}^2} = 7.1\,\mathrm{ps}$. However, the 7.1 ps Gaussian upper limit still includes bond wires to the SMA connector, and the coaxial cable to the oscilloscope. Therefore, it can be assumed that the actual Gaussian time constant $\sigma_{r(t)}$ of $r(t)$ is smaller than 7.1 ps.

The ringing after the main pulse can be attributed to reflections and imperfections in the IF path e.g. by an impedance mismatch in the wiring. The amplitude of the reflections depends on the impedance of the FET, that can be changed by a gate bias. This dependence is discussed later together with the dependence of the pulse width from the gate bias. These reflections influence the fitted pulse width only a few 10 ps after the main peak. The rising edge and the first few 10 ps, where the amplitude drops to 80% after the main peak are considered reflection-free and are

used for the fit of $m(t)$ with Eq. 4.10.

The measured Gaussian impulse response $IF_{eff}(t)$ allows to include the limitations from the IF path in the Gaussian width of the convolution model for the FEL pulse shape (cf. Eq. 4.10).

Comparison with state-of-the-art detectors

The measured 24 ps FWHM impulse response corresponds to a 3 dB IF bandwidth of 13 GHz in frequency domain. It is determined from the whole IF path including the wiring, SMA connectors and the 30 GHz oscilloscope. Without the oscilloscope, but including the bond wires and coaxial cable, the 3 dB IF bandwidth bandwidth calculates to 19 GHz. The response of the LA-FET detector is thus faster compared to the published results with cryogenic YBCO detectors with a 30 ps FWHM at a 30 GHz oscilloscope [14]. The LA-FET also features a similar bandwidth compared with results of a 18 GHz bandwidth FET used for communication around 0.3 THz [19]. However, the results are still below the measured 16 ps FWHM using a 63 GHz oscilloscope connected to a cryogenic YBCO detector [15]. The measured impulse response of the LA-FET may be narrowed further, by using a faster oscilloscope, and an improved bonding to a coplanar waveguide to a type K connector instead of freestanding wires and an SMA connector, that is only specified up to 18 GHz.

8.2. THz pulse shape characterization

Eq. 4.10 and Eq. 4.8 excellently describe the measured time traces $m(t)$ and the intensity spectra $\hat{p}_s(f)$ measured with the grating spectrometer, respectively [30]. This is demonstrated with experiments as described in the following paragraphs. The 2.0 THz FEL pulses are generated with a relative cavity detuning from $\Delta L' = 0$ with a Gaussian shape to a strongly negative detuning with $\Delta L' = -2.0\,\lambda_0$ with an exponential rising edge. Only the intensity spectrum of the FEL pulses at $\Delta L' = 0$ features a shoulder, that is not described by Eq. 4.8, but the respective measured time domain pulses are described very well by Eq. 4.10 with a Gaussian shape and a vanishing exponential broadening $\tau_m \to 0$. A faint linear ($\propto f$) background is accounted for, when fitting of the intensity spectra to Eq. 4.8. The SNR of the measured intensity spectra is about an order magnitude lower than of the time traces, resulting in larger fit errors for the frequency domain.

The solid lines in Fig. 8.2a) are fits to Eq. 4.10 of the measured time traces $m(t)$, that are displayed as dots, with the Gaussian pulse width σ_m and the exponential pulse width τ_m. The ideal time domain pulses $p_s(t)$ (dashed lines) are calculated from spectroscopic data, assuming no chirp or selective absorption that would broaden the time domain pulse. The broadening of the measured pulses in comparison with the ideal time domain pulses is due to the limited IF bandwidth of the measurement. The respective intensity spectra (points) from the grating spectrometer measurement in Fig. 8.2b) are fitted with Eq. 4.8, giving the pulse shape parameters $\bar{\sigma}_s$ and $\bar{\tau}_s$,

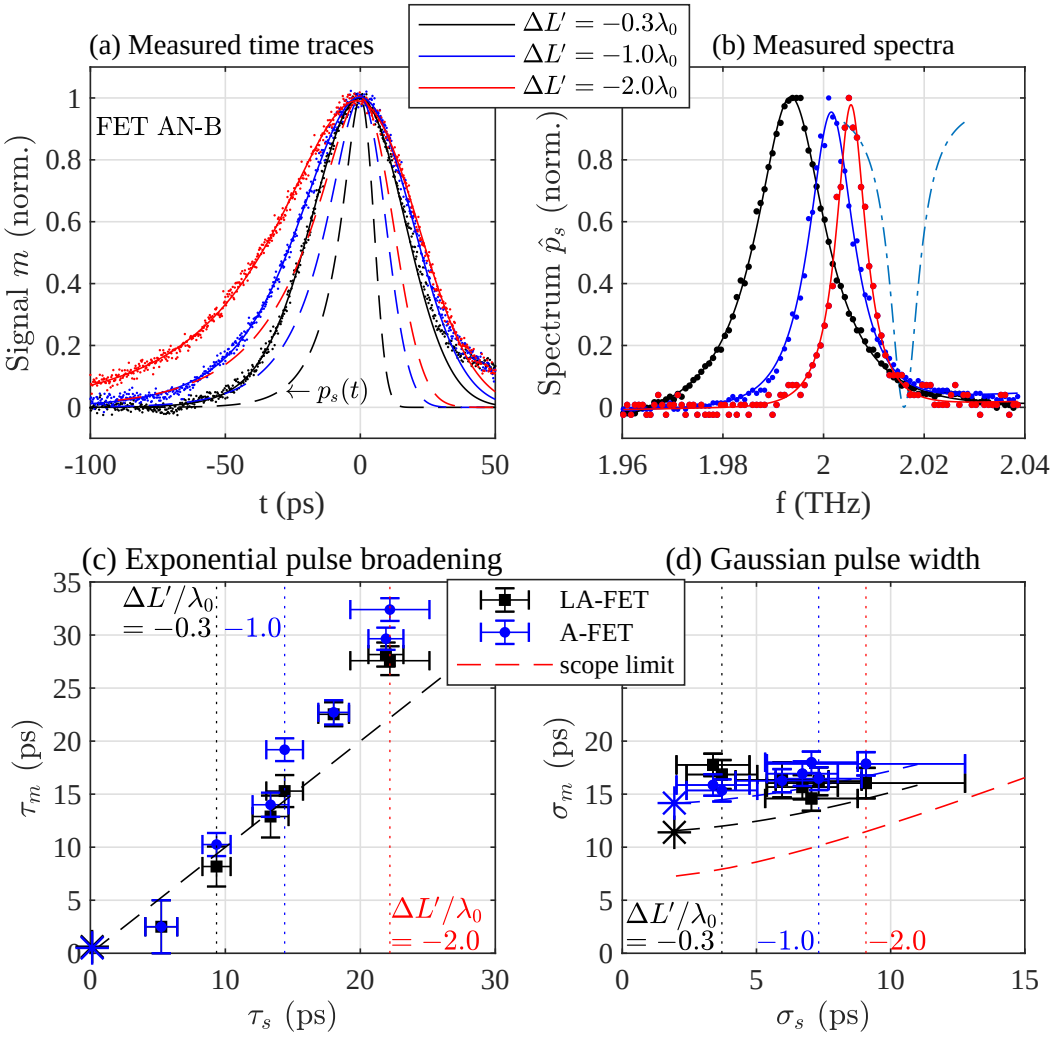

Fig. 8.2: *a) Detected 2.0 THz signal (dots) with the A-FET AN-B at $U_{GS} = 0$ V vs. time for three different FEL pulse shapes with different cavity detuning. The amplitude of the main peak is normalized and the time is set to $t = 0$ ps. The solid lines are fits to Eq. 4.10. The dashed lines are the ideal time domain pulses from fits to the measured spectra Eq. 4.8 in the respective color of the time domain data. b) Intensity spectra measured with the grating spectrometer of the respective THz pulses for three different FEL pulse shapes. The dashed dotted line (not to scale) indicates potential losses through a water vapor line for the time domain measurements carried out in air. c),d) Measured pulse widths for the LA-FET LA-E and the A-FET AN-B with $U_{GS} = 0$ V vs pulse width obtained from the spectrum $\hat{p}_s(f)$ at 2.0 THz. The star symbols display the Gaussian IF limitation (cf. Fig. 8.1). The fitted parameters τ_m and σ_m from a) and τ_s and σ_s from b) are marked with dotted lines in the same color. c) Exponential pulse width τ_m vs τ_s. d) Gaussian pulse width σ_m vs σ_s. The dashed lines represent the IF limitation for the LA-FET (black), the A-FET (blue) and the theoretical limit of the 30 GHz oscilloscope (red). Adapted from [30] ©IEEE 2019.*

that are converted to σ_s and τ_s for direct comparison to the time domain data (cf. Eq. 4.5).

Fig. 8.2c) shows the exponential pulse width τ_m from the time domain data of both LA-FET and A-FET vs the exponential width τ_s obtained from the intensity spectra for the FEL pulses with different cavity lengths. The dashed line is a guide to the eye for a perfect 1:1 correspondence. The measured exponential width τ_m shows only minor or no limitations through the IF limitations of the wiring and the oscilloscope $IF(t)$ and the rectification $r(t)$, as expected from the accuracy simulations (cf. chapter 4.3). The pulse widths from the measurement of the impulse response $IF_{eff}(t)$ from Fig. 8.1 are shown as overlapping star symbols. For large exponential rise times τ, i.e. pulses from a strongly negative detuned cavity ($\Delta L' \ll 0$), the exponential width from the spectrometer data τ_s is smaller compared to the exponential width τ_m from the time traces. This can be accounted to water vapor absorption. The time domain traces were measured in air, while the spectra were measured in a N_2 atmosphere (cf. Fig. 6.2a)). The THz pulses travel about 3.3 m in air after exiting the N_2 beam line, before they are rectified with the FET. At strongly negative cavity detuning (large τ_s), the spectrum shifts slightly towards a water line at 2.016 THz as shown in Fig. 8.2b). Therefore, pulses with long exponential rise times may experience absorption and thus temporal broadening that manifests in increased exponential rise times.

Fig. 8.2d) shows the Gaussian width σ_m from the time domain FET data vs Gaussian width σ_s determined from the frequency domain spectrometer measurements. The star symbols display the measured impulse response function at 11.8 THz. The dashed lines display the theoretical expectation $\sigma_m = \sqrt{\sigma_s^2 + \sigma_{IF,eff}^2}$ for the broadening of the Gaussian FEL pulse width σ_s with the measured impulse response function $\sigma_{IF,eff}$ of the LA-FET and A-FET, respectively. The red dashed line represents the limit due to the rise time of the oscilloscope given in the data sheet. The data of the A-FET shows good agreement with the theoretical expectation, while the Gaussian width from the LA-FET does not show a increasing dependence on the pulse width. However, both the data from the A-FET as well as from the LA-FET stay above the theoretical limitations through the IF bandwidth as expected [30].

8.3. Determination of cavity parameters and comparison with state-of-the-art model

Fig. 8.3 compares the refined convolution model to the state-of-the-art piecewise ansatz both for the time domain as well as for the spectral data. The exponential broadening τ_m from the fits to the time traces of the A-FET device AN-B is compared with the exponential broadening τ_s from the fits to the spectra for both models. There is excellent agreement between the data from the spectra and the time domain measurements evaluated with the convolution model for small exponential widths, where the water vapor absorption does not cause excessive pulse broadening [30]. The limitation through the limited IF bandwidth ($\sigma_{IF,eff} = 14$ ps) can thus be effectively

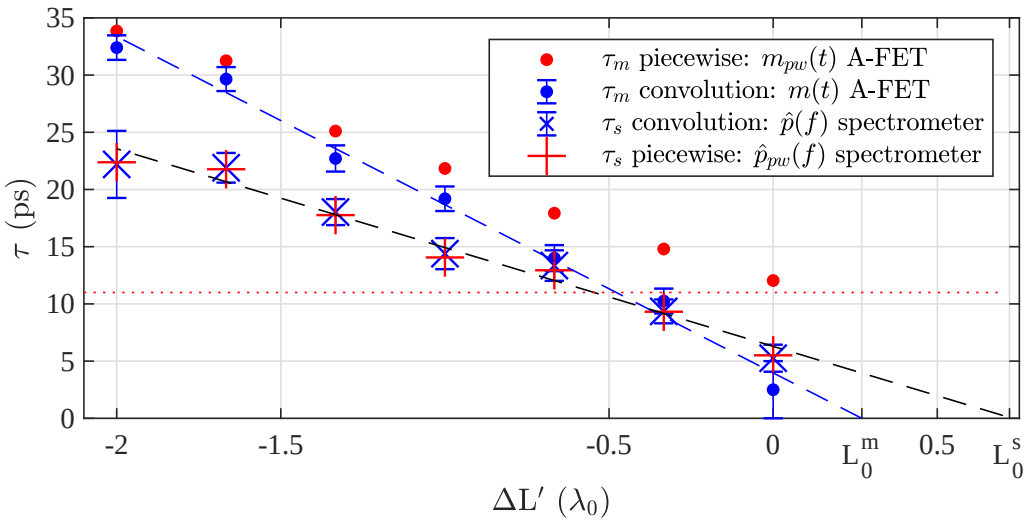

Fig. 8.3: *Exponential broadening τ evaluated with state-of-the-art piecewise model and refined convolution model vs. normalized cavity detuning $\Delta L'$. The exponential width τ_s derived from the spectroscopic data for the piecewise model $\hat{p}_{pw}(f)$ (cf. Eq. 4.3) and the convolution model $\hat{p}(f)$ (cf. Eq. 4.8) show a similar behavior. In contrast, the exponential width τ_m determined with the convolution model $m(t)$ (cf. Eq. 4.10) in time domain shows better agreement to the spectroscopic data than the data from the piecewise model $\hat{p}_{pw}(f)$ (cf. Eq. 4.3). The blue (red) dashed line is a guide to the eye fitted to the measured time domain data (measured grating spectrometer data). The red dotted line indicates the limit of the state-of-the-art ansatz for $\Delta L \to 0$. Adapted from [30] ©IEEE 2019.*

separated with the convolution ansatz (cf. Eq. 4.10) and does not limit the resolution of τ_m. Whereas the state-of-the-art piecewise ansatz is strongly affected by the IF limitations for small rise times, converging to a value of $\tau_m \approx 11\,\text{ps}$ at $\Delta L \to 0$. This corresponds to the measured Gaussian impulse response function in an exponential approximation. The piecewise model also shows increased exponential rise times for more negative cavity detuning and thus a larger deviation from the spectroscopic data for the investigated range of cavity detuning. As discussed in combination with Fig. 8.2, time domain measurements with large exponential rise times are potentially affected by excess pulse broadening in comparison with the spectroscopic data, due to absorption in water vapor.

The state-of-the-art piecewise model systematically overestimates the exponential rise time τ_m in time domain, as it cannot separate the Gaussian IF limitations from the exponential pulse width. The refined convolution ansatz allows to obtain excellent results with an accuracy of the exponential pulse width below the Gaussian IF limitation ($\sigma_{IF,eff} = 14\,\text{ps}$) [30].

The precise extraction of the exponential width τ_m from the refined model allows to determine the absolute cavity detuning ΔL and the cavity loss α (cf. Eq. 8.1). From the spectroscopic data $\hat{p}_s(f)$, the cavity loss calculates to $\alpha \approx 0.11$. The time

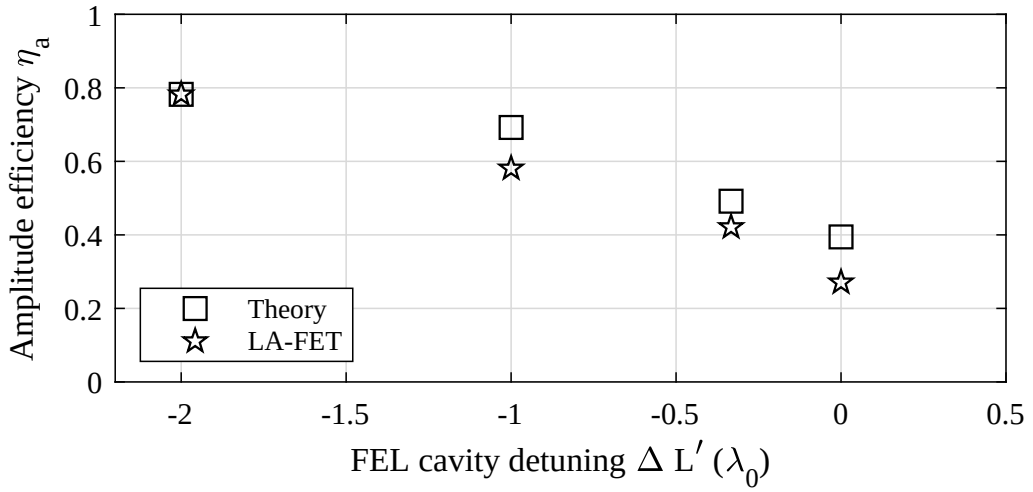

Fig. 8.4: *Amplitude efficiency η_a of LA-FET device LA-E vs FEL cavity detuning. The experimental values are normalized to the theoretical value at the longest FEL pulse at $\Delta L' = -2.0\,\lambda_0$.*

domain data $m(t)$ gives a cavity loss of $\alpha = 0.07$, potentially affected by the water vapor absorption. However, the cavity loss calculated from the time domain data is in good agreement with cavity loss simulations yielding a value of $\alpha = 0.05$ for the chosen parameters of FELBE at 2.0 THz.

The offset L_0 between the relative cavity detuning $\Delta L'$ and the absolute cavity detuning ΔL calculates to $L_0^m = -0.3\,\lambda_0$ from the time domain data using the convolution model. The spectroscopic data yields an offset of $L_0^s = -0.7\,\lambda_0$. The extracted offsets are well within the range defined by $-0.2\,\lambda_0$ from experimentally measured saturated power-optimized cavity detuning [82] and the theoretical expected value of $-1\,\lambda$ for non-saturated operation [30].

8.4. Amplitude suppression

A direct measurement of a pulse with a detector and oscilloscope having a finite response time broadens the pulse. Due to energy conservation, the pulse is not only broadened, but also the peak amplitude is suppressed at the same time. If the pulse width is in the order of the response time of the detector and the oscilloscope, there is a strong change in the amplitude efficiency η_a between the initial pulse $p(t)$ and the measured pulse $m(t)$ as discussed in context of Eq. 4.11. The FEL cavity detuning strongly changes the pulse length, while the FEL frequency remains almost constant. Short pulse lengths result in stronger amplitude suppression η_a. Fig. 8.4 shows the measured and calculated amplitude suppression vs FEL cavity detuning. The measured efficiency is normalized to the calculated value at the longest pulse. The efficiency is calculated numerically by comparing the peak height of the pulse broadened by the IF limitations ($\sigma_{IF,eff} = 14\,\text{ps}$) with the initial FEL pulse. The initial FEL pulse was calculated with the convolution model using the pulse shape

extracted from the spectroscopic measurements. The measured data shows excellent agreement with the calculated amplitude efficiency [85].

8.5. Field-effect transistor gate bias dependence

The measured pulses are broadened by the IF limitations $IF(t)$ and a finite time constant of the rectification process described by $r(t)$. The pulse widths are measured with different gate biases U_{GS} for the LA-FET and the A-FET to determine its influence on the rectification speed, as shown in Fig. 8.5 [30]. The threshold bias of the LA-FET device LA-E and A-FET device AN-B is $U_{th} = -0.4\,\mathrm{V}$ and $U_{th} = -0.5\,\mathrm{V}$, respectively.

The exponential rise time in Fig. 8.5a) is not affected significantly by the gate bias, but stays within the measurement error $\Delta\tau_m = \pm 1\,\mathrm{ps}$. This in agreement with the theoretical expectations from the convolution model, that the exponential width is not affected by the Gaussian broadening from the IF limitations $IF(t)$ and the rectification process $r(t)$.

Due to the finite transit time, the rectification process $r(t)$ is expected to become more slowly and the Gaussian width thus larger for more negative gate bias U_{GS}, scaling as $L^2/[\mu(U_{GS}-U_{th})]$ in the overdamped limit above threshold for low mobilities [84; 96]. An experimental study of a MOSFET transistor ($\mu = 200\,\mathrm{cm}^2/\mathrm{Vs}$) in an auto-correlation setup at 4.3 THz agrees to the predicted trend with an exponential time constant $\tau = 18\,\mathrm{ps}$ in the sub-threshold regime to $\tau = 12\,\mathrm{ps}$ above threshold [27]. Using the hydrodynamic equation (cf. Eq. 3.5) and additional terms from the Navier-Stokes equation, the study in ref. [84] simulated a $\tau \leq 2\,\mathrm{ps}$ for mobilities used in this thesis. The study predicts a slower rectification process for gate biases closer to threshold. In contrast, the Gaussian width σ_m from the direct measurement in this thesis shows a slight trend to smaller values for more negative U_{GS} from the range of $\sigma_m = 15.5 - 18.0\,\mathrm{ps}$ at $U_{GS} = 0\,\mathrm{V}$ to the range of $\sigma_m = 13.3 - 15.0\,\mathrm{ps}$ at $U_{GS} = -0.6\,\mathrm{V}$. This is above the measurement error, that is estimated to $\sigma_m = \pm 1\,\mathrm{ps}$, and therefore significant.

A change in the pulse width for the same initial FEL pulse width may originate from both $IF(t)$ and $r(t)$. However, the increase of the SD resistance R_{DS} does not suggest a temporal broadening of $IF(t)$ for more positive U_{GS}, but a constant $IF(t)$. The SD resistance R_{DS} in the IF path and an impedance mismatch in the IF path is not expected to alter the pulse width. The monotonous trend to smaller σ_m for more negative U_{GS} is also the same for both the LA-FET and the A-FET device, despite the lower R_{DS} of the LA-FET allowing for impedance matching in the IF path.

The amplitude of the reflections in the IF path after the main pulse depends on the gate bias (cf. Fig. 8.1). A more negative gate bias increases the FET impedance, such that e.g. for a resistance R_{SD} above the oscilloscope's $50\,\Omega$ impedance $R_{SD} > 50\,\Omega$, the reflections due to the impedance mismatch are expected to increase. A-FET device AN-B shows a smaller amplitude of the negative after-pulse for more positive gate bias. The minimum SD resistance of the A-FET AN-B is $R_{SD} = 0.4\,\mathrm{k}\Omega$, not dropping below the $50\,\Omega$ impedance of the oscilloscope. In agreement with the

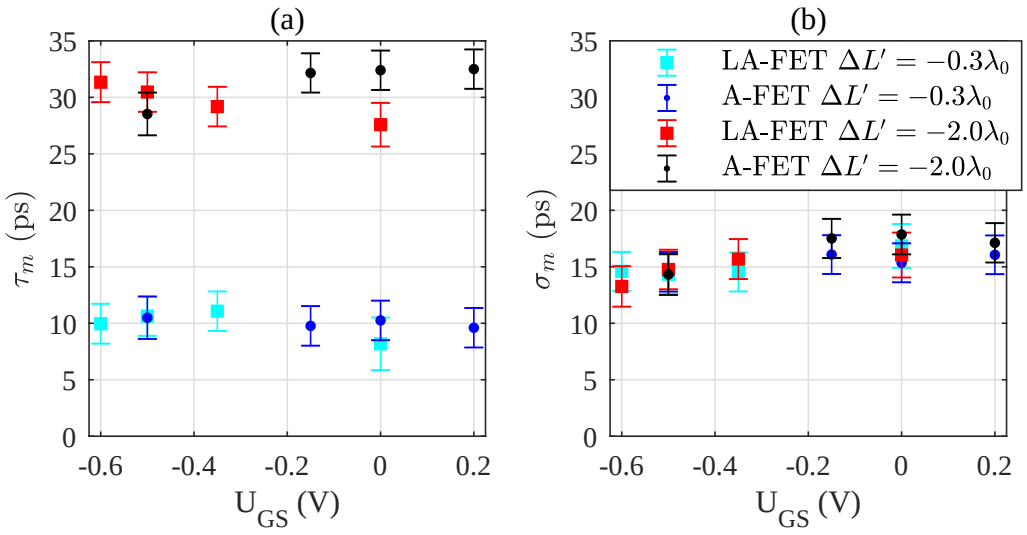

Fig. 8.5: *Measured pulse width vs gate bias U_{GS} for the LA-FET LA-E and the A-FET AN-B. a) Exponential width τ_m vs gate bias U_{GS}. b) Gaussian width σ_m vs U_{GS}. There is no significant influence on the exponential width τ_m, but a trend to smaller Gaussian pulse widths σ_m for more negative gate bias U_{GS}. Adapted from [30] ©IEEE 2019.*

expectations from impedance matching, the amplitude of the negative after-pulse increases for an even higher SD resistance of the A-FET. The negative after-pulse of the LA-FET device LA-E has a minimum amplitude at $U_{GS} = -0.35\,\mathrm{V}$, were the SD resistance is close to the $50\,\Omega$ impedance of the oscilloscope (cf. Fig. 5.4b)). Higher or lower gate biases increase the amplitude of the negative after-pulse.

Concluding, the change of the Gaussian width is only $\sigma_m \lessapprox 3\,\mathrm{ps}$, in the large range of investigated gate biases, therefore the post-detection electronics $IF(t)$ clearly dominate the pulse broadening.

9. Summary and outlook

9.1. Summary and conclusions

One goal of this thesis was the development of field-effect transistor-based detectors for ultra-short THz pulses and characterization of free electron laser (FEL) THz pulse shapes. A compact detector working at room temperature with real-time measurement capability is highly desirable in accelerator-based THz generation as well as for table-top systems. A further goal was the ultra-broadband characterization of the underlying detection mechanism with large-area field-effect transistors (LA-FETs) from the THz up to the MIR. Finally, the THz characteristics of LA-FETs were compared with antenna-coupled field-effect transistors (A-FET) regarding the frequency coverage, pulse shape characterization and radiation resistance.

In measurements, the LA-FET detector concept demonstrated an ultra-broadband frequency coverage from 0.1 up to 30 THz, only with the exception of the Reststrahlen band of the GaAs substrate in the high electron mobility transistor (HEMT). At 30 THz the results from the FEL measurements were verified with CO_2 laser measurements. The large active area allows to distribute the power and enable a dynamic range of up to 69 dB/$\sqrt{\text{Hz}}$, limited by the noise floor of the measurement electronics. The responsivity of the LA-FET devices was improved by two orders of magnitude within this thesis, now allowing the use in most table-top systems. This was not possible with LA-FET devices available at the beginning of the thesis. The detectors feature a measured impulse response function, i.e. temporal resolution of 24 ps full width at half maxmimum (FWHM), corresponding to 10 ps Gaussian $e^{-1/2}$ width, respectively. The temporal resolution was limited by the available 30 GHz oscilloscope. An upper limit for the internal rectification process of 7.1 ps Gaussian width was calculated by the deconvolution of the oscilloscope bandwidth. To the knowledge of the author, this is the fastest experimentally demonstrated detection with FETs in the THz band. The LA-FET devices display compact, easy-to-handle, room temperature detectors, ideally suited for real-time pulse shape characterization as needed for accelerator-based research, e.g. in pump-probe measurements.

The LA-FETs feature a $f^{-1.4}$ roll-off with corrected amplitude suppression, that is less strong than a RC roll-off with fixed resistance. The weaker measured roll-off may be accounted to an increasing radiation resistance at higher frequencies with smaller beam waists, improving the incoupling of THz power to the FET. The comparison with gate-less reference samples showed that the rectification signal that is generated underneath the gate contact dominates signals from other possible origin such as imperfect ohmic contacts by at least an order of magnitude. 2D scans showed that in the THz band as well as at 30 THz in the MIR the results are compatible with a fast plasmonic (Dyakonov-Shur-like) rectification mechanism on the tens-of-picosecond scale regarding the polarization dependence, distribution on the detector area, and the comparison with gate-less devices. The picosecond-scale response to a THz field polarized perpendicular to the FET channel is strongly suppressed in contrast to a THz field along the channel. This is compatible with the

expectations for a rectification along the channel underneath the gate contact. At the boundaries of the LA-FET devices to the pads, a THz field polarized perpendicular to the channel couples to the FET via contact pads that generates a response. The antenna-less design proved its applicability for studying an extreme frequency range without undesired incoupling through bond wires. However, the gate-bias dependence weakens with increasing frequency, pointing towards a yet unidentified detection process. The averaged response measured with a lock-in amplifier showed a significant contribution from gate-less reference samples at 30 THz pointing towards additional thermal detection processes. The temperature-dependent charge carrier density and charge carrier mobility in the semiconductor causes a bolometric detection mechanism, that may contribute significantly to the averaged signal at 30 THz.

The antenna-coupled devices proved a strongly enhanced responsivity on the low frequency end of the THz band. With simple UV-contact lithography, a noise equivalent power (NEP) of 250 pW/$\sqrt{\text{Hz}}$ at 0.6 THz could be obtained, that is only one order above foundry-processed silicon-based metal–oxide–semiconductor field-effect transistors (MOSFETs). The measured responsivity from 0.1 up to 11.8 THz agrees very well with the calculated responsivity from the transmission line model using a simulated radiation resistance and measured material parameters. Both the 30 μm wide A-FET, as well as the LA-FET devices with an effective width in the tens of mm feature a 1 dB saturation point in the mV range. The very similar saturation point despite orders of magnitude difference in the radiation resistance and device size proves that the saturation of the detector is solely determined by the coupling efficiencies of the THz power to the active rectifying element, not by the layout of the device.

Both LA-FET and A-FET detectors demonstrated the capability of picosecond-scale recording of FEL pulses. A refined model for the FEL pulse shape, developed within this thesis, allows to include the Gaussian IF limitations in a simple manner. Further, the model allows to obtain the exponential width of the FEL pulse much below the Gaussian IF time constant. The refined model was further verified with measurements in the frequency domain with a grating spectrometer. This demonstrates the capability of direct real-time detection with FETs. The FET detectors do not require long scanning-type measurements or complex setups. Further, direct detection does not require reconstruction of the pulses from the intensity spectra loosing the phase information, or complex deconvolution of auto-correlation measurements, or low-jitter phase-stability of the (accelerator-based) THz source.

Second generation LA-FET detectors with two orders of magnitude improved responsivity were fabricated within this thesis. One improved detector is now regularly used at the FEL at the Helmholtz-Zentrum Dresden-Rossendorf (FELBE) without additional pre-amplifiers demonstrating the applicability of the LA-FET concept. Further, an antenna-coupled A-FET detector with low NEP was used for detection of THz radiation from a quantum cascade laser at 3.8 THz in the group of Prof. Unterrainer at TU Wien, as well as for the detection of a photomixer-generated signal below 1.6 THz. This proves the versatility of the detection concept.

9.2. Outlook

This thesis showed that the rectification in A-FETs, as well as in LA-FETs are promising concepts for ultra-fast and ultra-broadband THz detection at room temperature. For further applications, a technological improvement as well as further research on the underlying detection mechanisms are highly desirable. Examples for further research and a proposal for a development of a detector concept accelerator-based experiments are given in the following paragraphs.

In a sample without gate contact, as used in this thesis, both a Dyakonov-Shur rectification and a thermoelectric mechanism can be excluded. Drift currents of thermoelectric origin, arising from gradients in the charge carrier density and temperature must be quantified exclusively using an adapted sample structure. With an aperture that partially shields the channel, e.g. a local reflection coating or a shadow mask, a charge carrier temperature gradient in the channel would be created, and subsequently a thermoelectric drift current is expected. The charge carrier density can be altered along the channel with a local surface modification by different dielectric layers on the surface that modify the barrier thickness or by local diffusion of dopants into the channel. Both methods create a charge carrier density gradient along the channel.

The latter technique can also be used for further optimization of the electrical coupling efficiency of the THz radiation to the transistor. The resistance of ungated areas in the channel, i.e. the access resistance can be decreased by surface modification that increases the charge carrier density. This is an alternative to implantation of dopants to GaAs, where the mobility decreases significantly. A different gate electrode material, increasing the Schottky barrier thickness to decrease the number of charge carriers, may further help to increase the resistance of the actual rectifying element and thereby achieve a higher coupling efficiency.

With scientists from KIT and TU Dresden, a concept for accelerator-based beam diagnostic was developed. The concept aims for pulse-to-pulse monitoring of the beam pointing stability and the beam intensity as shown in Fig. 9.1a). The integration of pre-amplifiers would greatly enhance the sensitivity of the measurement, as the noise floor in this thesis was limited by the oscilloscope. For pulse-to-pulse intensity and pointing stability monitoring a relatively small IF bandwidth of 30 MHz suffices for the repetition rate of 13 MHz at FELBE. The read-out can be done with a 4-channel oscilloscope, or the KAPTURE-2 data acquisition system from KIT. In a next step, a concept with more than 4 pixels would also possible. Fig. 9.1b) shows the concept of a single pixel detector as used in this thesis, but with an improved IF bandwidth. The main limitation of the IF bandwidth in this thesis was the 30 GHz oscilloscope and the wiring. The handmade custom wiring from the FET to the SMA connector could be replaced by a coplanar waveguide (CPW) and a type V connector. In combination with faster measurement electronics, such as the KAPTURE-2 from KIT, or a 67 GHz oscilloscope this would allow a factor 2 or more improved IF bandwidth for pulse shape characterization. An amplifier integrated within the CPW will further increase the sensitivity currently limited by the oscilloscope's noise level.

The aim is to submit this proposal to the Deutsche Forschungsgemeinschaft.

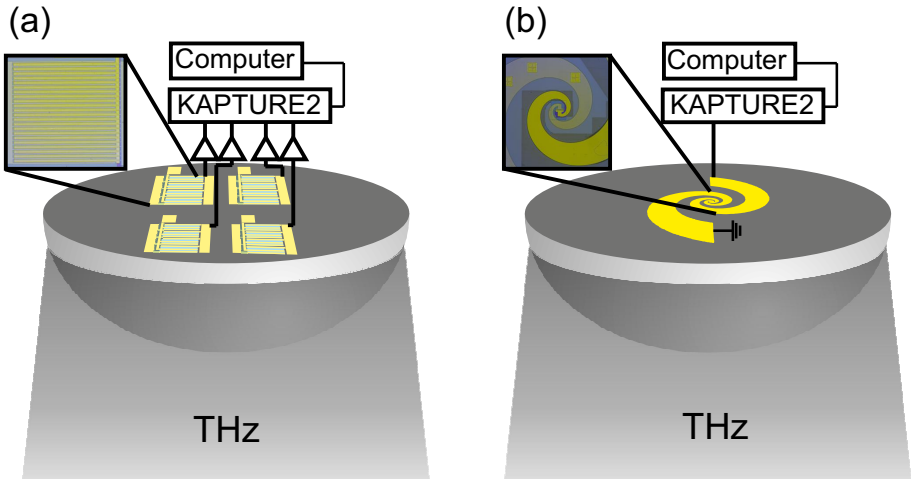

Fig. 9.1: *a) Concept of a quadrant detector using LA-FET detector elements. The signals from the individual sensors are to be pre-amplified and measured with new post-detection electronics. b) Sensitive single-pixel sensor for measurement of low power signals with* > 60 *GHz IF bandwidth.*

References

[1] S. Preu, G. H. Döhler, S. Malzer, L. J. Wang, and A. C. Gossard, "Tunable, continuous-wave Terahertz photomixer sources and applications," *Journal of Applied Physics*, vol. 109, no. 6, p. 061301, mar 2011.

[2] E. Bründermann, H.-W. Hübers, and M. F. Kimmitt, *Terahertz Techniques*, ser. Springer Series in Optical Sciences. Berlin, Heidelberg: Springer Berlin Heidelberg, 2012, vol. 151.

[3] T. Nagatsuma, "Breakthroughs in Photonics 2013: THz Communications Based on Photonics," *IEEE Photonics Journal*, vol. 6, no. 2, pp. 1–5, apr 2014.

[4] B. Ku, P. Schmalenberg, O. Inac, O. D. Gurbuz, J. S. Lee, K. Shiozaki, and G. M. Rebeiz, "A 77–81-GHz 16-Element Phased-Array Receiver With±50°Beam Scanning for Advanced Automotive Radars," *IEEE Transactions on Microwave Theory and Techniques*, vol. 62, no. 11, pp. 2823–2832, 2014.

[5] C. F. Neese, I. R. Medvedev, G. M. Plummer, A. J. Frank, C. D. Ball, and F. C. D. Lucia, "Compact Submillimeter/Terahertz Gas Sensor With Efficient Gas Collection, Preconcentration, and ppt Sensitivity," *IEEE Sensors Journal*, vol. 12, no. 8, pp. 2565–2574, 2012.

[6] E. R. Brown, J. E. Bjarnason, A. M. Fedor, and T. M. Korter, "On the strong and narrow absorption signature in lactose at 0.53 THz," *Applied Physics Letters*, vol. 90, no. 6, p. 061908, feb 2007.

[7] J. L. Steinmann, T. Boltz, M. Brosi, E. Bründermann, M. Caselle, B. Kehrer, L. Rota, P. Schönfeldt, M. Schuh, M. Siegel, M. Weber, and A.-S. Müller, "Continuous bunch-by-bunch spectroscopic investigation of the microbunching instability," *Physical Review Accelerators and Beams*, vol. 21, no. 11, p. 110705, nov 2018.

[8] Y.-S. Lee, *Principles of Terahertz Science and Technology.* Boston, MA: Springer US, 2009.

[9] S. Regensburger, "GaAs-Feldeffekttransistoren zur breitbandigen Detektion von Terahertz-Strahlung," master's thesis, Friedrich-Alexander Universität Erlangen-Nürnberg, 2013.

[10] B. Zaks, R. B. Liu, and M. S. Sherwin, "Experimental observation of electron–hole recollisions," *Nature*, vol. 483, p. 580, mar 2012.

[11] M. Wagner, H. Schneider, D. Stehr, S. Winnerl, A. M. Andrews, S. Schartner, G. Strasser, and M. Helm, "Observation of the Intraexciton Autler-Townes Effect in GaAs/AlGaAs Semiconductor Quantum Wells," *Phys. Rev. Lett.*, vol. 105, no. 16, p. 167401, 2010.

[12] H. A. Hafez, S. Kovalev, J.-C. Deinert, Z. Mics, B. Green, N. Awari, M. Chen, S. Germanskiy, U. Lehnert, J. Teichert, Z. Wang, K.-J. Tielrooij, Z. Liu, Z. Chen, A. Narita, K. Müllen, M. Bonn, M. Gensch, and D. Turchinovich, "Extremely efficient terahertz high-harmonic generation in graphene by hot Dirac fermions," *Nature*, vol. 561, no. 7724, pp. 507–511, 2018.

[13] A. Hirata and M. Yaita, "Ultrafast Terahertz Wireless Communications Technologies," *IEEE Transactions on Terahertz Science and Technology*, vol. 5, no. 6, pp. 1128–1132, nov 2015.

[14] P. Thoma, A. Scheuring, S. Wunsch, K. Il'in, A. Semenov, H.-W. Hubers, V. Judin, A.-S. Muller, N. Smale, M. Adachi, S. Tanaka, S.-i. Kimura, M. Katoh, N. Yamamoto, M. Hosaka, E. Roussel, C. Szwaj, S. Bielawski, and M. Siegel, "High-Speed Y-Ba-Cu-O Direct Detection System for Monitoring Picosecond THz Pulses," *IEEE Transactions on Terahertz Science and Technology*, vol. 3, no. 1, pp. 81–86, jan 2013.

[15] E. Roussel, C. Evain, C. Szwaj, S. Bielawski, J. Raasch, P. Thoma, A. Scheuring, M. Hofherr, K. Ilin, S. Wünsch, M. Siegel, M. Hosaka, N. Yamamoto, Y. Takashima, H. Zen, T. Konomi, M. Adachi, S. Kimura, and M. Katoh, "Microbunching instability in relativistic electron bunches: direct observations of the microstructures using ultrafast YBCO detectors." *Physical review letters*, vol. 113, no. 9, p. 094801, aug 2014.

[16] M. Ali, R. C. Guzman, A. Rivera-Lavado, O. Cojocari, L. E. Garcia-Mufioz, and G. Carpintero, "Quasi-Optical Schottky Barrier Diode Detector for mmWave/sub-THz Wireless Communication," in *2018 25th International Conference on Telecommunications (ICT)*, jun 2018, pp. 279–282.

[17] J. Hesler, K. Hui, and T. Crowe, "Ultrafast millimeter-wave and THz envelope detectors for wireless communications," in *2012 IEEE International Topical Meeting on Microwave Photonics*, 2012, pp. 93–94.

[18] A. Semenov, M. Ries, H.-W. Hübers, M. Sobornytskyy, G. Wüstefeld, O. Cojocari, R. Müller, A. Hoehl, and A. Pohl, "Schottky Diode Detectors for Monitoring Coherent THz Synchrotron Radiation Pulses," in *Proceedings, 5th International Particle Accelerator Conference (IPAC 2014): Dresden, Germany, June 15-20, 2014*, 2014.

[19] S. Blin, L. Tohme, D. Coquillat, S. Horiguchi, Y. Minamikata, S. Hisatake, P. Nouvel, T. Cohen, A. Pénarier, F. Cano, L. Varani, W. Knap, and T. Nagatsuma, "Wireless communication at 310 GHz using GaAs high-electron-mobility transistors for detection," *Journal of Communications and Networks*, vol. 15, no. 6, pp. 559–568, 2013.

[20] C. Fattinger and D. Grischkowsky, "Point source terahertz optics," *Applied Physics Letters*, vol. 53, no. 16, pp. 1480–1482, oct 1988.

[21] M. van Exter and D. Grischkowsky, "Characterization of an optoelectronic terahertz beam system," *IEEE Transactions on Microwave Theory and Techniques*, vol. 38, no. 11, pp. 1684–1691, 1990.

[22] Q. Wu and X. Zhang, "Free-space electro-optic sampling of terahertz beams," *Applied Physics Letters*, vol. 67, no. 24, pp. 3523–3525, dec 1995.

[23] S. Kovalev, B. Green, T. Golz, S. Maehrlein, N. Stojanovic, A. S. Fisher, T. Kampfrath, and M. Gensch, "Probing ultra-fast processes with high dynamic range at 4th-generation light sources: Arrival time and intensity binning at unprecedented repetition rates," *Structural Dynamics*, vol. 4, no. 2, p. 24301, mar 2017.

[24] J. Shan, A. S. Weling, E. Knoesel, L. Bartels, M. Bonn, A. Nahata, G. A. Reider, and T. F. Heinz, "Single-shot measurement of terahertz electromagnetic pulses by use of electro-optic sampling," *Optics Letters*, vol. 25, no. 6, p. 426, mar 2000.

[25] R. Kiessling, W. B. Colson, S. Gewinner, W. Schöllkopf, M. Wolf, and A. Paarmann, "Femtosecond single-shot timing and direct observation of subpulse formation in an infrared free-electron laser," *Physical Review Accelerators and Beams*, vol. 21, no. 8, p. 080702, aug 2018.

[26] S. Preu, M. Mittendorff, S. Winnerl, O. Cojocari, and A. Penirschke, "THz Autocorrelators for ps Pulse Characterization Based on Schottky Diodes and Rectifying Field-Effect Transistors," *IEEE Transactions on Terahertz Science and Technology*, 2015.

[27] A. Lisauskas, K. Ikamas, S. Massabeau, M. Bauer, D. Čibiraite, J. Matukas, J. Mangeney, M. Mittendorff, S. Winnerl, V. Krozer, and H. G. Roskos, "Field-effect transistors as electrically controllable nonlinear rectifiers for the characterization of terahertz pulses," *APL Photonics*, vol. 3, no. 5, p. 051705, may 2018.

[28] S. Regensburger, M. Mittendorff, S. Winnerl, H. Lu, A. C. Gossard, and S. Preu, "Broadband THz detection from 0.1 to 22 THz with large area field-effect transistors," *Optics express*, vol. 23, no. 16, pp. 20 732–20 742, 2015.

[29] S. Regensburger, A. k. Mukherjee, S. Schönhuber, M. A. Kainz, S. Winnerl, J. M. Klopf, H. Lu, A. C. Gossard, K. Unterrainer, and S. Preu, "Broadband Terahertz Detection with Zero-Bias Field-Effect Transistors between 100 GHz and 11.8 THz with a Noise Equivalent Power of 250 pW/$\sqrt{Hz}$ at 0.6 THz," *IEEE Transactions on Terahertz Science and Technology*, vol. 8, no. 4, pp. 465–471, 2018.

[30] S. Regensburger, S. Winnerl, J. M. Klopf, H. Lu, A. C. Gossard, and S. Preu, "Picosecond-scale Terahertz pulse characterization with field-effect transistors,"

IEEE Transactions on Terahertz Science and Technology, vol. 9, no. 3, pp. 262 – 271, 2019.

[31] A. M. MacLeod, X. Yan, W. A. Gillespie, G. M. H. Knippels, D. Oepts, A. F. G. van der Meer, C. W. Rella, T. I. Smith, and H. A. Schwettman, "Formation of low time-bandwidth product, single-sided exponential optical pulses in free-electron laser oscillators," *Physical Review E*, vol. 62, no. 3, pp. 4216–4220, sep 2000.

[32] C. Deutsch, M. A. Kainz, M. Krall, M. Brandstetter, D. Bachmann, S. Schönhuber, H. Detz, T. Zederbauer, D. MacFarland, A. M. Andrews, W. Schrenk, M. Beck, K. Ohtani, J. Faist, G. Strasser, and K. Unterrainer, "High-Power Growth-Robust InGaAs/InAlAs Terahertz Quantum Cascade Lasers," *ACS Photonics*, vol. 4, no. 4, pp. 957–962, apr 2017.

[33] S. Ganichev and W. Prettl, *Intense Terahertz Excitation of Semiconductors*. Oxford University Press, dec 2005.

[34] M. J. E. Golay, "Theoretical Consideration in Heat and Infra-Red Detection, with Particular Reference to the Pneumatic Detector," *Review of Scientific Instruments*, vol. 18, no. 5, pp. 347–356, may 1947.

[35] H.-W. Hübers, G. W. Schwaab, and H. P. Röser, "Video detection and mixing performance of GaAs Schottky-barrier diodes at 30 THz and comparison with metal-insulator-metal diodes," *Journal of Applied Physics*, vol. 75, no. 8, p. 4243, apr 1994.

[36] M. Hoefle, K. Haehnsen, I. Oprea, O. Cojocari, A. Penirschke, and R. Jakoby, "Compact and Sensitive Millimetre Wave Detectors Based on Low Barrier Schottky Diodes on Impedance Matched Planar Antennas," *Journal of Infrared, Millimeter, and Terahertz Waves*, vol. 35, no. 11, pp. 891–908, nov 2014.

[37] J. L. Hesler, T. W. Crowe, and V. Diodes, "Responsivity and Noise Measurements of Zero-Bias Schottky Diode Detectors," *18th International Symposium on Space Terahertz Technology*, no. March, pp. 89–92, 2007.

[38] C. Sydlo, O. Cojocari, D. Schoenherr, T. Goebel, S. Jatta, H. L. Hartnagel, and P. Meissner, "Ultrawideband THz detector based on a zero- bias Schottky diode," *19th International Symposium on Space Terahertz Technology*, no. April, p. 520, 2008.

[39] E. R. Brown, A. C. Young, J. E. Bjarnason, J. D. Zimmerman, A. C. Gossard, and H. Kazemi, "Millimeter and sub-millimeter wave performance of an ErAs:InAlGaAs Schottky diode coupled to a single-turn square spiral," *International Journal of High Speed Electronics and Systems*, vol. 17, no. 02, pp. 383–394, jun 2007.

[40] M. Laabs, N. Neumann, B. Green, N. Awari, J. Deinert, S. Kovalev, D. Plettemeier, M. Gensch, and IUCr, "On-chip THz spectrometer for bunch compression fingerprinting at fourth-generation light sources," *Journal of Synchrotron Radiation*, vol. 25, no. 5, pp. 1509–1513, sep 2018.

[41] M. Sakhno, F. Sizov, and A. Golenkov, "Uncooled THz/sub-THz Rectifying Detectors: FET vs. SBD," *Journal of Infrared, Millimeter, and Terahertz Waves*, vol. 34, no. 12, pp. 798–814, dec 2013.

[42] U. R. Pfeiffer and E. Öjefors, "A 600-GHz CMOS focal-plane array for terahertz imaging applications," *ESSCIRC 2008 - Proceedings of the 34th European Solid-State Circuits Conference*, pp. 110–113, 2008.

[43] J. Grzyb and U. Pfeiffer, "THz Direct Detector and Heterodyne Receiver Arrays in Silicon Nanoscale Technologies," *Journal of Infrared, Millimeter, and Terahertz Waves*, vol. 36, no. 10, pp. 998–1032, oct 2015.

[44] M. Bauer, R. Venckevičius, I. Kašalynas, S. Boppel, M. Mundt, L. Minkevičius, A. Lisauskas, G. Valušis, V. Krozer, and H. G. Roskos, "Antenna-coupled field-effect transistors for multi-spectral terahertz imaging up to 4.25 THz." *Optics express*, vol. 22, no. 16, pp. 19 235–41, aug 2014.

[45] W. Knap, F. Teppe, N. Dyakonova, D. Coquillat, and J. Łusakowski, "Plasma wave oscillations in nanometer field effect transistors for terahertz detection and emission," *Journal of Physics: Condensed Matter*, vol. 20, no. 38, p. 384205, sep 2008.

[46] D. Veksler, F. Teppe, A. Dmitriev, V. Kachorovskii, W. Knap, and M. Shur, "Detection of terahertz radiation in gated two-dimensional structures governed by dc current," *Physical Review B*, vol. 73, no. 12, p. 125328, mar 2006.

[47] V. Ryzhii, A. Satou, W. Knap, and M. S. Shur, "Plasma oscillations in high-electron-mobility transistors with recessed gate," *Journal of Applied Physics*, vol. 99, no. 8, p. 084507, apr 2006.

[48] V. Krozer, M. Mittendorff, A. Lisauskas, L. Minkevicius, H. G. Roskos, S. Boppel, M. Mundt, S. Winnerl, I. Kasalynas, G. Valusis, and D. Seliuta, "CMOS Integrated Antenna-Coupled Field-Effect Transistors for the Detection of Radiation From 0.2 to 4.3 THz," *IEEE Transactions on Microwave Theory and Techniques*, vol. 60, no. 12, pp. 3834–3843, dec 2012.

[49] S. Boppel, M. Ragauskas, A. Hajo, M. Bauer, A. Lisauskas, S. Chevtchenko, A. Ramer, I. Kasalynas, G. Valusis, H.-J. Wurfl, W. Heinrich, G. Trankle, V. Krozer, and H. G. Roskos, "0.25-um GaN TeraFETs Optimized as THz Power Detectors and Intensity-Gradient Sensors," *IEEE Transactions on Terahertz Science and Technology*, vol. 6, no. 2, p. 348, 2016.

[50] W. Knap, V. Kachorovskii, Y. Deng, S. Rumyantsev, J.-Q. Lü, R. Gaska, M. S. Shur, G. Simin, X. Hu, M. A. Khan, C. A. Saylor, and L. C. Brunel, "Nonresonant detection of terahertz radiation in field effect transistors," *Journal of Applied Physics*, vol. 91, no. 11, p. 9346, may 2002.

[51] V. V. Popov, O. V. Polischuk, T. V. Teperik, X. G. Peralta, S. J. Allen, N. J. M. Horing, and M. C. Wanke, "Absorption of terahertz radiation by plasmon modes in a grid-gated double-quantum-well field-effect transistor," *Journal of Applied Physics*, vol. 94, no. 5, p. 3556, aug 2003.

[52] A. V. Muravjov, D. B. Veksler, V. V. Popov, O. V. Polischuk, N. Pala, X. Hu, R. Gaska, H. Saxena, R. E. Peale, and M. S. Shur, "Temperature dependence of plasmonic terahertz absorption in grating-gate gallium-nitride transistor structures," *Applied Physics Letters*, vol. 96, no. 4, p. 042105, jan 2010.

[53] V. V. Popov, D. M. Ermolaev, K. V. Maremyanin, N. A. Maleev, V. E. Zemlyakov, V. I. Gavrilenko, and S. Y. Shapoval, "High-responsivity terahertz detection by on-chip InGaAs/GaAs field-effect-transistor array," *Applied Physics Letters*, vol. 98, no. 15, p. 153504, apr 2011.

[54] S. Preu, M. Mittendorff, S. Winnerl, H. Lu, A. C. Gossard, and H. B. Weber, "Ultra-fast transistor-based detectors for precise timing of near infrared and THz signals." *Optics express*, vol. 21, no. 15, pp. 17 941–50, jul 2013.

[55] S. Preu, S. Kim, R. Verma, P. G. Burke, M. S. Sherwin, and A. C. Gossard, "An improved model for non-resonant terahertz detection in field-effect transistors," *Journal of Applied Physics*, vol. 111, no. 2, p. 024502, jan 2012.

[56] S. Preu, H. Lu, M. S. Sherwin, and A. C. Gossard, "Detection of nanosecond-scale, high power THz pulses with a field effect transistor." *The Review of scientific instruments*, vol. 83, no. 5, p. 053101, may 2012.

[57] S. Preu, S. Regensburger, S. Kim, M. Mittendorff, S. Winnerl, S. Malzer, H. Lu, P. G. Burke, A. C. Gossard, H. B. Weber, and M. S. Sherwin, "Broadband THz detection and homodyne mixing using GaAs high-electron-mobility transistor rectifiers," in *SPIE Security + Defence*, N. A. Salmon and E. L. Jacobs, Eds. International Society for Optics and Photonics, oct 2013, p. 89000R.

[58] M. Dyakonov and M. Shur, "Detection, mixing, and frequency multiplication of terahertz radiation by two-dimensional electronic fluid," *IEEE Transactions on Electron Devices*, vol. 43, no. 3, pp. 380–387, 1996.

[59] W. Knap and M. Dyakonov, "Field effect transistors for terahertz applications," *Handbook of Terahertz Technology for Imaging, Sensing and Communications*, pp. 121–155, jan 2013.

[60] M. Sakhno, A. Golenkov, and F. Sizov, "Uncooled detector challenges: Millimeter-wave and terahertz long channel field effect transistor and Schottky barrier diode detectors," *Journal of Applied Physics*, vol. 114, no. 16, p. 164503, oct 2013.

[61] M. Dyakonov and M. Shur, "Shallow water analogy for a ballistic field effect transistor: New mechanism of plasma wave generation by dc current," pp. 2465–2468, oct 1993.

[62] S. Boppel, "Field-Effect-Transistor-Based Detection of Terahertz Radiation: Modelling, Implementation and Application," Doctoral thesis, Johann Wolfgang Goethe-Universität Frankfurt, 2013.

[63] M. A. Andersson and J. Stake, "An Accurate Empirical Model Based on Volterra Series for FET Power Detectors," *IEEE Transactions on Microwave Theory and Techniques*, vol. 64, no. 5, pp. 1431–1441, may 2016.

[64] S. Boppel, A. Lisauskas, and H. G. Roskos, "Terahertz array imagers: Towards the implementation of terahertz cameras with plasma-wave-based silicon MOSFET detectors," in *Handbook of Terahertz Technology for Imaging, Sensing and Communications*. Elsevier, 2013, pp. 231–271.

[65] H. G. Roskos, M. Bauer, K. Ikamas, F. Ludwig, and A. Lisauskas, "THz Detection with Field-Effect Transistors: The Role of Plasma Waves and of Thermoelectric Contributions," in *2018 43rd International Conference on Infrared, Millimeter, and Terahertz Waves (IRMMW-THz)*. IEEE, sep 2018.

[66] S. Regensburger, A. K. Mukherjee, S. Preu, H. Lu, and A. C. Gossard, "Broadband Terahertz Detection with an Antenna Coupled Zero-Bias Field-Effect Transistor," in *2018 43rd International Conference on Infrared, Millimeter, and Terahertz Waves (IRMMW-THz)*. IEEE, sep 2018.

[67] S. Regensburger, M. Mittendorff, S. Winnerl, H. Lu, A. C. Gossard, and S. Preu, "Symmetry effects in broadband, room-temperature field effect transistor THz detectors," in *2015 40th International Conference on Infrared, Millimeter, and Terahertz waves (IRMMW-THz)*. IEEE, aug 2015.

[68] A. Lisauskas, M. Bauer, A. Ramer, K. Ikamas, J. Matukas, S. Chevtchenko, W. Heinrich, V. Krozer, and H. G. Roskos, "Terahertz rectification by plasmons and hot carriers in gated 2D electron gases," in *2015 International Conference on Noise and Fluctuations (ICNF)*. IEEE, jun 2015, pp. 1–5.

[69] M. Bauer, M. Andersson, A. Zak, P. Sakalas, D. Čibiraitė, A. Lisauskas, M. Schröter, J. Stake, and H. G. Roskos, "The potential for sensitivity enhancement by the thermoelectric effect in carbon-nanotube and graphene Tera-FETs," *Journal of Physics: Conference Series*, vol. 647, no. 1, p. 012004, oct 2015.

[70] M. Bauer, S. Boppel, J. Zhang, A. Rämer, S. Chevtchenko, A. Lisauskas, W. Heinrich, V. Krozer, and H. G. Roskos, "Optimization of the Design of Terahertz Detectors Based on Si CMOS and AlGaN/GaN Field-Effect Transistors," *International Journal of High Speed Electronics and Systems*, vol. 25, no. 03n04, p. 1640013, sep 2016.

[71] A. Zak, M. A. Andersson, M. Bauer, J. Matukas, A. Lisauskas, H. G. Roskos, and J. Stake, "Antenna-Integrated 0.6 THz FET Direct Detectors Based on CVD Graphene," *Nano Letters*, vol. 14, no. 10, pp. 5834–5838, oct 2014.

[72] L. Vicarelli, M. S. Vitiello, D. Coquillat, A. Lombardo, A. C. Ferrari, W. Knap, M. Polini, V. Pellegrini, and A. Tredicucci, "Graphene field-effect transistors as room-temperature terahertz detectors," *Nature Materials*, vol. 11, no. 10, pp. 865–871, oct 2012.

[73] C. A. Balanis, *Antenna Theory: Analysis and Design, 3rd Edition*. Wiley-Interscience, 2005.

[74] S. Preu, "Continuous-wave, Tunable THz Ni-pn-ip Superlattice Photomixers and Applications," Dissertation, Friedrich-Alexander Universität Erlangen-Nürnberg, 2009.

[75] Y. Huo, G. W. Taylor, and R. Bansal, "Planar log-periodic antennas on extended hemishperical silicon lenses for millimeter/submillimeter wave detection applications," *International Journal of Infrared and Millimeter Waves*, vol. 23, no. 6, pp. 819–839, 2002.

[76] A. Lisauskas, S. Boppel, J. Matukas, V. Palenskis, L. Minkevičius, G. Valušis, P. Haring-Bolívar, and H. G. Roskos, "Terahertz responsivity and low-frequency noise in biased silicon field-effect transistors," *Applied Physics Letters*, vol. 102, no. 15, p. 153505, apr 2013.

[77] A. Lisauskas, U. Pfeiffer, E. Öjefors, P. H. Bolívar, D. Glaab, and H. G. Roskos, "Rational design of high-responsivity detectors of terahertz radiation based on distributed self-mixing in silicon field-effect transistors," *Journal of Applied Physics*, vol. 105, no. 11, p. 114511, 2009.

[78] S. Sze and K. K. Ng, *Physics of Semiconductor Devices*. Hoboken, NJ, USA: John Wiley and Sons, oct 2006.

[79] D. Stehr, "Infrared studies of impurity states and ultrafast carrier dynamics in semiconductor quantum structures," Ph.D. dissertation, TU Dresden, Forschungszentrum Dresden-Rossendorf, 2007.

[80] P. Schmüser, M. Dohlus, J. Rossbach, and C. Behrens, "Free-electron lasers in the ultraviolet and X-ray regime," *Springer Tracts in Modern Physics*, vol. 258, 2014.

[81] R. Hajima, N. Nishimori, R. Nagai, M. Sawamura, N. Kikuzawa, T. Shizuma, and E. Minehara, "Demonstration of a high-power FEL oscillator with high extraction-efficiency," in *PACS2001. Proceedings of the 2001 Particle Accelerator Conference*, vol. 4. IEEE, 2001, pp. 2733–2735.

[82] D. Jaroszynski, D. Oepts, A. Van Der Meer, P. Van Amersfoort, and W. Colson, "Consequences of short electron-beam pulses in the FELIX project," *Nuclear Instruments and Methods in Physics Research Section A: Accelerators, Spectrometers, Detectors and Associated Equipment*, vol. 296, no. 1-3, pp. 480–484, oct 1990.

[83] M. Teich, M. Wagner, H. Schneider, and M. Helm, "Semiconductor quantum well excitons in strong, narrowband terahertz fields," *New Journal of Physics*, vol. 15, no. 6, p. 065007, jun 2013.

[84] S. Rudin, G. Rupper, and M. Shur, "Ultimate response time of high electron mobility transistors," *Journal of Applied Physics*, vol. 117, no. 17, p. 174502, may 2015.

[85] S. Regensburger, S. Winnerl, J. M. Klopf, H. Lu, A. C. Gossard, and S. Preu, "Amplitude suppression of picosecond Terahertz pulses in a FET detector," in *Optical Terahertz Science and Technology (OTST 2019)*, mar 2019.

[86] S. Regensburger, S. Winnerl, J. Klopf, H. Lu, A. C. Gossard, and S. Preu, "Investigation of parasitic coupling of THz radiation to a large area field-effect transistor," in *2017 42nd International Conference on Infrared, Millimeter, and Terahertz Waves (IRMMW-THz)*. IEEE, aug 2017.

[87] S. Regensburger, S. Winnerl, J. M. Klopf, H. Lu, P. G. Burke, A. C. Gossard, and S. Preu, "Comparison and responsivity improvement of horn- and lens-coupled large area field-effect transistors," in *2nd German Terahertz Conference in Dresden*, 2017.

[88] M. Wagner, "Terahertz studies on semiconductor quantum heterostructures in the low and high field regime," Ph.D. dissertation, TU Dresden, Forschungszentrum Dresden-Rossendorf, 2010.

[89] J. D. Sun, Y. F. Sun, D. M. Wu, Y. Cai, H. Qin, and B. S. Zhang, "High-responsivity, low-noise, room-temperature, self-mixing terahertz detector realized using floating antennas on a GaN-based field-effect transistor," *Applied Physics Letters*, 2012.

[90] Z.-y. Liu, L.-y. Liu, J. Yang, and N.-j. Wu, "A CMOS Fully Integrated 860-GHz Terahertz Sensor," *IEEE Transactions on Terahertz Science and Technology*, vol. 7, no. 4, pp. 455–465, jul 2017.

[91] D. B. But, C. Drexler, M. V. Sakhno, N. Dyakonova, O. Drachenko, F. F. Sizov, A. Gutin, S. D. Ganichev, and W. Knap, "Nonlinear photoresponse of field effect transistors terahertz detectors at high irradiation intensities," *Journal of Applied Physics*, vol. 115, no. 16, p. 164514, apr 2014.

[92] W. Knap, J. Lusakowski, T. Parenty, S. Bollaert, A. Cappy, V. V. Popov, and M. S. Shur, "Terahertz emission by plasma waves in 60 nm gate high electron mobility transistors," *Applied Physics Letters*, vol. 84, no. 13, pp. 2331–2333, mar 2004.

[93] S. Regensburger, H. Lu, A. C. Gossard, and S. Preu, "Comparison of large area and lumped element field-effect transistors for broadband detection of Terahertz," in *2017 42nd International Conference on Infrared, Millimeter, and Terahertz Waves (IRMMW-THz)*. IEEE, aug 2017.

[94] C. Drexler, N. Dyakonova, P. Olbrich, J. Karch, M. Schafberger, K. Karpierz, Y. Mityagin, M. B. Lifshits, F. Teppe, O. Klimenko, Y. M. Meziani, W. Knap, and S. D. Ganichev, "Helicity sensitive terahertz radiation detection by field effect transistors," *Journal of Applied Physics*, vol. 111, no. 12, p. 124504, jun 2012.

[95] M. Sakowicz, J. Łusakowski, K. Karpierz, M. Grynberg, W. Knap, and W. Gwarek, "Polarization sensitive detection of 100 GHz radiation by high mobility field-effect transistors," *Journal of Applied Physics*, 2008.

[96] V. Kachorovskii and M. Shur, "Field effect transistor as ultrafast detector of modulated terahertz radiation," *Solid-State Electronics*, vol. 52, no. 2, pp. 182–185, feb 2008.

A. Publications related to this thesis

Journal publications

- S. Regensburger, M. Mittendorff, S. Winnerl, H. Lu, A. C. Gossard, and S. Preu, "Broadband THz detection from 0.1 to 22 THz with large area field-effect transistors," *Optics express*, vol. 23, no. 16, pp. 20 732–20 742, 2015.

- S. Regensburger, A. k. Mukherjee, S. Schönhuber, M. A. Kainz, S. Winnerl, J. M. Klopf, H. Lu, A. C. Gossard, K. Unterrainer, and S. Preu, "Broadband Terahertz Detection with Zero-Bias Field-Effect Transistors between 100 GHz and 11.8 THz with a Noise Equivalent Power of 250 pW/$\sqrt{\text{Hz}}$ at 0.6 THz," *IEEE Transactions on Terahertz Science and Technology*, vol. 8, no. 4, pp. 465–471, 2018.

- S. Regensburger, S. Winnerl, J. M. Klopf, H. Lu, A. C. Gossard, and S. Preu, "Picosecond-scale Terahertz pulse characterization with field-effect transistors," *IEEE Transactions on Terahertz Science and Technology*, vol. 9, no. 3, pp. 262–271, 2019.

Conference publications

- S. Regensburger, M. Mittendorff, S. Winnerl, H. Lu, A. C. Gossard, and S. Preu, "Symmetry effects in broadband, room-temperature field effect transistor THz detectors," in *2015 40th International Conference on Infrared, Millimeter, and Terahertz waves (IRMMW-THz)*. IEEE, aug 2015.

- S. Regensburger, H. Lu, A. C. Gossard, and S. Preu, "Comparison of large area and lumped element field-effect transistors for broadband detection of Terahertz," in *2017 42nd International Conference on Infrared, Millimeter, and Terahertz Waves (IRMMW-THz)*. IEEE, aug 2017.

- S. Regensburger, S. Winnerl, J. M. Klopf, H. Lu, A. C. Gossard, and S. Preu, "Investigation of parasitic coupling of THz radiation to a large area field-effect transistor," in *2017 42nd International Conference on Infrared, Millimeter, and Terahertz Waves (IRMMW-THz)*. IEEE, aug 2017.

- S. Regensburger, A. K. Mukherjee, S. Preu, H. Lu, and A. C. Gossard, "Broadband Terahertz Detection with an Antenna Coupled Zero-Bias Field-Effect Transistor," in *2018 43rd International Conference on Infrared, Millimeter, and Terahertz Waves (IRMMW-THz)*. IEEE, sep 2018.

Invited oral contribution

- S. Regensburger and S. Preu, "Field-effect transistor-based detectors: covering the THz band and beyond with few ps resolution," in *2019 FELBE/TELBE*

User Workshop Helmholtz-Zentrum Dresden-Rossendorf, Dresden, may 2019.

Conference and workshop contributions

- S. Regensburger, M. Mittendorff, S. Winnerl, H. Lu, A. C. Gossard, and S. Preu, "Ultra Broadband and Fast FET Detectors for THz and NIR at Room-Temperature," in *German THz Conference 2015*, jun 2015.
- S. Regensburger, M. Mittendorff, S. Winnerl, H. Lu, A. C. Gossard, and S. Preu, "Broadband and Fast Large-Area Field-Effect Detectors for THz and NIR," in *VDI workshop Kaiserslautern*, 2016.
- S. Regensburger, S. Winnerl, J. M. Klopf, H. Lu, P. G. Burke, A. C. Gossard, and S. Preu, "Comparison and responsivity improvement of horn- and lens-coupled large area field-effect transistors," in *2nd German Terahertz Conference in Dresden*, 2017.
- S. Regensburger, S. Winnerl, J. M. Klopf, L. Hong, A. C. Gossard, and S. Preu, "20 ps temporal resolution of THz pulses recorded with (Al)GaAs high electron mobility transistors," in *RJUSE 2018 - 7th Russia-Japan-USA-Europe Symposium on Fundamental & Applied Problems of Terahertz Devices & Technologies & 4th TERAMIR International Laboratory Workshop*, sep 2018.
- S. Regensburger, S. Winnerl, J. M. Klopf, H. Lu, A. C. Gossard, and S. Preu, "Amplitude suppression of picosecond Terahertz pulses in a FET detector," in *Optical Terahertz Science and Technology (OTST 2019)*, mar 2019.

Supervised master theses

- Amlan kusum Mukherjee, "Antenna-Coupled Field Effect Transistors for Rectification of Terahertz Radiation," master's thesis, TU Darmstadt, 2017.
- Khawaja Arslan Anwar, "Terahertz Properties of $SrMoO_3$," master's thesis, TU Darmstadt, 2018.

B. Declarations according to general doctoral regulations – Erklärungen laut Promotionsordnung

§ 8 Abs. 1 lit. c PromO

Ich versichere hiermit, dass die elektronische Version meiner Dissertation mit der schriftlichen Version übereinstimmt.

§ 8 Abs. 1 lit. d PromO

Ich versichere hiermit, dass zu einem vorherigen Zeitpunkt noch keine Promotion versucht wurde. In diesem Fall sind nähere Angaben über Zeitpunkt, Hochschule, Dissertationsthema und Ergebnis dieses Versuchs mitzuteilen.

§ 9 Abs. 1 PromO

Ich versichere hiermit, dass die vorliegende Dissertation selbstständig und nur unter Verwendung der angegebenen Quellen verfasst wurde.

§ 9 Abs. 2 PromO

Die Arbeit hat bisher noch nicht zu Prüfungszwecken gedient.

_____

Datum und Unterschrift

C. Acknowledgments

First of all, I am grateful to Prof. Dr. Sascha Preu for his guidance, as well as for many fruitful discussions on physical or technical details. The open-minded working atmosphere he created, being focused rather on physics than formalities is very motivating. Thank you!

Further, I would like to thank the following persons, that contributed to this thesis:

- Amlan k. Mukherjee, for his successful master's thesis on lumped element transistors and fabricating and characterizing device AN-A. His motivation made it fun working together.

- The other doctoral students in Sascha Preu's THz group for the very friendly and also motivationg atmosphere in the last years. A good cup of coffee in the Hipster place, a beer after work, or a barbecue in Uttam's garden were always a nice distraction from work from time to time. Further, i thank Peter Kießlich and Andreas Semrad and the mechanical workshop for dedicated support with mechanical problems in the lab as well as for the CNC drilling of the packages.

- Prof. Dr. Hong Lu (now at Nanjing University) and Prof. Dr. Arthur C. Gossard at University of California, Santa Barbara for the MBE wafer growth with very shallow channels.

- Dr. J. Michael Klopf and Dr. Stephan Winnerl from Helmholtz-Zentrum Dresden-Rossendorf for their support during the beam time at the FEL shifts and discussions on technical details after the FEL shifts. I am further grateful to P. Michel and the FELBE team for their dedicated support.

- Prof. Dr. Heiko B. Weber for allowing me to fabricate FETs in the clean room in Erlangen, where i did my master's thesis before the beginning of my PhD thesis, when the processing was not fully working at TU Darmstadt.

- Dr. Philipp Faltermeier, Dr. Sergey Danilov, and Prof. Dr. Sergey D. Ganichev for allowing me to measure with the CO_2 laser at Terahertz Zentrum Regensburg and their dedicated support during the measurements.

- Dovile Čibiraitė, Prof. Dr. Alvydas Lisauskas and Prof. Dr. Hartmut G. Roskos from Johann Wolfgang Goethe-Universität, Frankfurt(Main), Germany for help with the calibration of the Golay cell. I further want to thank Prof. Dr. Hartmut G. Roskos for taking the time to review this thesis.

- Sebastian Schönhuber, Martin A. Kainz, and Prof. Dr. Karl Unterrainer from TU Wien for the successful collaboration on the measurement of antenna-coupled FETs with a QCL.

- My parents and my brothers, that always supported me, especially Alois for proofreading.

Finally I would like to acknowledge the funding by Deutsche Forschungsgemeinschaft, within Project PR1413/2-1 (LA-FET) and the CST AG for providing the CST Studio Suite for the antenna simulations.

Darmstadt, October 2019 Stefan Regensburger